COMPARISON OF TWO NUCLEUS SPECTRUM MEASURING DEVICES AND THE INFLUENCE OF SEVERAL VARIABLES ON CAVITATION THRESHOLD IN WATER

by

Emin Yilmaz

A dissertation submitted in partial fulfillment
of the requirements for the degree of
Doctor of Philosophy
(Nuclear Engineering)
in The University of Michigan
1974

Doctoral Committee:

Professor Frederick G. Hammitt, Co-Chairman
Professor William Kerr, Co-Chairman
Professor John M. Carpenter
Associate Professor James J. Duderstadt

ABSTRACT

COMPARISON OF TWO NUCLEUS SPECTRUM MEASURING DEVICES AND THE INFLUENCE OF SEVERAL VARIABLES ON CAVITATION THRESHOLD IN WATER

by

Emin Yilmaz

Co-Chairmen: Frederick G. Hammitt, William Kerr

Two nucleus spectrum measuring systems were evaluated by measuring natural nuclei content of tap water. The Coulter counter technique which is used extensively in blood cell counting, and relies upon the electrical conductivity of the liquid, and a light scattering technique were both found to be adequate for nucleus spectrum measurement for special cases. The light scattering method is especially advantageous when the water samples contain particles. Shape and color of the particles were found to be not significant for most of the cases. The Coulter counter can only be adopted to water samples which contain either non-conducting particles and bubbles, or bubbles alone, since the electrical conductivity of bubbles is very small compared to water. For untreated tap water of Ann Arbor, Michigan, an addition of at least ~ 0.1% of salt in the sample is required to obtain a nucleus spectrum close to the nucleus spectrum obtained using the light scattering method. Total nuclei count in this case was about 60% of the nuclei count obtained by the light scattering method.

Inception pressures for cavitation were measured using a sonic horn assembly operating at about 14 KHz. Tap, filtered tap, and degassed tap water samples were used to measure cavitation inception pressures as a function of temperature, gas content, waiting time, addition of different kinds of particles, polymer and wetting agent, magnetic field and fast neutron irradiation. Decrease of cavitation inception pressures were measured when temperature, gas content, and nuclei content were increased. Fast neutron irradiation also decreased the cavitation inception threshold. An increase on cavitation inception pressure was measured when waiting time, addition of polymer or wetting agent were increased. No change in either nucleus spectrum or cavitation inception pressure were found under 5.9 K Gauss magnetic field.

The conical crevice theory was found to be predicting behavior of the inception pressures close enough for most of the variables mentioned. One of the measured cavitation inception pressures was used as reference to evaluate unknown variables and then calculate the nucleation pressure as a function of the variable.

The conical crevice diameters at the interface are calculated using the bubble dynamics equation, and measured cavitation inception pressures, and are found to be 1/10 to 1/40 of that to be expected from the nuclei diameters existing in the water samples.

ACKNOWLEDGEMENTS

The author is greatly indebted to the assistance and moral support provided by his supervisors, Professor F. G. Hammitt and Professor W. Kerr, throughout the course of this research, and wishes especially to acknowledge their endurance through many hours in discussing the problems during the research work and over the manuscript.

The author fully appreciates also the help provided by Dr. Andreas Keller in setting up the Light Scattering System and many long discussions and suggestions on the research work and technical difficulties encountered during the course of the investigation.

The author should also like to express his gratitude to the late Professor Louis J. Hamilton for his advice on dealing with the technical problems, and how to solve them, during his first Ph. D. project.

The financial aid provided by (1) Mechanical Engineering Department of the Middle East Technical University through Agency for International Development, (2) Rackham School of Graduate Studies and (3) Mechanical and Nuclear Engineering Departments of The University of Michigan and (4) National Science Foundation is gratefully acknowledged.

Last, but not least, the author wishes to acknowledge the advice and help provided by his committee members and the services provided by Mechanical Engineering Machine Shop, Computing Center and Nuclear Engineering Department in various aspects of the work.

TABLE OF CONTENTS

LIST OF TABLES

LIST OF ILLUSTRATIONS

LIST OF APPENDICES

NOMENCLATURE

Symbol	Description
A	Area of orifice
a	Area of nucleus
a_c	Critical crevice radius
a_n	Mie coefficient
a_o	Radius of crevice smaller than critical crevice
B	issipation
b_n	Mie coefficient
C	Concentration of gas
c	Sound speed
D	Diffusion coefficient
d	Orifice diameter
E_m	Nucleation energy
e	2.71
f_o	Resonance frequency
g	Acceleration of gravity
h_{fg}	Latent heat of vaporization
I	Intensity
K	Stiffness
Ke	Attenuation factor
k	Thermal conductivity of liquid
L	Energy deposition length
ℓ	Distance
m	Ratio of indices of refraction

Symbol	Description
$n(R_o)$	Distribution density of bubbles/cc
P	Pressure
P_A	Pressure generated by acoustic waves
P_g	Partial gas pressure
P_H	Hydrostatic pressure
P_i	Pressure inside the bubble
P_L	Liquid pressure
P_v	Partial vapor pressure
R	Radius
R_c	Coulter tube orifice resistance
$\dot{R}$	dr/dt
$\ddot{R}$	d^2R/dt^2
ΔR	Resistance change
r	Radial distance
S_n	Riccati Bessel function
T	Temperature
T_∞	Temperature of liquid
T_{sat}	Saturation temperature
t	Time
U	Energy deposition rate
$U(R_o)$	Distribution density of volume for nucleus radius R_o
V	Volume, voltage, velocity
V_c	Control volume

Symbol	Description
ω	Frequency of acoustic field
ω_o	Resonant frequency

Greek Characters

α	Attenuation, liquid thermal diffusivity
α_A	Advancing contact angle
α_R	Receding contact angle
β	Apex angle of a conical crevice
δ	Damping coefficient
η	Kinematic viscosity
η_o	Compressibility constant
γ	Ratio of specific heats
ϕ	Angle of polarization
λ	Wave length of light
μ	Viscosity of water
ν	Ascent velocity of bubble
ρ	Density of liquid
ρ_o	Resistivity of electrolyte
ρ_p	Resistivity of nucleus
ρ_v	Density of vapor
σ	Surface tension
θ	Scattering angle

CHAPTER I

INTRODUCTION

Historical Review

One of the first references to the fact that rotating hydraulic machinery might promote localized low pressure regions, in water which would result in voids or cavities was made by Leonard Euler in 1754 [1]. In 1895 Sir John Thornycraft and S. W. Barnaby [2, 3], in England, presented a paper on the screw trials of a new torpedo boat destroyer, Daring, in which they postulated that the reason for her poor performance was the inefficiency and loss of power caused by the formation of cavities in the water. R. E. Froude initiated the use of the word "cavitation" to describe this phenomenon. The same speed could be obtained as with the original screws by increasing surface area of the blade and reducing horsepower. In 1894, Sir Charles Parsons [4] formed a syndicate to test applications of steam turbines to marine propulsion, and the ship Turbina was started.

In a recent review of Parson's work, L. C. Burrill [5] indicates that even before Turbina was built, or cavitation recognized, Parsons anticipated that the high speed of the turbine drive would require several fine pitched screws on a shaft in order to obtain a sufficient blade area to provide the required thrust. The initial trials of the Turbina were unsuccessful in that power consumption was excessive for the low speed attained.

After considerable experimentation with various configurations, Parsons decided on three separate shafts each with three screws, and driven by three turbines. In conjuncation with these experiments, Parsons ran a two inch diameter model screw in water within a few degrees of boiling, and photographically observed the formation of cavities behind the leading edge of the screw near the blade tip. At higher speeds a complete vapor cavity was formed with almost all the power going into maintaining the cavity.

As pumps and propulsion units became more powerful, another phenomenon became apparent. Even if the performance is not noticeably affected, bubbles may form on the low pressure side of the blade and collapse as they move into higher pressure regions on the blade. High pressure created by collapse of bubbles caused pitting of the blades. Sir Charles Parsons and S. S. Cook [6] after extensive investigations, came to the conclusion that the damage was mechanical in nature and was caused by collapsing cavities.

Relatively clean liquids are found to be able to support considerable tension or can be superheated above the stable boiling point without boiling. Reynolds [7] has described experiments with a column of mercury in 1877 in which the column of mercury had a tension at the top of nearly two atmospheres without breaking the column. Fisher [8] has calculated the fracture strength of pure liquids and found that calculated values were greater than the maximum experimental values by a very large amount. In real liquids, however, nucleation of bubbles may occur from solid particle or gas microbubble contaminants.

A good review of literature on theoretical bubble analysis is given by Ivany [9].

Motivation

An important aspect of the study of cavitation phenomena is the determination of the conditions which lead to incipient cavitation. The interest in producing controlled cavitation for the purpose of studying the hydrodynamic phenomena was paralleled by interest in producing controlled conditions for the study of cavitation erosion. This led to laboratory devices for accelerated damage testing. All these devices involved a controlled time of exposure of materials to a cavitation attack of a fixed average intensity [10].

Vapor cavity formation in liquid can occur under a wide variety of situations. These situations can be classified into three main groups: superheating a liquid, supersaturating a liquid with a gas, or cavitating a liquid. Cavitation can also be considered as a case of superheating the liquid by decreasing the static pressure above it. However, a liquid will not start boiling near saturation temperatures unless there is at least one "nucleus" existing in it. Probability of formation of bubbles of about molecular dimensions ($\sim 10^{-8}$ cm) in a pure liquid is very high [11]. However probability of formation of bubbles of radius of about 10^{-7} cm is almost zero. Thus for a bubble of radius of about 10^{-8} cm, the tensile strength required to make it grow at room temperature is:

$$P_i = \frac{2\sigma}{R} + P_H$$

$$P_i \cong 1.5 \times 10^4 \text{ bars} \qquad (1\text{-}1)$$

where equation (1) expresses the mechanical equilibrium of a bubble of radius R, and σ is the surface tension. Figure 1-1 gives the probability of formation of a vapor bubble of radius R.

The maximum negative pressure observed in water is about 270 atm at $-8^{\circ}C$ [12]. That the magnitude of observed negative pressure in liquids is low compared to calculated values is usually attributed to the impurities in the liquids.

No method has been found to be completely effective in removing such impurities from liquids. Thus it is very important to know what kind of impurities exist in water to contribute to an understanding of cavitation inception.

The effects of neutron or other high-energy particle irradiation in liquids are of vital interest to nuclear reactor core designers as well as to those concerned with bubble chambers, or with the basic understanding of nucleation process.

Objective

Two nuclei spectrum measurement systems will be compared, and one will be selected for the nucleus spectrum measurements to study cavitation inception at 14 KHz imposed pressure oscillation using an acoustic horn assembly. One of the nucleus size measurement methods is the Coulter counter method which relies on the instantaneous interruption of the path of electrical conductivity between

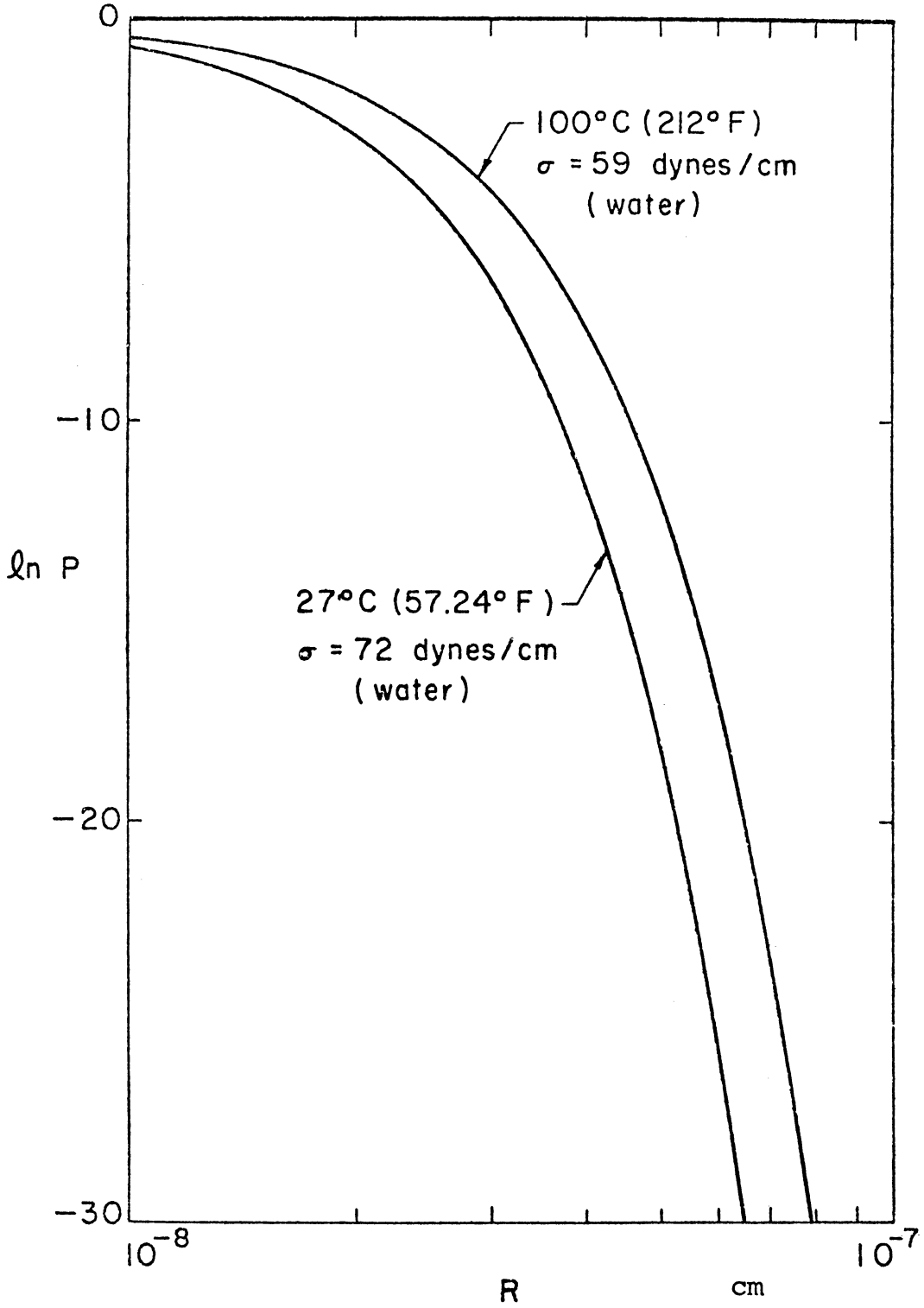

Figure 1-1 Probability of Formation of a Vapor Bubble of Radius R.

two electrodes. It has been developed in this laboratory for measuring cavitation "nuclei" (or microbubbles to use current terminology), in both a tunnel and in a static ultrasonic facility [13, 14]. The other is the scattered light method. In this method, the amount of scattered light from a nucleus is measured. A laser provides a most convenient source of light for this purpose. This method has been recently adapted to the measurements of cavitation nuclei by A. Keller [17].

The effect of

(i) gas content

(ii) nucleus spectrum

(iii) temperature

(iv) filtration

(v) addition of particles

(vi) neutron irradiation

on sonic cavitation inception in water was then investigated by the author. at atmospheric pressure.

Magnetic field effects on cavitation damage in sodium have been reported by Perel'man and Govorskii [15] and magnetic and electric field effects on cavitation damage patterns even in water tunnels have been reported [100]. Here, an attempt will be made to measure effects of magnetic fields, if any, on nucleus spectrum and cavitation inception pressure of tap and slightly conducting tap water. About 20 times larger (5.9 K Gauss) magnetic field than that used, by Perel'man will be used for investigations. Shalobasov and Shal'nev [100] used 3-7 K Gauss magnetic field in their water tunnel experiments.

CHAPTER II

THEORY

Nucleus Spectrum Measurements

Scattered Light Method

Since the nucleus spectrum measurement by scattered light depends on the light scattered by individual nuclei, an attempt will be made to explain, in detail, the nature of light scattering by bubbles.

Much of the literature on scattering is concerned with the scattering by particles or discontinuities in a medium which is small with respect to the wavelength of light. Some of them are listed below [16]:

i. Compton and Raman Scattering - apply to particles of molecular size, whenever the scattered radiation experiences quantum transitions, i. e. frequency changes, at the instant of scattering.

ii. Brillouin Scattering - results from density fluctuations in a fluid as a result of thermal excitation.

iii. Raleigh Scattering - applies to scattering by particles of arbitrary shape which are small compared with the wavelength of light.

iv. Mie Scattering - is applicable to spheres of any size and refractive index.

The first three items do not apply to this case; the last one (i. e. the Mie Solution) covers the range of bubble size to be measured by our instrument which uses a He-Ne laser. The Mie Theory [17] describes the scattering properties of a homogeneous isotropic sphere in

a plane monochromatic wave field. The resulting equations are infinite series which give the scattering intensity, I, as a function of the scattered angle, θ, the angle of polarization, ϕ, the sphere radius, R, the wave length of light, λ, and ratio, m, of the indices of refraction ($\eta_{sphere}/\eta_{water}$).

The dimensionless number $\alpha = 2R\pi/\lambda$ is used to represent the influence of the radius R. At distance $l \gg R$ from the nucleus, the intensity, I, of the light which is scattered at an angle θ, versus the incoming rays consist of two parts:

$$I = I_1 + I_2 \tag{2-1}$$

where I_1 is the intensity of that portion of the light which is polarized perpendicular to the observation plane

$$I_1 = I_o \cos^2\phi \frac{\lambda^2}{4\pi^2 l^2} \left| \sum_{n=1}^{\infty} \frac{2n+1}{n(n+1)} (a_n A_n + b_n B_n) \right|^2 \tag{2-2}$$

I_2 is the intensity of the light polarized parallel to it

$$I_2 = I_o \sin^2\phi \frac{\lambda^2}{4\pi^2 l^2} \left| \sum_{n=1}^{\infty} \frac{2n+1}{n(n+1)} (a_n B_n + b_n A_n) \right|^2 \tag{2-3}$$

The observation plane is defined by the laser ray and the observation point. I_o is the intensity of the incoming polarized monochromatic light.

One can obtain approximate values of I_1 and I_2 by truncating the series after a sufficiently high number of terms. The coefficients A_n and B_n are only dependent on the scattering angle θ and can be calculated from the derivatives of the Legendre polynomials $P_n(\cos\theta)$

$$A_n = \frac{\partial P_n(\cos\theta)}{\partial(\cos\theta)}$$

$$A_n' = \frac{\partial A_n(\cos\theta)}{\partial(\cos\theta)}$$

$$A_o = \frac{\partial P_o(\cos\theta)}{\partial(\cos\theta)} = 0; \qquad A_o' = 0$$

$$A_1 = 1, \qquad A_1' = 0$$

The remaining values of A_n and B_n can be obtained with the recursive equations:

$$A_n = \cos\theta \left(\frac{2n-1}{n-1}\right) A_{n-1} - \frac{n}{n-1} A_{n-2},$$

$$A_n' = (2n-1)A_{n-1} + A_{n-2}',$$

$$B_n = \cos\theta\, A_n - (1 - \cos\theta)A_n'$$

The Mie coefficients a_n and b_n depend upon the breaking index ratio, m, and Riccati Bessel functions

$$a_n = \frac{S_n'(\beta)S_n(\alpha) - mS_n'(\alpha)S_n(\beta)}{S_n'(\beta)\Phi_n(\alpha) - m\Phi_n'(\alpha)S_n(\beta)},$$

$$b_n = \frac{mS_n'(\beta)S_n(\alpha) - S_n'(\alpha)S_n(\beta)}{mS_n'(\beta)\Phi_n(\alpha) - \Phi_n'(\alpha)S_n(\beta)},$$

$$S_n(x) = \sqrt{\frac{\pi x}{2}}\, J_{n+\frac{1}{2}}(x)$$

$$C_n(x) = (-1)^n \sqrt{\frac{\pi x}{2}}\, J_{n-\frac{1}{2}}(x)$$

$$\Phi_n(x) = S_n(x) + i\, C_n(x);$$

$$\beta = m\alpha$$

J is the Bessel function of the first kind.

Mie scattering intensity, I, has been calculated by Keller [17] for the range of the required parameters.

Figure 2-1 shows the calculated intensities for four different bubble diameters.

Figure 2-2 shows the relation between nucleus size and scattered light intensity for a scattering angle of 90 degrees. It is clearly seen that intensity decreases significantly with the nucleus radius. For a bubble radius greater than ten times the wavelength of laser light, an approximation derived from geometrical optics produces acceptable values for the scattered light intensity. The intensity is then proportional to light flux which hits the bubble, and therefore it is proportional to R^2. The dotted line in Figure 2-2 shows the scattered light intensity versus the nucleus radius as obtained from the geometrical approximation. Above R = 8.5 μm one can observe a good agreement with the values obtained from the Mie theory.

Coulter-Counter Method

The operational principle of the Coulter counter is based on the fact that when a relatively non-conducting particle passes through a media containing a continuous and consistent current field (via a conducting electrolyte) variations in the resistance of this field occur which may be electronically detected, and related to the particle size [13, 14, 18, 19, 20]. Figure 2-3 shows how the system operates.

Particles or bubbles present in the electrolyte are aspirated through an orifice in the wall of a non-conducting tube through which

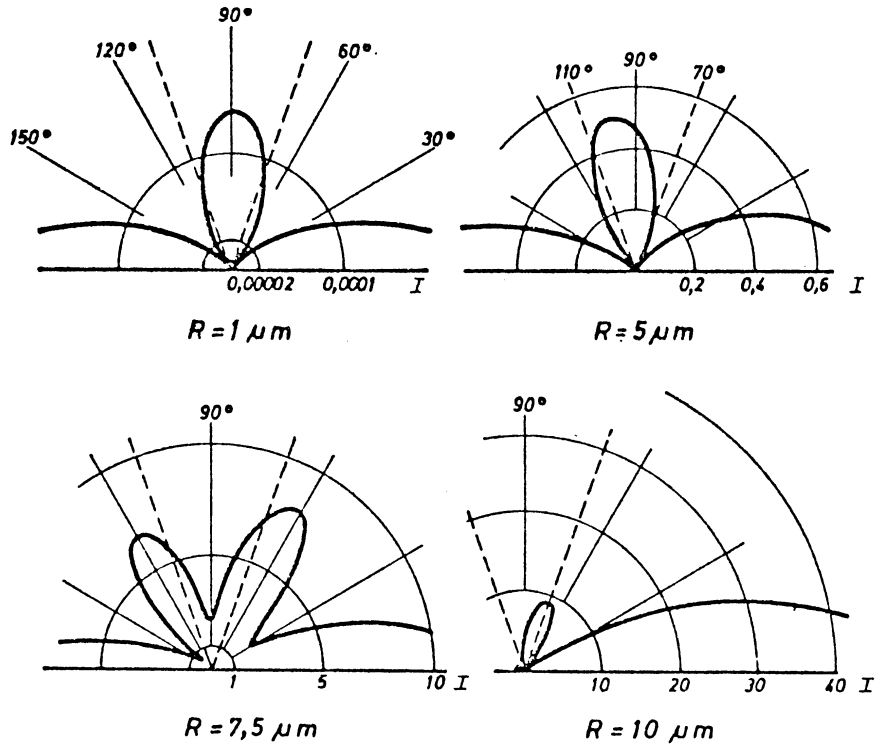

5001

Figure 2-1 Four Polar Diagrams of the Scattered Intensity of Small Air Bubbles in Water.

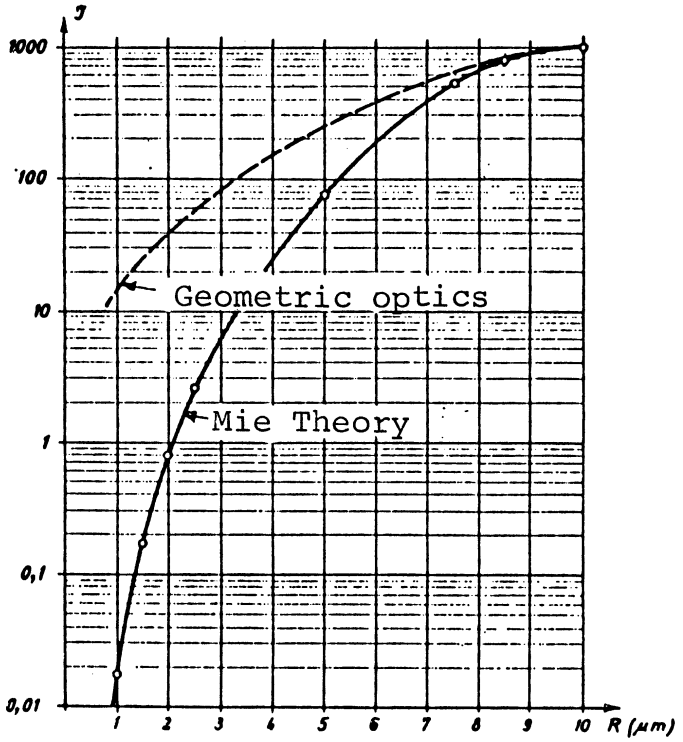

5002

Figure 2-2 Function I=I(R), Found by Integrating the Scatered Light Intensity over the Spherical Angle Which is Covered by the Optical System.

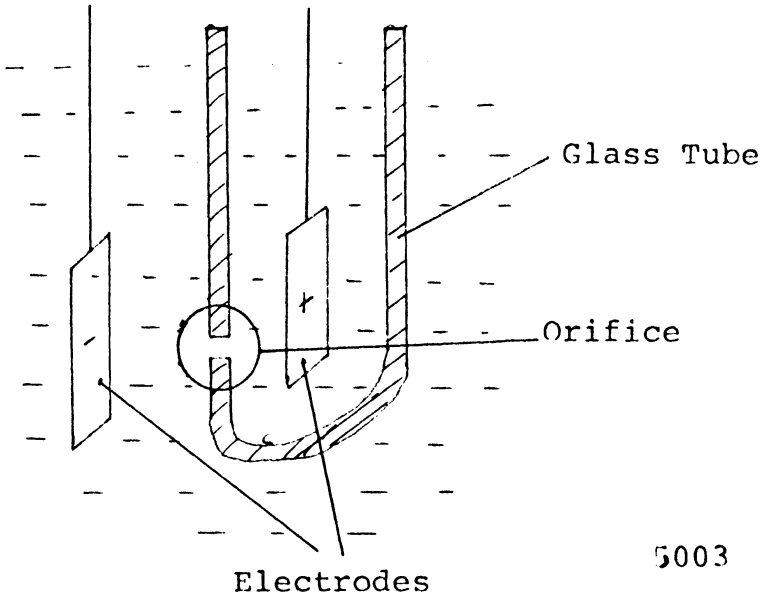

Figure 2-3 An Enlarged Wiev of Orifice on Tube.

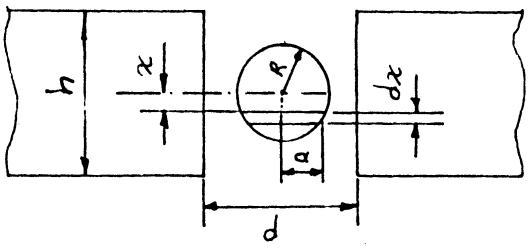

Figure 2-4 A Particle of Radius R in an Orifice of Diameter d.

5004

an electric current also passes. As a relatively non-conducting particle passes through the aperture, it changes the resistance between two electrodes. The resulting voltage variation is amplified and analyzed electronically.

Now, let us derive an equation which relates particle volume to the resistance change through the orifice [14, 20]. As shown in Figure 2-4, the resistance of the small element of orifice without particle, dR_o, is given by

$$dR_o = \frac{\rho_o dx}{A}$$

and resistance of a small element of particle, dR_p, by

$$dR_p = \frac{\rho_p dx}{a}$$

where

$A = \pi d^2/4$

$a = \pi r^2$

ρ_p = resistivity of particle

ρ_o = resistivity of electrolyte

The resistance of a small element with a particle included, dR_{op}, is the two resistances in parallel

$$dR_{op} = \frac{1}{\frac{A-a}{\rho_o dx} + \frac{a}{\rho_p dx}}$$

Thus, the change of resistance of small elements, due to the temporary precesence of a particle or bubble, will be

$$dR = dR_{op} - dR_o$$

$$= (1 - \frac{\rho_o}{\rho_p}) \frac{\rho_o}{A^2} dx \left[\frac{a}{1-(1-\frac{\rho_o}{\rho_p})\frac{a}{A}} \right]$$

Integration of dR from -R to R will give total incremental resistance due to presence of a particle, which is

$$\Delta R = 2\pi(1 - \frac{\rho_o}{\rho_p}) \frac{\rho_o}{A^2} \int_0^R dx \left[\frac{R^2 - x^2}{1-4(1-\frac{\rho_o}{\rho_p})\frac{R^2-x^2}{d^2}} \right].$$

(i) Solution for $\rho_o << \rho_p$

This is the case for bubbles such as gas nuclei in water, but may not be the case for particles.

$$\Delta R \cong \frac{2\rho_o}{A^2} \pi \int_0^R \frac{R^2 - x^2}{1 - \frac{R^2 - x^2}{(d/2)^2}} dx$$

Since $r^2 << d^2$ for practical use of the instrument

$$\Delta R \cong \frac{\rho_o}{A^2} V \qquad (2.4)$$

where V is the volume of the particle.

(ii) Solution for $\rho_o >> \rho_p$

This is the case with particles which are more conducting than the electrolyte.

$$\Delta R \cong -\frac{2}{A} \rho_o R \qquad (2.5)$$

If a cylindrical particle is assumed, calculations are very much

simplified. With the assumption that thickness of orifice is smaller than bubble diameter, one gets [18]

$$\Delta R = \frac{\rho_o}{A^2} \frac{1}{\frac{1}{1 - \frac{\rho_o}{\rho_p}} - \frac{a}{A}} V \qquad (2\text{-}6)$$

where no approximations have been made on resistivities of electrolyte and nuclei.

Quite an error is introduced on the measured particle size if $\rho_o \cong \rho_p$. Error as a function of resistivity ratios are given in Appendix A.

Thus, for nuclei which have resistivities very much larger than electrolyte, water for example, resistance change due to a nuclus will be proportional to the nucleus volume. However, if nuclei are much more conductive than the electrolyte, resistance change will be proportional to radius of the nucleus, and will of course be in the opposite direction.

Sound Attenuation Method [21, 22, 23]

This is an alternative method which has been considered and used elsewhere, and will only briefly be described here. The method is based on the attenuation of sound by the bubbles present in the test section. Bubbles of a certain size resonate under the frequency of an applied sound wave. These will then contribute much to the attenuation of the sonic beam in this frequency. Free gas bubbles contribute most to the attenuation of sound, and suspended particles have a negligible effect. A bubble which exists in water in direct contact with liquid

forms an oscillator of zero order. The displaced liquid forms the mass of the resonant system, and the gas bubble acts as a spring. Thus energy of the propagated sound will be absorbed by the resonating bubbles. In general, the attenuation factor can be written as [23]

$$K_e = 1.5 \times 10^5 \, U(R_o) = 6.3 \times 10^5 \, n(R_o) R_o^3 \qquad (2\text{-}7)$$

where K_e is the attenuation factor in dB/m, $U(R_o)$ and $n(R_o)$ are the distribution densities of the volume and number of bubbles per cubic centimeter of water, and R_o is the resonance bubble radius at a given acoustic frequency.

Appendix B gives the derivation of resonance frequency as a function of bubble radius, assuming a spring-mass system analogy. Resonance frequencies are found to be [21]

$$f_o = \frac{1}{2\pi R_o} \sqrt{\frac{3\gamma}{\rho} \left(P_L + \frac{2\sigma}{R_o} \right)} \qquad (2\text{-}8)$$

and attenuation perturbation is given by

$$\alpha = 8.68\pi \frac{f_o}{c_o} \frac{\eta_{oi}}{\eta_{or}} + 4.03 \times 10^2 \, V f_o \qquad (2\text{-}9)$$

in KMS units,

where c_o is the velocity of sound in water, and V is the total volume concentration of free gas. η_{oi} and η_{or} are imaginary and real parts of the complex compressibility constant η_o.

The first term in equation (2-9) is the attentuation due to pure water, and the second term is the perturbation or attenuation due to bubbles. The first term can be evaluated by measuring the attenuation

when the liquid is under large static pressure. Thus it is expected that all bubbles will dissolve in water.

Figure 2-5 shows a block diagram for a sound attenuation measuring system [21]. The system employs a transducer to transmit a short pulse of ultrasonic energy through the water to a reflector, and back to the transducer over a total length of one meter. The echo strength is compared to the signal through a reference attenuator to obtain a relative attenuation. 100 to 940 KHz frequency range is required to measure bubble radius range of 4-34μm. These high frequencies are unfortunately rapidly attenuated in liquids, and sound scattering and large background noise as carried through the pipe becomes a problem.

Microscopic and Holographic Methods

Both methods, in principle, employ photography of nuclei existing in transparent liquids. In microscopic method a microscope and a camera is used. Photographs of a sample of liquid are taken at different focal planes and the size of nuclei is sorted by visual inspection of the photographs.

The holographic method employs two lasers by which holograms of nuclei are developed passing through the test section. Photographs of holograms are used to measure nuclei size and number.

Both methods are time-consuming compared to the previously mentioned three methods. However, they have the possibility of distinguishing between bubbles and solid particles.

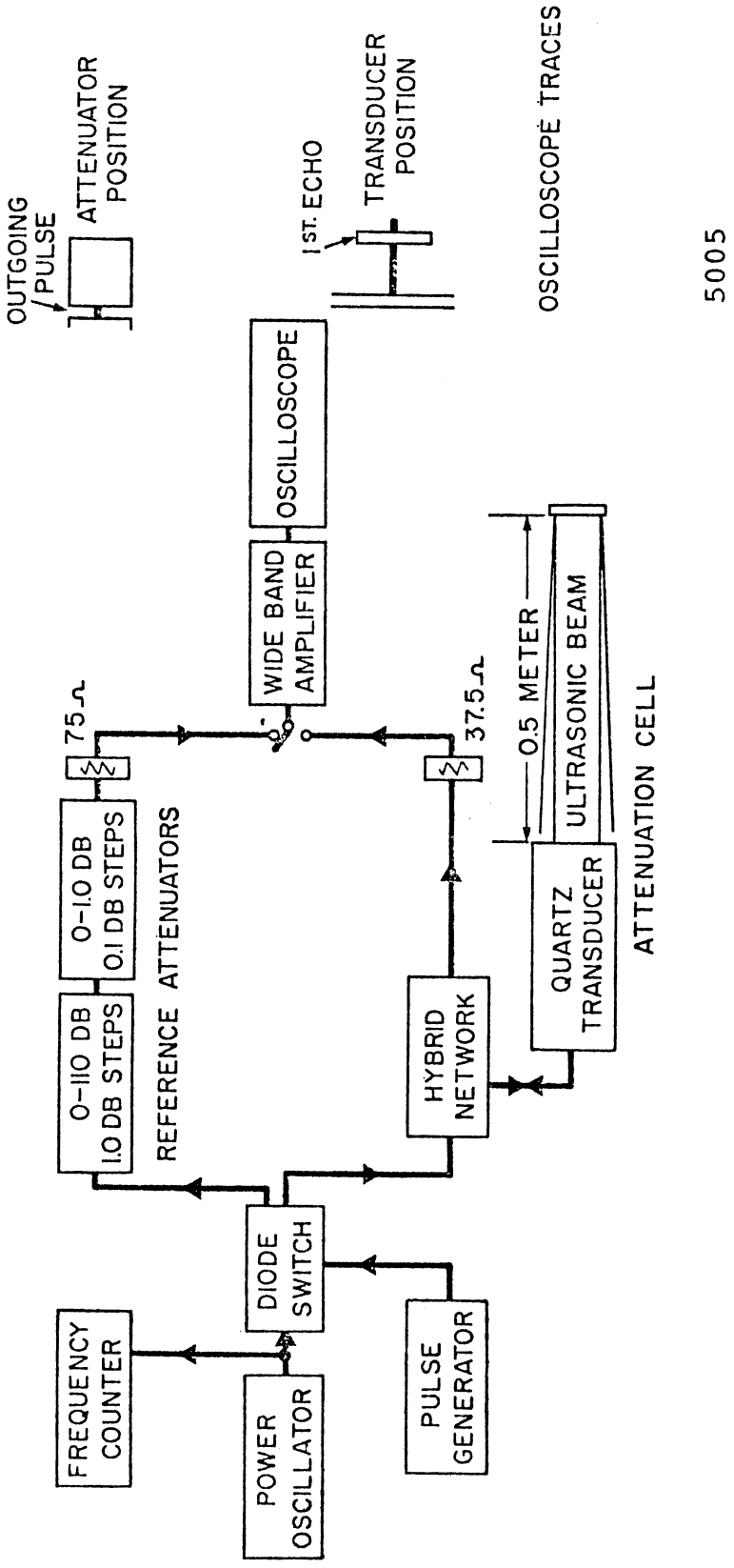

Figure 2-5 Block Diagram of Electronic System.

Acoustic Cavitation

Introduction

Cavitation created by induced sonic pressure oscillations is usually referred to as "acoustic cavitation". An acoustical standing wave system is a good way of obtaining easily controlled pressure variation at any point in a liquid. Mainly two types of acoustic cavitation systems are used. The first is a spherical resonator, which is a spherical flask excited externally by either a magnetostriction or a piezoelectric transducer. Resonance frequencies starting from 15 KHz up to 2.5 MHz have been used successfully [24, 25, 26, 31].

The second method was developed originally for damage tests, and used in this laboratory [27] and elsewhere, for that purpose. Later on, it is adapted to measure cavitation inception pressures in water [14]. Vibrations of piezoelectrically excited resonating horns is transferred to a sample of liquid. Standing sound waves are created in the sample to cause sonic cavitation.

Several factors influence inception of cavitation in a sample of water. The effect of these factors will be investigated separately in the following sections.

Effect of Nucleus Size

The term nucleus, here, will refer to holes, bubbles, solid particles or any combination of these. It has been stated in Chapter I that without any existing nuclei, tensile strength of water would be thousands of atmospheres. Since this is not the case for real liquids (except in extremely careful laboratory experiments), nuclei much larger than

molecular dimensions must exist in liquids. A realistic value of 5 bars tension (P_i = 5 bars), requires that the radius, using the static pressure balance, of existing holes be at least 0.36 μm (i.e., $R = 2\sigma/(P_i - P_H)$). The theoretically predicted natural hole sizes [11] are about 10^{-4} μm. Not all foreign materials added to a liquid will affect the cavitation process. Unless it effects the formation, growth or collapse of the cavities, the impurity will have little effect on cavitation [28]. Since very large amounts of impurities, sufficient to change its gross properties, are not expected to exist in liquids of interest, attention here will be focused upon the impurities that affect the formation of cavities by providing "weak spots". Non-miscible and nonsoluble substances appear to be closely related in that determination of the degree of wettability is of major importance (in liquid tensile strength) between two liquids, or between solid particles and liquid. Measurements of the contact angle between liquids and solids indicate that no liquid wets any solid particle perfectly (i.e., contact angle is zero), and all liquids wet all solids to some extent [10].

Harvey [29] and Knapp [35] showed that if water is subjected to 1000 atmospheres for 15 minutes and then the pressure is removed, no cavitation could be produced for a considerable time. This, they explained, by the effective destruction of "nuclei", the undissolved gas having been forced into solution by the high pressure. Thus, the assumption of "micro-bubbles" and unwettable solids entrapped in the liquid, is compelling. If cavitation nuclei are micro-bubbles, they

must somehow be stabilized in water. However no such stabilizing mechanism has yet been conclusively demonstrated, giving rise to the so-called microbubble persistence paradox.

Harvey [29] postulated that the gas bubbles existed in unwetted crevices in solid particles or the walls, and this is the mechanism most commonly accepted today.

Existence of free bubbles have been postulated for flowing systems where some portion of the loop allows constant gas entrainment. Fox [30], and others, showed that for non-flowing systems small bubbles will dissolve due to the pressure unbalance between entrapped gas and surrounding liquid due to surface tension, and large bubbles will quickly float to the surface. He showed that even when water is saturated with air, dissolution time of a bubble is

$$t = \frac{R^2}{3D\alpha} \left(1 - \frac{P_L}{2\sigma} R\right) \qquad (2\text{-}10)$$

where α is the proportionality constant for Dalton's Law, which relates the concentration of air to pressure inside the bubble (i.e., $C = \alpha P_i$). On the other hand, a bubble will float to the surface due to buoyancy with a speed in cm/sec $\tilde{=} 20000\, R^2$, in cold water, following Stoke's equation, where R is in cm.

Thus a bubble larger than 10 μm will not exist more than a few minutes in a test beaker, and a bubble smaller than 10 μm will dissolve in water in less than 8 seconds. Thus, the "microbubble persistence paradox".

Fox [30], has introduced a stabilizing mechanism, differing from that of Harvey [29], previously discussed. In his hypothesis, free bubbles in water are assumed to acquire an impervious organic skin. This organic skin will prevent any diffusion of gas into the liquid and will also support any surface tension pressures. Thus, small bubbles (order of 1 μm) will exist in water for long periods, without being forced into solution. However, this hypothesis is now partially abandoned [97], on the grounds that various experiments do not support it. However, it seems quite probable that combinations of various mechanisms are responsible for the stabilization observed in many cases.

Sirotyuk [97] demonstrated experimentally that the stabilization of gas bubbles acting as cavitation nuclei in water can be attributed to the presence of surface-active substances in the water. This does not exclude the hypothesis that bubbles can be stabilized in the crevices of impurities. In his studies, the contents of surface active substances in ordinary distilled water amounted to about 10^{-7} mole/lt. The reduction in the content of these substances to about 2×10^{-8} mole/lt yielded an increase in the strength of the water to about 7.5 atm. However, it is of course possible that other impurity contents were also changed. He used a 15 KHz magnetorestrictive radiator to create cavitation at the focal zone, so that his experiments are quite closely related to our own.

The hypothesis, which leads to stabilization of nuclei by the existence of ions in water has also been proven not to be the case. Sirotyuk's [97] experimental results show no dependence of cavitation inception on conductivity of water.

Harvey [31], as already mentioned, suggested dust particles as stabilizing agents for bubbles. His theory indicated that microbubbles can exist almost indefinitely if trapped in submicroscopic hydrophobic cracks in such solid particles. His mechanism appears to be somewhat complicated but is the mechanism most generally accepted today. It offers the advantage of providing a physically conceivable way of distributing nuclei throughout all liquid. The trapping of air in a crack requires that the crack wall be "hydrophobic", i. e. not wetted by water. If, on the contrary, the wall were wetted, water would creep into the crack and displace the air [32]. The theory of unwetted particles is supported by the fact that many organic liquids are considerably more resitant to cavitation than water, although they have up to ten times higher gas solubilities, and a smaller theoretical tensile strength [18]. The higher resistance to cavitation of these liquids is believed due to their better wetting capability, so that no gas bubbles cling to suspended particles, etc. or dissolve, if they do penetrate crevices of particles. However, if crevices are hydrophobic, surface tension will act to decrease the equilibrium pressure inside the bubble, so that the contained gas will not be forced into solution. Also bubbles can more easily start growing from such non-wetted crevices if the

external pressure is reduced. However, such a nucleus can be forced to dissolve, or at least to decrease greatly in size, if the surrounding liquid were subjected to a pressure high enough to dissolve the gas in spite of the surface tension effect. If these crevices were formed of pure acute angle rays, an infinite pressure would be required to completely dissolve the gas. If the bottom of the crevice were slightly rounded, the gas would dissolve with lower liquid pressure.

Plesset [11] has studied solid nuclei in the absence of gas. He considered solid nuclei which are wetted by the liquid, i.e. hydrophilic solids and solids which are not wetted. He showed that for the wetted solid particles, liquid rupture would occur first at locations other than such a nucleus, since a wetted solid has a greater adhesion for the liquid than the cohesion of the liquid for itself. On the other hand, the hydrophobic solid causes a weak point in the liquid, and the tension required for liquid rupture is considerably less than that of pure liquid. The tension required to create a vapor bubble of size R_o is $\frac{2\sigma}{R_o}$. Holl [33] has given a good review on "Cavitation and Nuclei". Many substances in fact found in water are partially hydrophobic like sulfide ores, heavy metals, some metal oxides, graphite, charcoal, greases, etc.

Apfel [34] has extended the theoretical work of Harvey, et al. [29, 31] and Strasberg [32] in order to consider the conditions that must exist in a liquid for a vapor cavity to be nucleated from an imperfectly wetted solid impurity in the liquid. He found that for sufficiently small and readily wetted motes, the tensile stress required for nucleation is

almost independent of gas content. However for large and imperfectly wetted motes, the gas content of the liquid is found to be crucial.

Effect of Temperature

A vapor bubble will not grow unless the temperature of the liquid is at least slightly greater than saturation. Saturation can be obtained by two methods. The conventional way is to increase temperature of the liquid. The other is to decrease the pressure of the liquid. Figure 2-6 gives the relationship between pressure and temperature for saturated water. Any state below the saturation line is called a superheated state for the liquid. Superheat is defined as the temperature difference between vapor temperature and saturation temperature.

Under even slight superheated conditions liquid evaporates into the bubble, if sufficiently large nuclei exist. As liquid evaporates into the bubble, the surface of the bubble, from which evaporation takes place, must move to satisfy mass continuity requirements. This problem was first treated by Plesset and Zwick [36] to a first approximation for a spherical boundary.

Forster and Zuber [37] solved the extended Rayleigh equation [38]

$$\rho[R\frac{d^2R}{dt^2} + \frac{3}{2}\dot{R}^2] = \Delta P - \frac{2\sigma}{R} \qquad (2\text{-}11)$$

assuming that the system is under constant pressure. The pressure ΔP in this equation can be determined from the Clausius-Clapeyron equation for thermodynamic equilibrium, which connects the pressure difference to the temperature difference ΔT, i.e. to the difference in

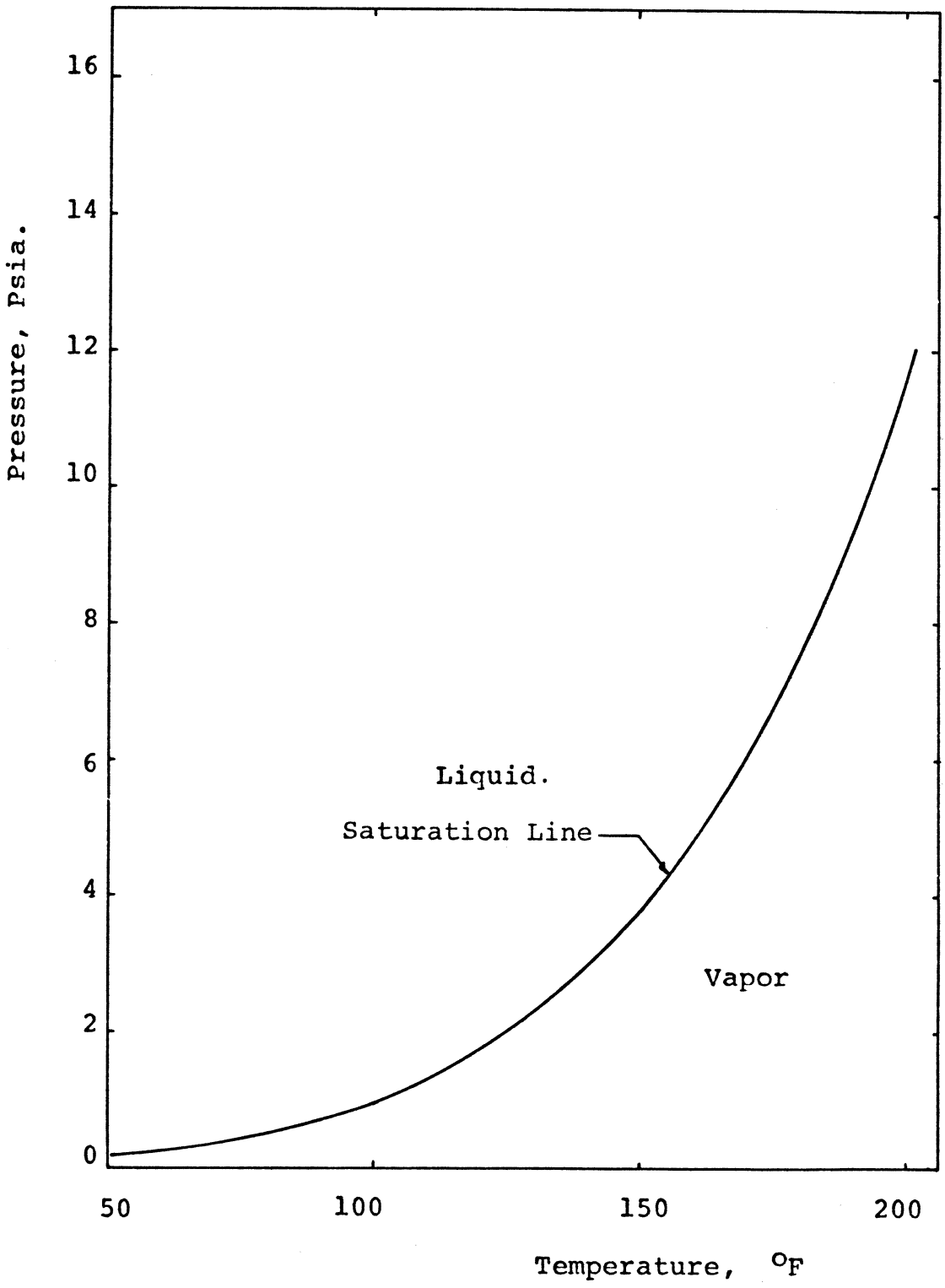

Figure 2-6 Saturation Curve for Water.

5006

saturation temperatures inside and at great distance from the bubble. Then,

$$\Delta P \cong \frac{\rho_v}{T} h_{fg} \Delta T \tag{2-12}$$

where h_{fg} is the latent heat of evaporation, ρ_v is the density of vapor, and temperature difference, ΔT, is determined by the solution of the heat conduction problem with a moving surface of evaporation. Approximate solutions are also given by other authors, which approximate the data obtained in experiments [39, 40, 41, 43, 44, 45, 47].

Forster [42] solved the problem of diffusion of heat in a moving medium with given motion of the boundaries. His numerical method neglects the contribution of convection on heat diffusion. The general heat diffusion equation is:

$$\alpha \nabla^2 T - V(r,t) \cdot \text{grad } T - \frac{\partial T}{\partial t} = 0 \tag{2-13}$$

where α is the liquid thermal diffusivity. For spherical bubbles, the growth equation (2-13) can be written as

$$\frac{\partial T}{\partial t} + V(r,t) \frac{\partial T}{\partial r} = k\left(\frac{\partial^2 T}{\partial r^2} + \frac{2}{r} \frac{\partial T}{\partial r}\right) \tag{2-14}$$

where k is the thermal conductivity of liquid and $V(r,t)$ is the radial velocity of liquid at position r from center of bubble. Initial and boundary conditions for the differential equations are

$$T(r,0) = T_\infty$$

$$T(R,t) = T_{sat}$$

and

$$k \left(\frac{\partial T}{\partial r}\right)_{r=R} = (\rho_v \, h_{fg} \, R)_{r=R}$$

where the last boundary condition gives how much vapor mass is evaporated into the bubble.

Plesset and Hsieh [46] solved the heat diffusion equation under oscillating pressure fields. Their only approximation is the linearization of the Raleigh and heat diffusion equations and related initial and boundary conditions. If the assumption is made that conditions within the bubble are uniform, the thermodynamic relations found are as expected; i. e. at low frequencies the bubble behaves isothermally and at high frequencies the behavior becomes adiabatic. In their calculation, however, no phase change is considered.

Hickling [98] explained the strong dependence of the luminous intensity on the nature of the gas dissolved in the liquid in terms of thermal conduction and demonstrated anlytically by means of a numerical solution of the equations of motion of a gas inside a collapsing cavitation bubble. He found that if the cavitation bubbles are sufficiently small, loss of heat from the bubble into the liquid can significantly reduce the temperature attained during collapse. In his analysis only effect of noncondensable gases are included.

Effect of vapor and other thermodynamic parameters upon spherically symmetric bubble collapse are examined numerically by Mitchell and Hammitt [99]. The net effect of vapor present in the bubbles is found to reduce collapse temperatures and pressures. It is also shown that the value of evaporation coefficient has very strong influence

on collapse pressures and velocities.

Effect of Dissolved Air

The effect of dissolved air was noticed in early experiments by Blake [48]. A sample of tap water, left open to atmosphere for one or two days and hence approximately saturated with air at atmospheric pressure and sample temperature, was cavitated acoustically. Bubbles were produced at very low acoustic power levels in such air saturated water.

Bubbles formed under supersaturated conditions did not collapse but floated to the surface. For tap water, aged several days until its gas content is in equilibrium with atmospheric pressure, the phenomena are quite different. As the power input to the liquid was increased, more and more small bubbles resembling fog were formed. After the power was turned off, a small clear bubble was left. This remained relatively stationary, or rose slowly in the liquid. The phenomena observed for such vaporous, and foggy, cavitation were so dissimilar that Blake [48] felt that an entirely different process led to the formation of gas filled (as opposed to vapor-filled) bubbles. Thus the process of formation of gaseous bubbles in acoustic cavitation can be attributed partly to the diffusion of gas into bubbles. When the negative cycle of the acoustic field acts on the liquid, the liquid, becomes supersaturated, following Henry's Law [49]. Ordinarily one cannot expect a dissolved gas to participate effectively in the development of a cavity since the rate of diffusion of dissolved gas in a liquid is quite

small. In water, for example, the diffusivity coefficient for dissolved air, D, has the value of about 2×10^{-5} $cm^2/sec.$ at 20^oC. Nevertheless, the possibility for the formation of a gas bubble under high-frequency pressure oscillations is high, due to "rectified diffusion."

Rectified Diffusion

Gas diffuses into the bubble during the expansion half-cycle in which the pressure drops below its mean value, and diffuses out of the bubble during the compression half-cycle in which the pressure rises above its mean value. Since surface area of the bubble under the expansion cycle is larger than during the compression cycle, there will be a net air inflow into the bubble.

Several authors investigated the diffusion of mass under oscillating pressure fields [48, 50-57]. Analysis of the problem required the solution of diffusion equation in spherical coordinates:

$$\frac{\partial C}{\partial t} + V(r,t)\,\nabla C = D\nabla^2 C \qquad (2\text{-}15)$$

where $V(r,t)$ is the velocity of the liquid and C is the concentration of air in the liquid.

In spherical coordinates the equation (2-15) can be written as

$$\frac{\partial C}{\partial t} + V\frac{\partial C}{\partial r} = D\left(\frac{\partial^2 C}{\partial r^2} + \frac{2}{r}\frac{\partial C}{\partial r}\right) \qquad (2\text{-}16)$$

Blake [48] has solved equation (2-16) neglecting convective term (i.e., $V \equiv 0$). To avoid the problem of the moving boundary in the diffusion equation, he assumed the bubble wall to be fixed in space, but allowed concentration of gas at the bubble wall, and the area of the

wall, to vary as they would if the bubble wall were moving. For his solution he assumed that variation of bubble diameter is sinusoidal and small.

Several solutions are found under different types of boundary conditions by several other investigators. Equation (2-16) cannot be solved unless bubble growth is known precisely. Hsieh and Plesset [50, 51] assumed small amplitudes of oscillating acoustic fields, and gave a solution for large times.

A solution that is free of these restrictions has been obtained by Eller and Flynn [52] considering the problems of motion and of diffusion as two separate problems rather than as two aspects of a single problem. Exact computer calculated solutions of the non-linear equation of motion

$$\ddot{R} + \frac{3}{2R}\dot{R}^2 = \frac{1}{\rho R}\left[P_i - \frac{2\sigma}{R} - P_H + P_A \sin \omega t\right] \qquad (2\text{-}17)$$

were obtained through a joint program with the Acoustic Research Laboratory at Harvard University. The diffusion equation (2-16) is then treated in such a way that a formal solution may be obtained for the flux of gas into the bubble for any general oscillatory solution R(t), of the equation of motion with boundary and initial conditions

$$C(r, 0) = C_i \qquad r > R$$

$$\lim_{r \to \infty} C(r, t) = C_i$$

$$C(R, t) = C_s \qquad t > 0$$

where C_i is the initial uniform concentration of gas, and also the concentration of gas at infinity, and C_s is the concentration of gas in the liquid at the bubble wall. C_s will change with time as the bubble slowly changes in size. Their only approximation, thus, is the assumption of C_s as constant. Results are given [52] for very small variations of acoustic pressure (i.e. $\pm$ 0.3 bars) and air saturated water at atmospheric pressure and temperature.

Diffusion of Gas During Expansion

An attempt is made here to solve bubble dynamics and gas diffusion differential equations simultaneously and numerically to investigate the effect of air content of water on the growth of bubbles. The following assumptions were made:

(1) Henry's Law is applicable;

(2) The process can be assumed isothermal.

General bubble dynamics equations can be arranged as follows [60, 61, 62]:

$$\rho R\ddot{R} + \frac{3}{2}\rho \dot{R}^2 = P_A \sin \omega t - P_H + P_v + P_g(t)\left(\frac{R_o}{R}\right)^{3\gamma} - \frac{2\sigma}{R} - 4\eta \dot{R}/R \qquad (2\text{-}18)$$

where P_H is the hydrostatic pressure, P_v is the partial vapor pressure of the liquid, P_g is the partial pressure of gas inside the bubble and η is the viscosity of the liquid and γ=1 for isothermal expansion.

Pyun [14] working in this laboratory, and others solved equation (2-18) numerically, assuming that a free bubble of radius R_o exists in the liquid. In their analysis no diffusion of gas is allowed. Since

theory of stabilization of nuclei in conical pores [34] seems to be more logical (see Appendix C), existence of nuclei in such unwetted acute angle pores will be now assumed. Surface tension will then help to expand the cavity rather than contracting it, and thus no gas will diffuse out of the nucleus. When under equilibrium such a nucleus will satisfy

$$P_{go} = P_H - P_v - \frac{2\sigma}{R_i} \tag{2-19}$$

where P_{go} and R_i are partial pressure of the gas in the liquid and radius of bubbles under equilibrium before any expansion starts. Figures 2-7 and 2-8 show the bubbles before and after nucleation in two sizes of conical pores.

In equation (2-18), it is implicitly assumed that vapor pressure of the liquid remains the same during expansion, i.e., evaporation of liquid into the cavity will be allowed without any temperature effects on the system. As the bubble starts growing, diffusion of air into the bubble will start due to the decrease of air concentration inside the bubble.

For gas to be stabilized in a conical crevice, the following conditions must be met [25, 63]

$$\alpha_R < \beta + \pi/2 < \alpha_A \leq \pi$$

where α_R = Receding contact angle

α_A = Advancing contact angle.

The position of the interface for the larger and smaller crevices are

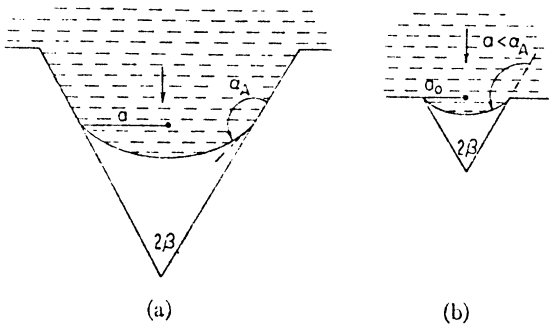

Figure 2-7 Crevices in a Degassed Liquid (a) Larger than Critical Size, and (b) Smaller than Critical Size.

5007

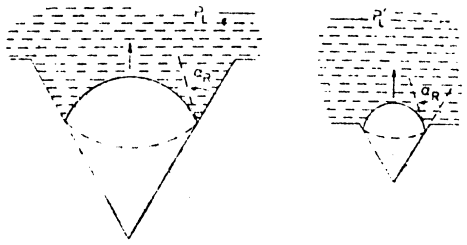

Figure 2-8 Cavity Nucleation from a Crevice (a) Larger than Critical Size, and (b) Smaller than Critical Size.

5008

given by

$$a = R_i \left| \cos (\alpha_A - \beta) \right| = a_c$$

$$a_o = R_i \left| \cos (\alpha - \beta) \right| \qquad \alpha < \alpha_A$$

Thus, depending on the values of α_A, α and β, which are properties of the solid-liquid system, values of a and a_o may vary between zero and R_i. If a_c is larger than the available crevice size in the system, the interface will stay at the crevice mouth.

When the expansion starts due to decrease in liquid pressure, larger and smaller crevices behave differently (see Appendix C).

For the purposes of simplicity it is assumed that a spherical bubble of radius R_o exist in the liquid. The partial pressure of gas inside the bubble, however, will be equal to the partial pressure of the gas in the liquid, which is the case for a gas bubble in a pore. Expansion of the bubble will not start until the pressure inside the bubble exceeds the liquid pressure. Collapse of a bubble at radius R_o will not be considered at this point. A static equilibrium will be assumed rather than a dynamic one for the purposes of simplicity at the beginning of the expansion starting at R_o.

Consider the time required for the acoustic pressure to reach a value necessary to balance the right side of the following equation:

$$P_A \sin \omega t = P_H - P_v - \gamma_v P_{go} + \frac{2\sigma}{R_o} \qquad (2\text{-}20)$$

This time is

$$t = \sin^{-1}\left[\frac{P_H - P_v - \gamma_v P_{go} + \frac{2\sigma}{R_o}}{P_A}\right] \cdot \frac{1}{\omega} \qquad (2\text{-}21)$$

where γ_v is the ratio of volumes of bubble when it is under static equilibrium and when its radius is R_o. Then,

$$P_A \geq P_H - P_v - \gamma_v P_{go} + \frac{2\sigma}{R_o}$$

is required for the expansion to start.

Equations (2-16) and (2-18) are solved simultaneously using fourth order Runge-Kutta method for bubble dynamics equation (i.e., equation (2-8)) and DuFort-Frankel numerical integration scheme for diffusion equation. Formulation of the problem is given in Appendix D. Figure 2-9 summarizes the results of the calculations for one cycle of the acoustic field.

The radius of nucleation, R_o, is a function of crevice size, wetting angles and gas concentration, in the system when dynamic effects are neglected. For smaller crevices than critical size, R_o is a function of crevice size and wetting angles. For larger crevices, R_o, is not only a function of wetting angles and size, but also is a function of gas concentration in the sample. Thus for large crevices, degassing should be more effective. For smaller crevices, dependence of nucleation pressure on the gas content is due to gas partial pressure, P_{go}, in equation (2-20). Since there are larger nuclei in ordinary tap water, as compared to filtered tap water, variation of inception pressure by air content is expected to be more in tap water.

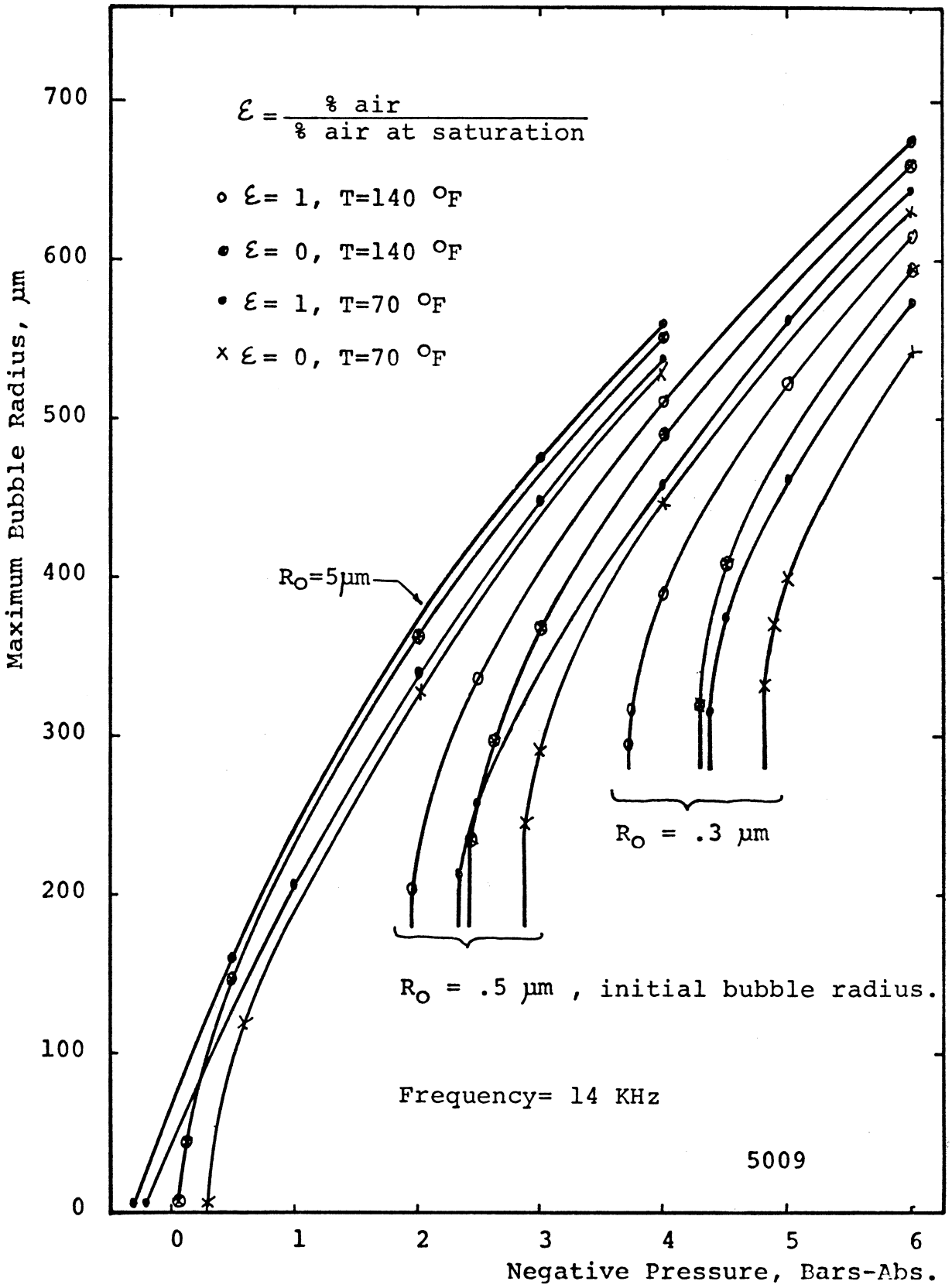

Figure 2-9 Expansion of Bubble in one Cycle as a Function of Initial Buble Radius and Negative Liquid Pressure.

Effect of Radiation

Glasser [64] observed nucleation by radiation in superheated diethylether. His work is reviewed by Fretter [65]. Since then, bubble chambers have been employed in the field of high energy physics to study the interaction of ionizing radiation. Bubble chambers utilize the instability of superheated liquids to provide bubble formation. The same mechanism is, of course, also operative in the liquid coolant channels of a nuclear power reactor. Liquid may be superheated on the smooth surfaces of cladding on fuel rods. Large superheats may cause sudden evaporation of liquid and damage the cladding. Neutron irradiation may help prevent large superheats in water reactors.

Study of nucleation in superheated water and ethyl alcohol by different types of nuclear particles were undertaken by Whitehouse and Pilati [66, 67] recently.

Following Seitz [68] and Whitehouse [66], and neglecting kinetic energy of expansion, energy, E_m, required to create a bubble of radius R is given by

$$E_m = 4\pi\sigma R^2 + \frac{4}{3}\pi R^3 \rho_v h_{fg} + \frac{4}{3}\pi R^3 (P_H - P_i) \qquad (2\text{-}22)$$

in which ρ_v is the density of vapor inside the bubble at pressure P_i, h_{fg} is the latent heat.

ρ_v and P_i can also be written as

$$\rho_v = \frac{2\sigma/R + P_H}{R_{steam} T} ,$$

$$P_i = \frac{2\sigma}{R} + P_H$$

where R_{steam} is the gas constant for vapor and T is the temperature. In the derivation of equation (2-14), it has been assumed that (i) the initial bubble is formed so quickly that no energy is transferred to the surrounding water, (ii) the formed bubble is stationary, and (iii) the process is isothermal.

It may be noted that equation (2-22) is relatively sensitive to both $P_i - P_H$ and to σ, decreasing with increasing values of the first and decreasing values of the second. Thus, as temperature increases, E_m decreases. Increasing temperature has the same effect as decreasing hydrostatic pressure. For radiation-induced nucleation, two conditions must be satisfied:

i) Energy of ionizing particles must be greater than required nucleation energy, E_m,

ii) The required nucleation energy must be deposited in a distance comparable to the critical radius.

Since the second requirement is the controlling factor, the energy deposition rate

$$\frac{dE}{dx} \geq E_m / L \qquad (2\text{-}23)$$

where L is the effective energy deposition length, is controlling.

A widely accepted theory [66] describing the mechanism of energy transfer between the ion and the medium through which it travels was proposed by Seitz [68]. It is envisioned that the particle

experiences innumerable electromagnetic interactions with the atoms along its path. The interactions leave the electronic structure of the atoms in a highly excited state. Actual ionization may or may not occur. In either case, the energy imparted to the electronic structure eventually appears as heat in the existing vibrational modes of the molecular structure. This sudden appearance of highly localized heat energy is called a "thermal spike". This thermal spike produces a subvisible, cylindrical vapor wake along the particle's path. This vapor wake, according to Raleigh [74], breaks up and forms spherical nuclei, due to surface tension. Thus the radius of nuclei will be dependent on where these wakes occur. His conclusion is that effective energy deposition length is about $2\pi R$. Thus, energy deposition rate U, should be

$$U \cong \frac{E_m}{2\pi R} \geq \frac{2}{3} R(\sigma + R\rho_v h_{fg}) \qquad (2\text{-}24)$$

Figure 2-10 gives the required energy deposition rates as a function of critical radius and negative liquid pressure. Figure 2-11 gives stopping power of several ions in water [67]. As it is seen, the only candidate for the nucleation mechanism is the oxygen atom, and it has maximum energy deposition rate when its energy is about 10 Mev.

The energy spectrum of Pu-Be source used in the present experiments ranges from 1 to 10 Mev. Thus energy of oxygen nuclei atoms will range from zero to ~ 2.21 Mev. for a monoenergetic neutron of 10 Mev.

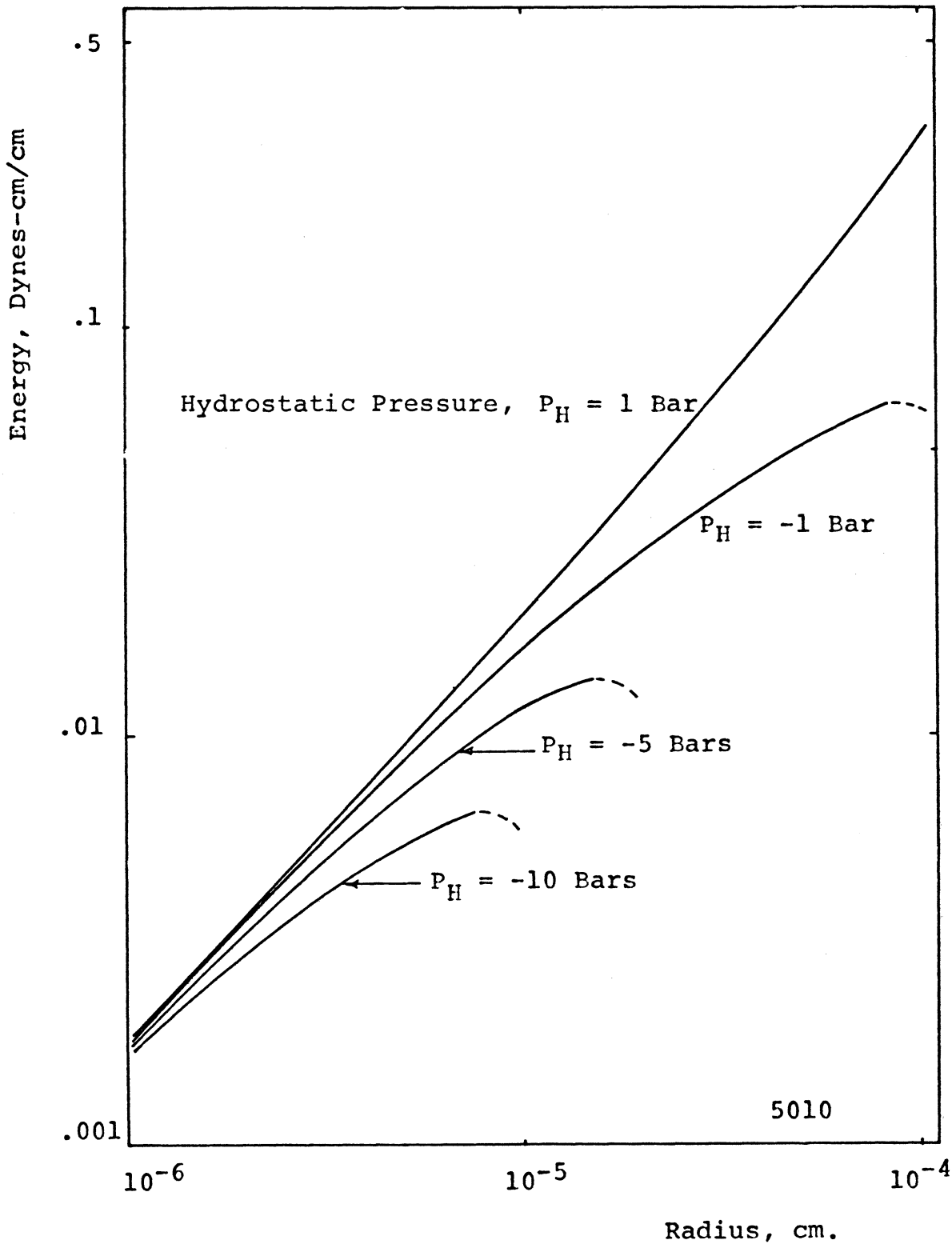

Figure 2-10 Required Energy Deposition Rate to Generate a Vapor Bubble of Radius R.

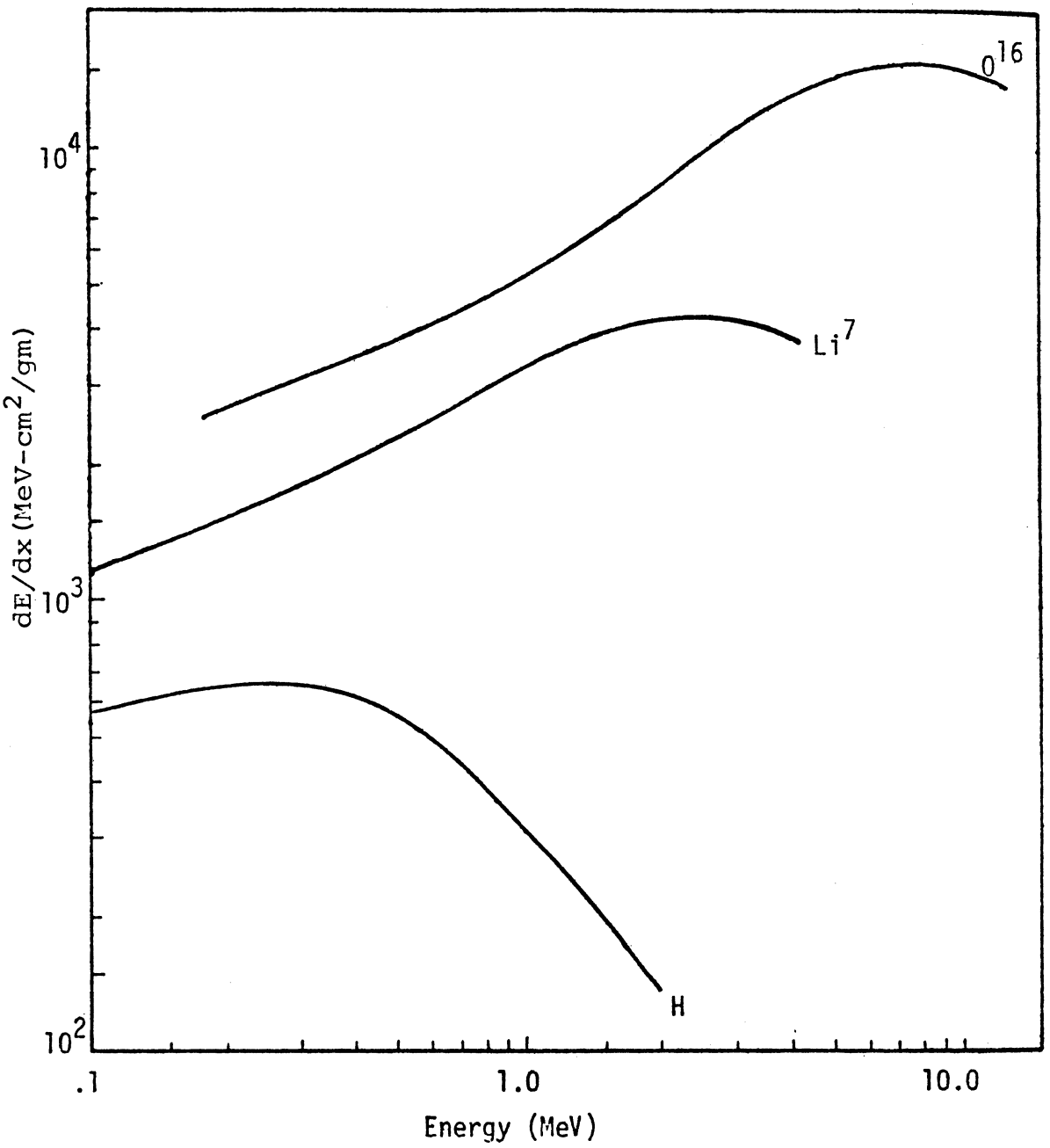

Figure 2-11 Stopping Power of Several Ions in Water.

5011

From Figure 2-11 for a 2.2 Mev oxygen knock-on ion, energy deposition rate is about 10^4 Mev-cm^2/gm or 1 Mev/μm or 0.024 dynes-cm/cm for water. Using equation (2-16) for P_H = 1 bar, T = 530°R, R_{steam} = 85.77 ft-lb/lb-°R, h_{fg} = 1053 Btu/lb, σ = 72.5 dynes/cm, bubbles of about 0.1 μm radius will be created in water at room temperature. Thus, in order that these nuclei will grow, negative pressures of about

$$\frac{2\sigma}{R} \cong 15 \text{ atm.}$$

are required. In practice negative pressures of less than 15 atmospheres are observed [77, 78, 79]. Of course, it is also possible that the energy contributed by irradiation will simply contribute to the growth of already existing nuclei, allowing them to attain the critical radius necessary for further growth.

Sette and Wanderlighn [75] reached the conclusion that 1000 Mev/cm or less energy deposition rates for any ions were not enough to cause nucleation. The only ions which exist in water are either hydrogen or oxygen. Hydrogen ions are not able to deposit energies at a rate higher than 10^3 Mev/cm. The oxygen recoil nuclei are, therefore, the only secondary particles which may produce cavitation nuclei in water according to Sette and Wanderlighn [75]. Excluding dynamic effects, their experimental results require that nuclei of about 1 μm be created by radiation. It is to be noted that ionizing radiation produces in water not only local overheating, but radiolytic effects as well. OH^- and H^+ free radicals are formed along the path

of ionizing radiation. This situation may lead to reactions among free radicals of the same kind with production of H_2 and O_2 molecules.

The creation of microbubbles in liquid, induced by high-energy ionizing particles is examined from the thermodynamic point of view by the same authors [76]. It is shown that dissolved gas lowers the amount of energy required for the creation of nuclei. A threshold value for the initiation of an exothermic process exists if an ionizing particle passes through water containing dissolved gas.

Effect of Magnetic Field

An effect of a magnetic field on cavitation erosion is reported by Perel'man and Govorskii [15]. A magnetostriction vibrator was used to achieve erosion of the specimen by cavitation in an "electrically-conducting" liquid. A magnetic field of 236 Gauss was produced by an electromagnet. Weight loss rate of the specimen decreased considerably when a magnetic field was applied. It was also observed that, during Perel'man's experiments, temperature of specimen rose from 450° C to 900° C, during the tests. This temperature rise is explained mainly by the liberation of heat when the conducting liquid intersected the magnetic field.

Another effect of a magnetic field on the extent of cavitation damage and its intensity on a circular cylinder in a water tunnel is reported by Shalobasow and Shal'nev [100]. The effect of magnetic field was to increase the size of damage done, and cause the pits to

appear earlier during the test. The weight loss rate was also found to be increased during incubation period under magnetic fields. The increase on the cavitation damage is attributed to the charged cavities which is calculated to be carrying electric charge density of $(6\text{-}7) \times 10^{-4}$ amp-sec/m^2 at 20 m/sec water flow speeds in the water tunnel.

If sufficiently large electric charge density exist around nuclei, they may contribute to heat up the system when they repeatatively cross the magnetic field in an acoustically induced pressure field.

CHAPTER III

EXPERIMENTAL APPARATUS AND INSTRUMENTATION

Experimental Setup

The experimental setup consists mainly of ten groups: water loop, ultrasonic horn system, Coulter counter system, light scattering system, inception pressure measuring system, inception detection system, electro-magnet system, flow measuring system, pulse-peak detection and gating system, and pulse processing system. Significant circulation of water is required, as opposed to the Coulter counter system, for the light scattering system to measure nucleus spectrum. Flow velocity should be low so that no new nuclei by entrainment, etc. will be generated due to the water circulation. Figure 3-1 is an over-all view of the experimental setup. A schematic diagram of the system is given in Figure 3-2.

The Coulter counter system is installed as close as possible to the light scattering system so that the water samples measured will be as closely as possible the same. The distance between two nucleus spectrum measuring systems was less than four inches.

Water Loop

Figure 3-3 shows a partial view of the water loop including stilling tanks. Water is filled from a connector at the top of the stilling tank no. 2. These glass stilling tanks are about one foot in diameter and two feet in height, providing a total water-holding capacity of about 90 liters. A stay time of at least seven minutes was thus obtained at

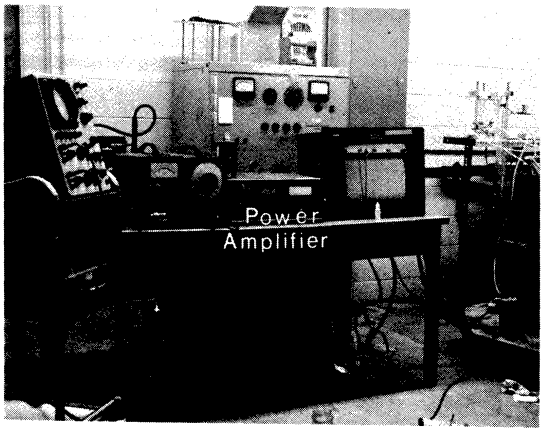

(b) Cavitation Generation and Inception Detection Equipment.

Figure 3-1 Overall View of the Experimental Apparatus and Equipment.

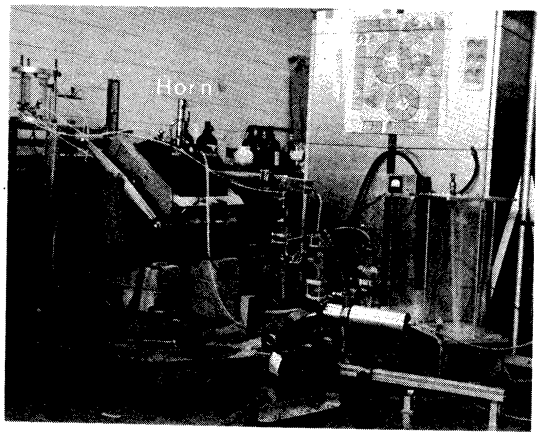

(a) Water Loop and Electro-Magnet.

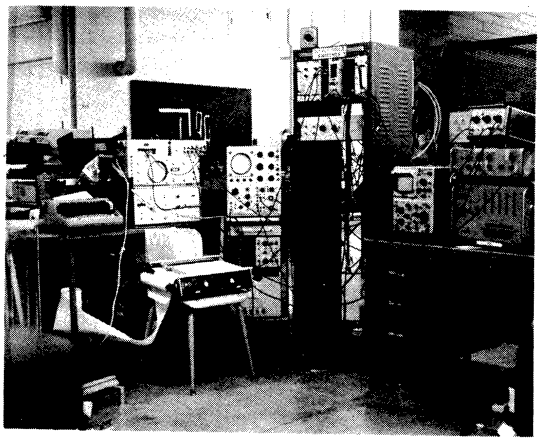

(c) Multi-Channel Analyzer and Pulse Shaping System.

5012

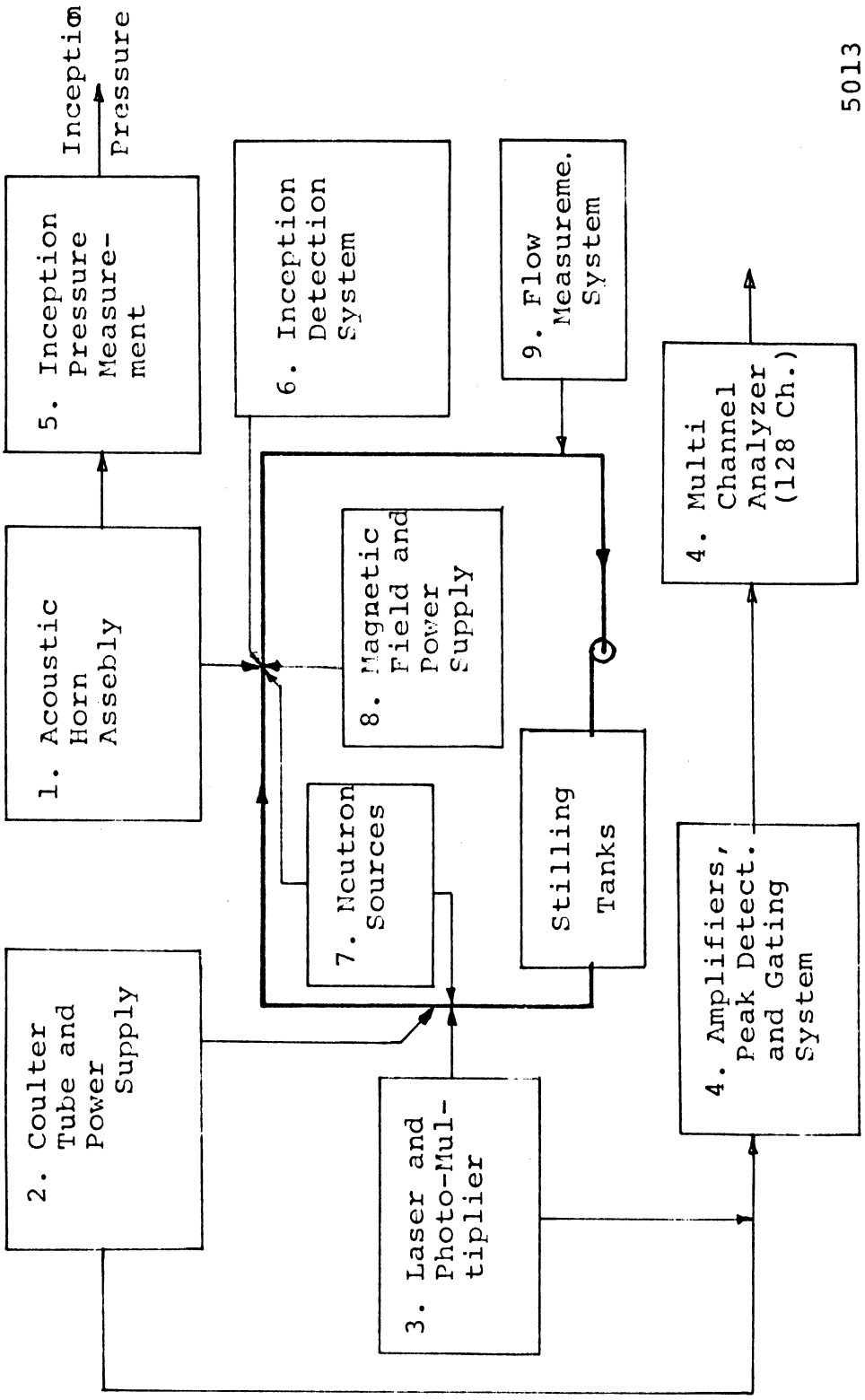

Fig. 3-2. Schematic diagram of the experimental setup and instrumentation.

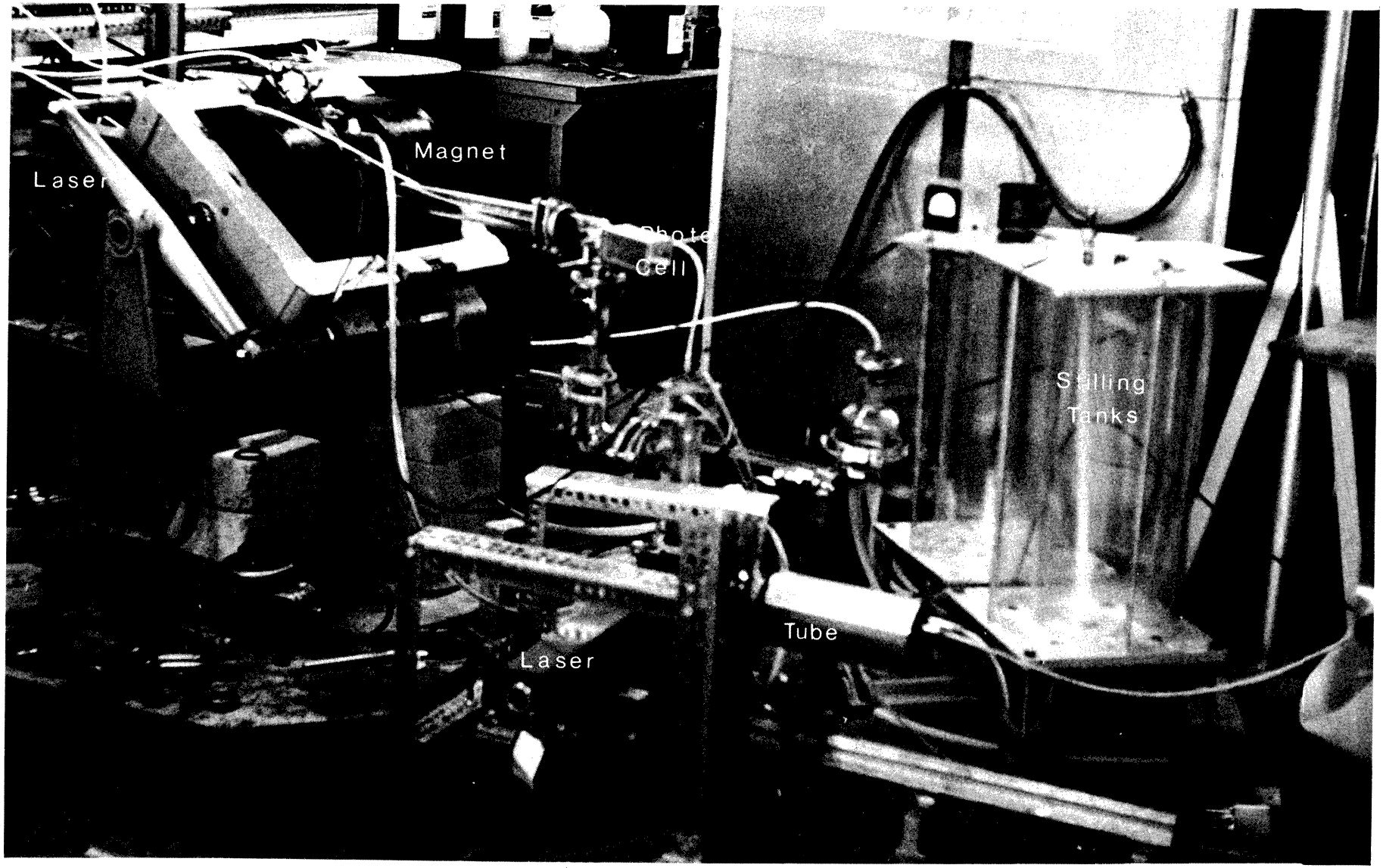

Figure 3-3 An Enlarged View of the Test Section and Instrumentation on it. 5014

the highest flow rate used for the water samples. Tank no. 1 houses a two-element 1.3 kw (at 150 volts) immersion heater. Both tanks are baffled to provide maximum chance for large bubbles to float to the surface. A concentric reducer is also used before water enters into tank no. 1 to reduce entrance speed of water to the tanks. The reducer is seen in Figure 3-4. A schematic of the water loop is given in Figure 3-4. A main loop was constructed using 1-1/2" I. D. Pyrex glass tubing. The use of small diameter tubing was avoided to reduce the flow velocity. Four 5/8 inch O. D. polyethylene tubings were used to connect the tanks and the reducers together. All air-extraction piping were 1/4 inch O. D. polyethylene tubing. Water contact with metals was avoided to prevent corrosion. Only the connectors for the 1/4 inch and 5/8 inch O. D. tubing, and the top and bottom plates for the stilling tanks were of metal. The connectors were of brass and the three plates for the tanks of anodized aluminum. The heater plate was of tinned brass and the heater was soldered to the plate. The heater has incoloy elements which are non-corrosive in water, as are in general all the other metallic elements discussed above.

Flow rate is varied using a variac controlled plastic centrifugal pump, having no metal parts. Inlet and outlet connectors were 1/2 inch I. D. The pump is driven by a 1 hp variable-speed electric motor, which was an integral part of the pump.

A turbine flow meter of about 1/2 inch I. D. measures flow rate. Thus the smallest I. D. in the loop is 1/2 inch. To achieve a uniform flow at the measuring points, a honeycomb flow straightener is used.

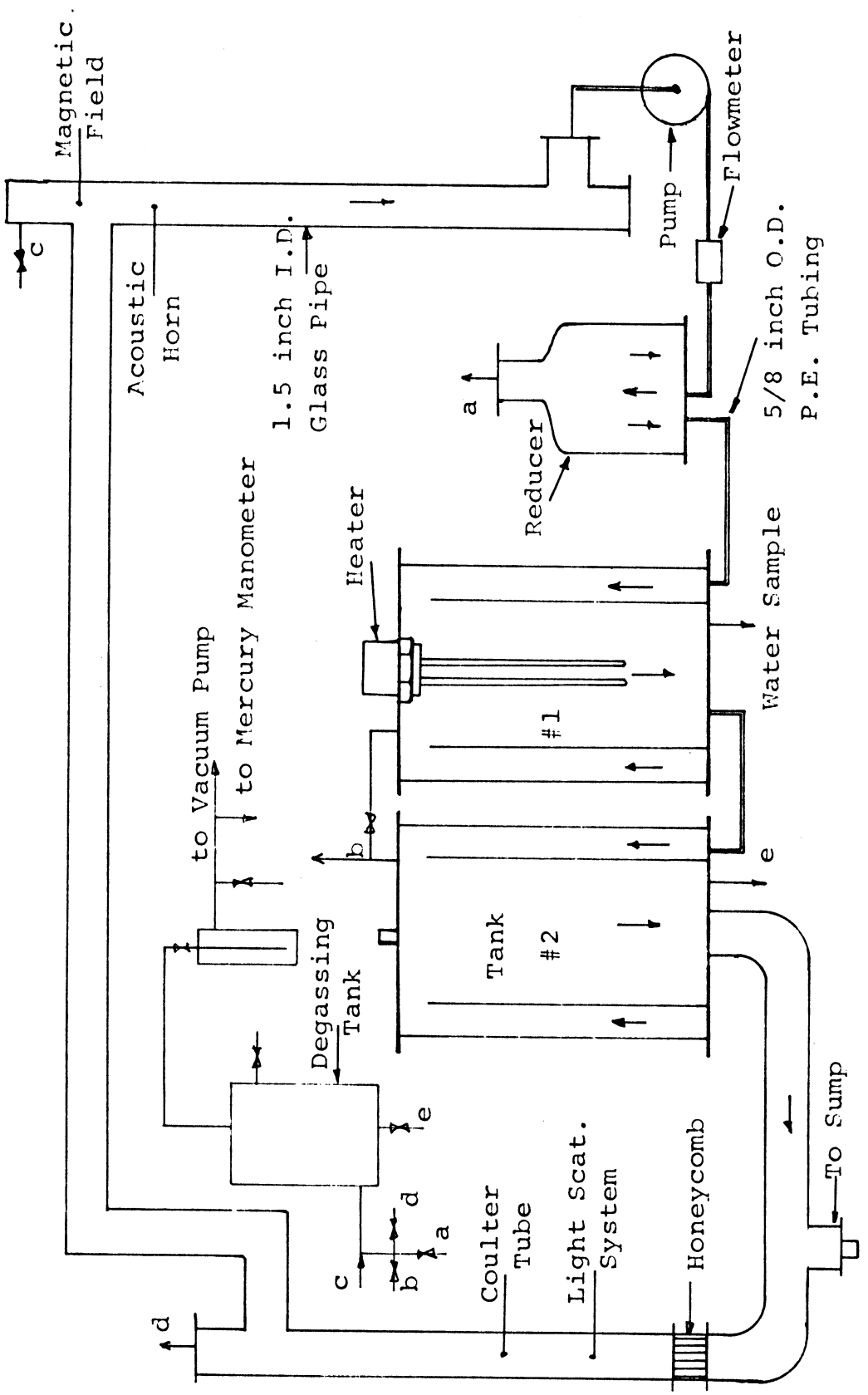

Fig. 3-4. Schematic Diagram of the Water Loop.

A plexiglass pipe of about 1-1/4 inch length was installed, with a movable brush attached, just at the position of the aperture of the Coulter tube. This brush is used to clean the aperture as necessary. Water temperature is controlled (and measured) by a thermocouple in tank no. 2, and an electronic recorder connected to the heater.

Acoustic Horn Assembly

The acoustic horn assembly here used was originally designed by Garcia [81], and later used by Nystrom [27] and Pyun [14] in this laboratory. The transducer horn assembly which is used in this investigation is shown in Figure 3-5. Nystrom's explanation will be given here to understand how the assembly operates.

Two lead-zirconate-titanate (PZT-4) crystals, separated by an aluminum spacer which serves as an electrode, are connected to the aluminum sleeve by an internal bolt which passes through the steel counter weight, crystals, and the spacer, and terminates in the aluminum section. The internal bolt is electrically insulated from the crystals and aluminum spacer so that the steel counter weight, the upper surface of the lower crystal are electrically the same point (ground). The second electrode is attached to the upper steel counterweight. The surfaces of the crystals are silver plated to provide electrical contact between the crystal surfaces and the metal surfaces of the aluminum electrode and the transducer assembly. The exponential horn is attached to the aluminum section by means of an internally threaded rod. This allows easy removal of the exponential horn from

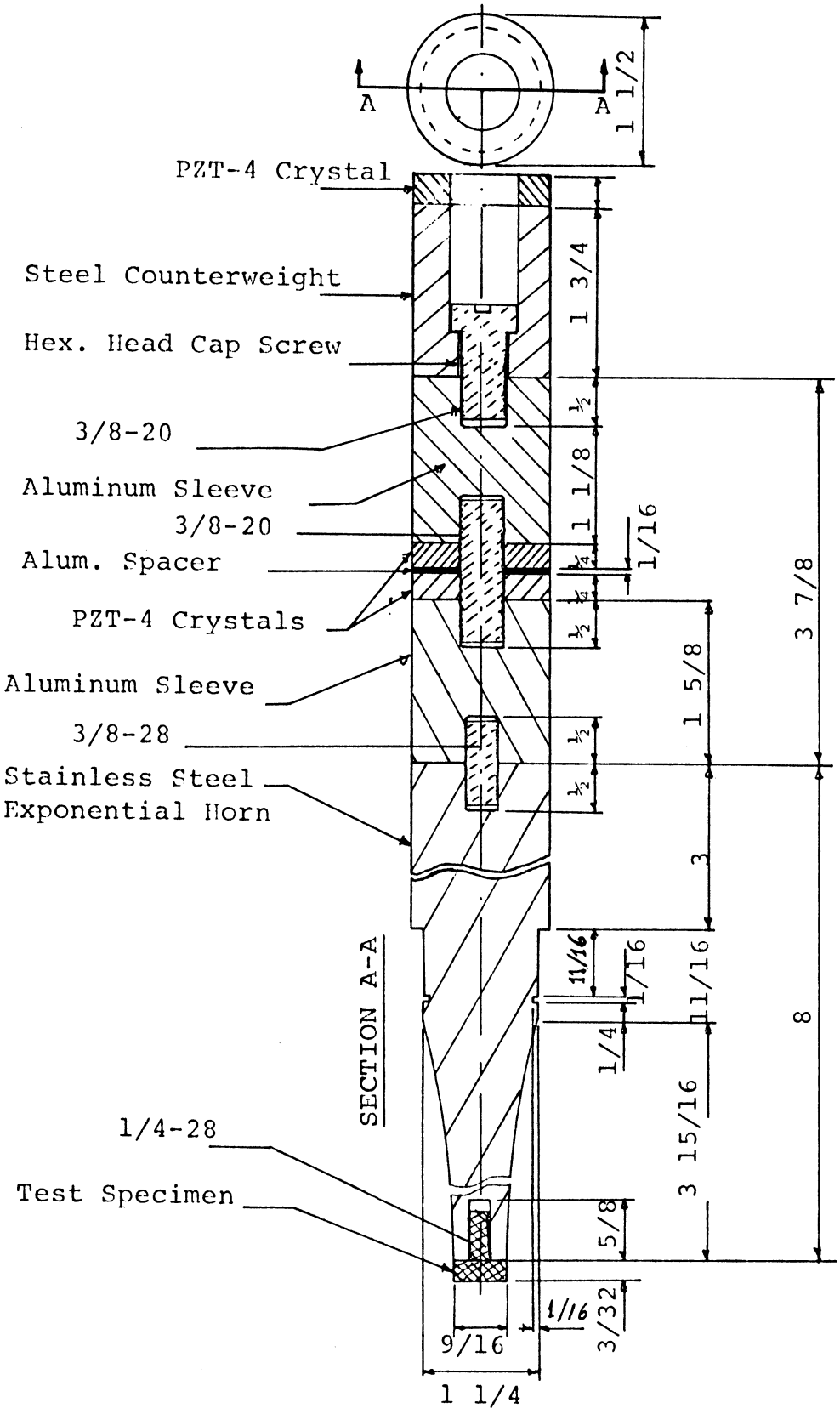

Figure 3-5 Exponential Horn and Transducer Assembly.

5016

the transducer assembly, without disturbing the crystal assembly.

One of the important considerations in the design of a transducer horn assembly is the transfer of the acoustic energy from the crystals to the tip of the exponential horn. To realize an efficient transfer of energy, it is necessary to achieve a proper acoustic match between the various materials making up the assembly. If one considers the reflection and transmission of plane waves at the plane interface of two materials, the reflection coefficient approaches zero and the transmission coefficient approaches unity as the acoustic impedances of the two media approach one another. The acoustic impedance of a medium is the product of its density and the velocity of sound in the medium. Since there is a large difference between densities and elastic moduli of materials, acoustic impedances can also differ substantially. Using aluminum for the center section of the assembly, between crystal and stainless steel exponential horn, a reasonably close match is obtained. In addition to using smoothly ground surfaces at each component interface, a thin layer of a compound such as silicone should be applied to each surface prior to assembly to prevent air gaps from remaining at the interfaces.

Dimensions of the various section of the assembly are important in the design of such a transducer assembly. Typically, the length of the upper section and the length of the exponential section each correspond to half the wavelength of the acoustic wave propagated in it. Figure 3-5 is a drawing of the exponential and sonic transducer assembly used in the experiments. The total length of the assembly is one

wavelength. The amplitude of this waveform represents the vibrational displacements produced by the axial dilation motion of the crystals. Therefore, the tip of the horn should correspond to an antinode so that maximum tip displacement can be produced. Since the horn assembly must be physically supported, the support attachment should be at a node in order to minimize any damping which may be produced by the support structure. Due to symmetry the aluminum spacer electrode located between the two crystals must be a nodal point. The velocity of sound in aluminum and stainless steel is approximately 16,000 ft/sec. Therefore, it is possible to compute the required length of the assembly given the applied frequency, or to compute the frequency, given the length. The length of the transducer assembly used in those experiments is ~ 1 4 inches. The resonant frequency of this assembly was calculated to be ~ 13. 7 KHz (i. e. $c = f\lambda$). Measured resonant frequency was 14.1 KHz.

A counterweight crystal attached to the top surface of the horn assembly was used to measure displacement of the horn tip, indirectly, or pressure wave amplitude in the water.

The transducer horn assembly was driven by a sine wave generator. Figure 3-6 is a schematic of the transducer assembly and associated system. Switch S_1 was used to protect the counterweight crystal and horn assembly when the amplifier was activated. It was observed that, sometimes, pulses large enough to damage the counterweight crystal are generated when the amplifier is started. Double amplitude of about 2 mils ($\sim 51\mu$) at the horn tip was obtained at peak

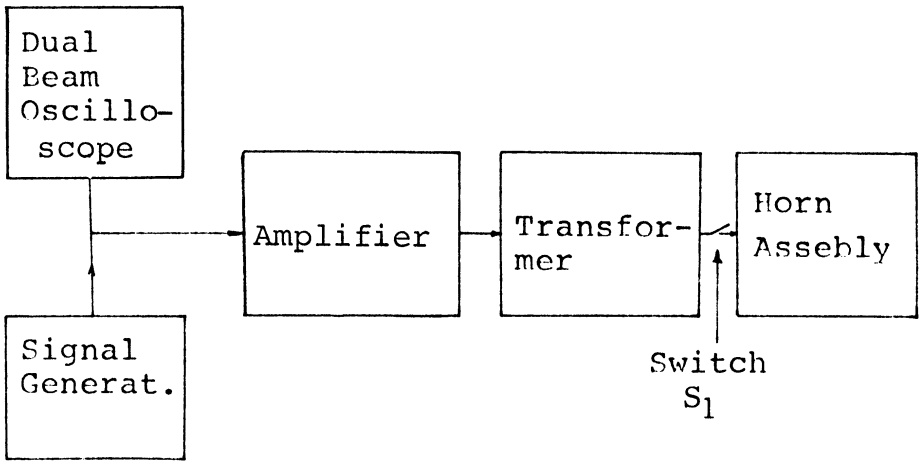

Fig. 3-6. Schematic Diagram of the Acoustic Horn Assembly and Associated System.

5017

power of the amplifier.

Impedance matching between amplifier and transformer, and transformer and exponential horn assembly, is very important for the purposes of adequate power transfer. Figure 3-7 gives maximum power output versus load resistance for the power amplifier. Thus, load resistance should be between 3 and 4 ohms for maximum transfer of power from the amplifier to the transformers. Further details are given in Appendix H.

Coulter Counter

Introduction

Figure 3-8 shows the Coulter tube as assembled in the system and Figure 3-9 provides further details of the assembly itself. The position of the electrodes are also shown along with the Coulter tube. The overall Coulter tube assembly is installed downstream of the light scattering system. The Coulter tube was positioned inside of 1-1/2 inch I. D. diameter glass tube which was shielded by meshed wire, and grounded to reduce electronic noise. Electrodes were of platinum to prevent any corrosion. The outside electrode of the Coulter counter was grounded, while the inside electrode was the hot side (+) of the constant voltage power supply.

Coupling Circuit

A Coulter counter assembly for the present purpose was originally designed here by Ahmed, and operated using a constant current power supply [13]. Since the original constant current power supply

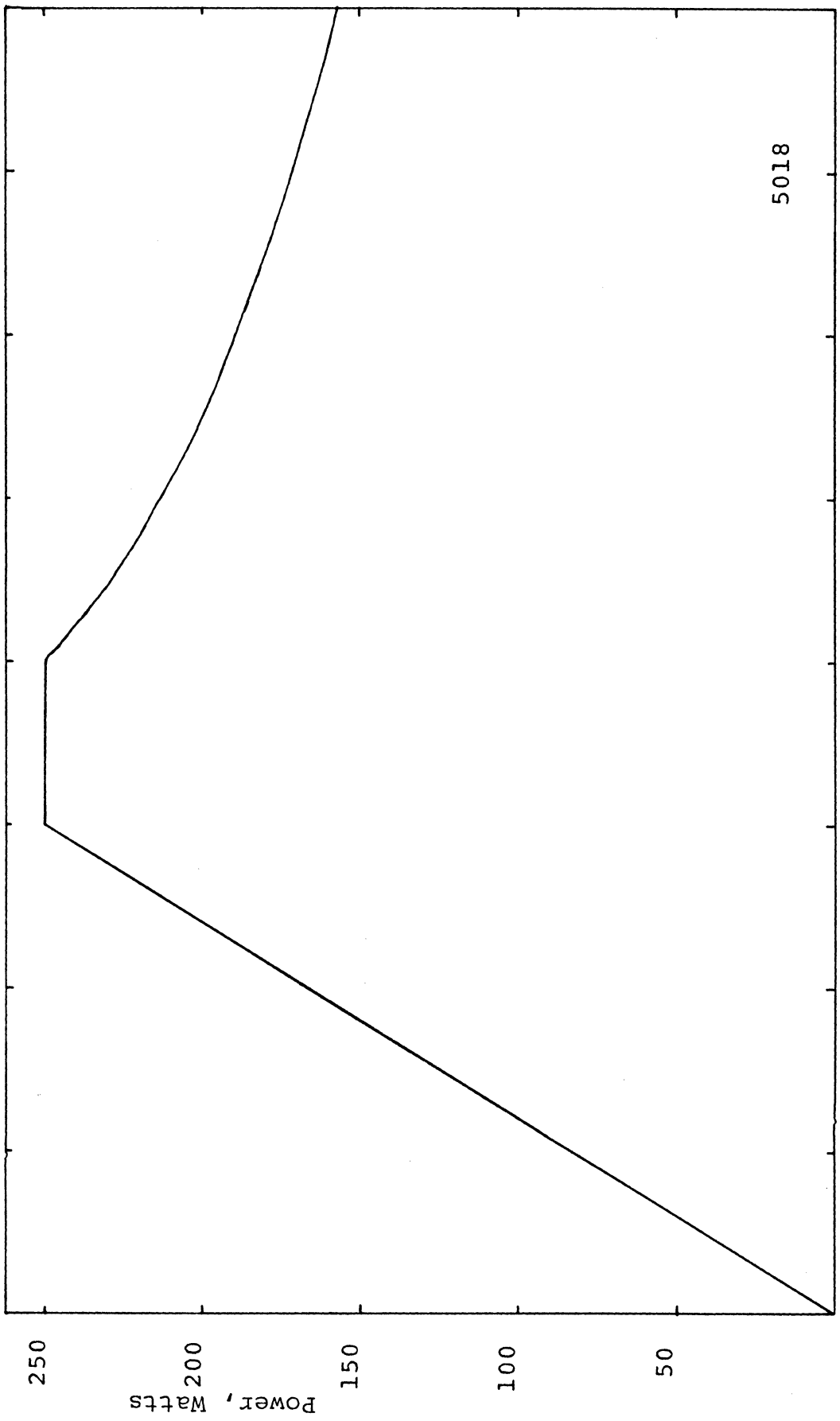

Figure 3-7 Maximum Output Power Versus Load Resistance.

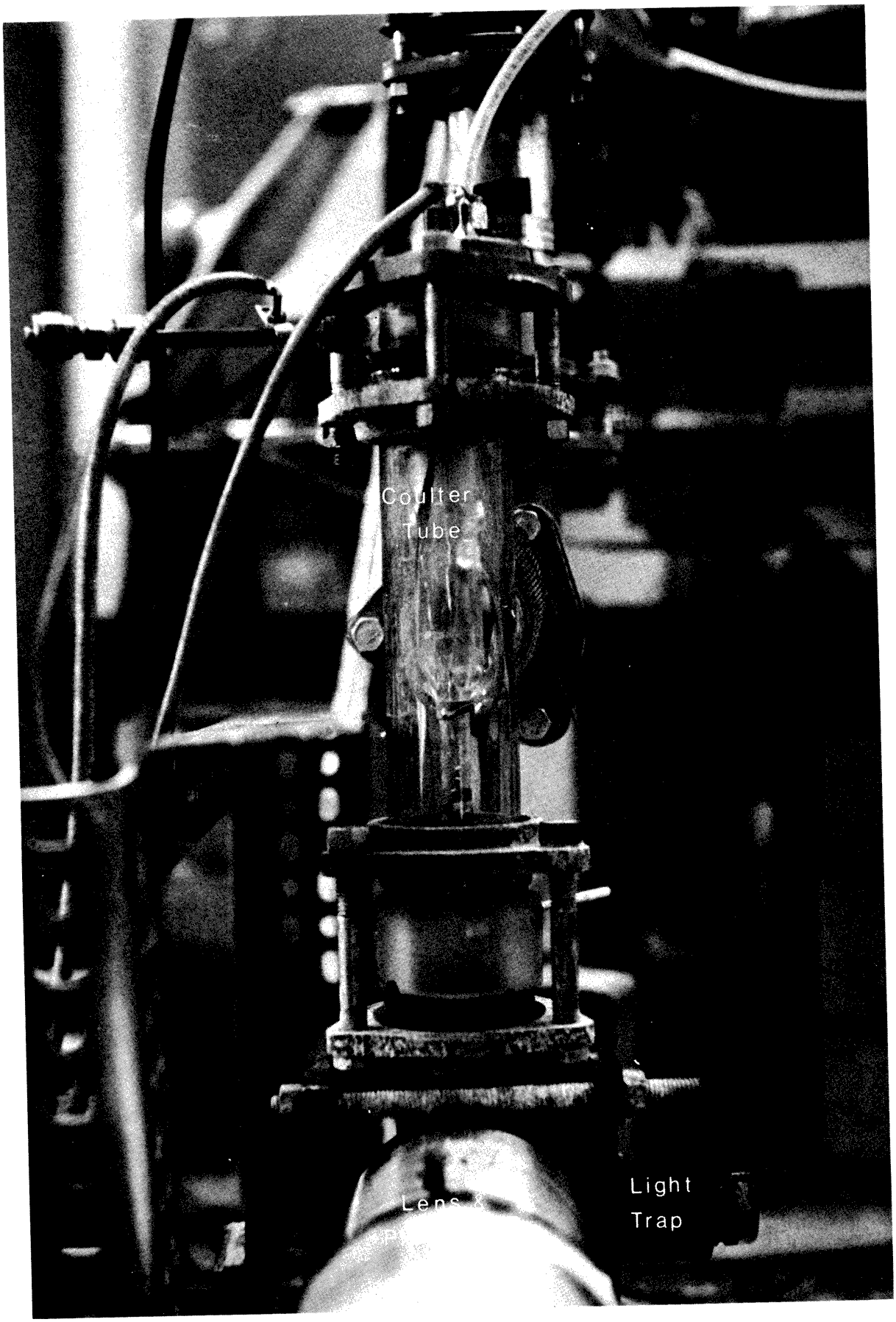

Figure 3-8 An Enlarged View of the Test Section. 5019

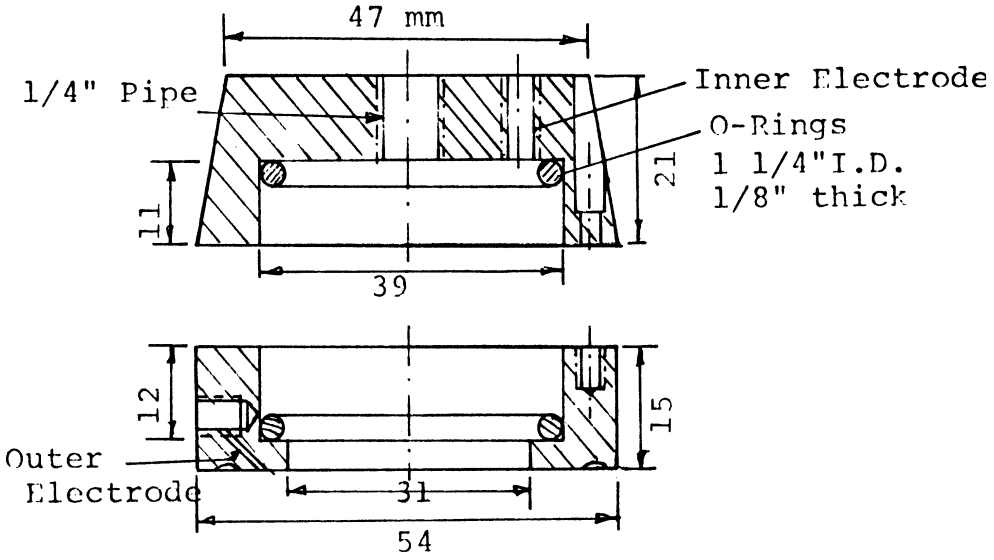

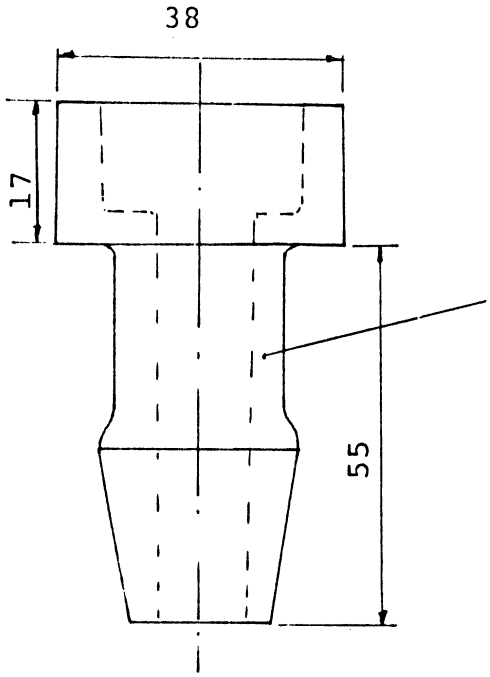

Figure 3-9 Components of Coulter Tube Assembly.

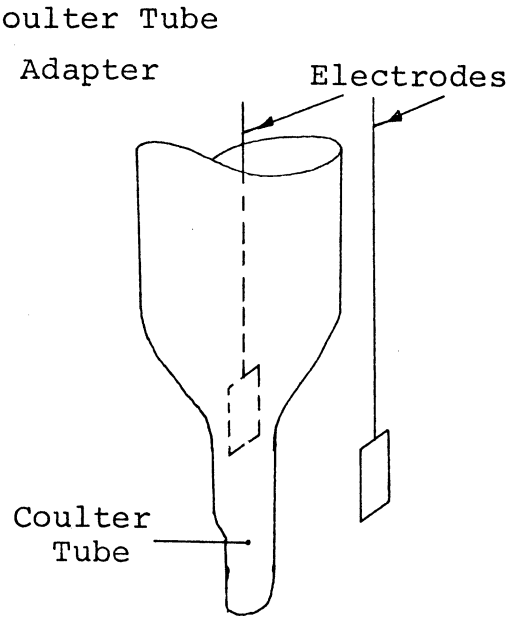

5020

was found to be noisy [14], a constant voltage power supply was used. Since the system consumes little energy, a 90 V battery was preferred to the power supply which was available for the reason that no 60 Hz ripple would interfere with the signal, and it would be noise-free. Figure 3-10 shows the coupling circuit used to convert resistance changes to voltage changes. R_c is the Coulter orifice resistance which is variable depending on electrolyte and Coulter tube orifice dimensions. When a particle enters into the orifice, R_c will be $R_c \mp \Delta R$ depending on the size and conductivity of the particle. It can be shown that for maximum voltage changes due to resistance change, $R = R_c\sqrt{1+\Delta R/R_c}$. Since $\Delta R \ll R_c$, $R \cong R_c$ will be optimum for the system. Table 3-1 gives the values of R used for different conductivities of electrolyte.

A Coulter tube with 70 μm diameter orifice has been used in all measurements to be able to measure the smaller nuclei required. Recommended nuclei diameter [20] is 5-40 percent of the aperture diameter for Coulter tubes. It was found that there were not many nuclei in the present loop having diameters larger than 25 μm.

Resistivity of electrolyte is measured using a resistance bridge. An electrode set having 1 cm^2 area with 1 cm between was used. Values of resistivities are assumed to be approximate. A 680 μF capacitor was used to block the D. C. voltage, which was about V/2 volts, where V is the power supply voltage.

Calibration

Calibration of the Coulter system was necessary, since there were too many variables affecting pulse height. An approximate calculation was used for the design of the calibration system. Using

$$\Delta R \cong \frac{\rho_o}{A^2} V,$$

where ΔR is the resitivity change, when a particle of volume V enters into the orifice of the Coulter tube, ρ_o is the resistivity of the electrolyte and A is the area of the orifice. For nuclei radius, r, and orifice diameter, d:

$$\Delta R = \frac{64}{3\pi} \frac{\rho_o}{d^4} r^3$$

For tap water, $\rho_o = 3800\,\Omega$-cm and for an orifice diameter of 70 μm

$$\Delta R \cong 41.2\, r^3$$

For a 5 μm diameter particle, $\Delta R \cong 170\,\Omega$. Voltage drop, ΔV, can be evaluated for tap water using $R = 620\Omega$ and $V = 90V$. Current flow will be $i \cong 45/620 = 72\,\mu a$, and pulse height $\Delta V = i\Delta R \cong 12$ mV.

The variables that influence pulse height are mainly resistivity of water, length and diameter of the orifice, and finally the particle itself. Since neither orifice length nor diameter is known accurately, the calculation will be inexact to the corresponding extent.

For the calibration of the system, latex particles of 5.02 μm diameter were used. Larger particles of latex and pollen are also available from Coulter Electronics. Pollens are found to be less desirable than latex, since latex has the larger resistivity. Paper

Mulberry, for example, was found to have very close resistivity to tap water so that it was useless for calibration purposes for tap water. Larger latex particles usually have very large standard deviation of particle size. The Coulter tube pulse height distribution for 5.02 μm peak diameter latex particles was obtained using a multi-channel analyser (MCA). The resulting pulse height distribution for the 5.02 μm diameter latex particles is given in Figure 3-11. The channel number of the MCA where the peak of the particle-size distribution is located, corresponds to 5.02 μm diameter for this latex particle sample. Corresponding pulse heights for different sizes of nuclei, thus, can be calculated using

$$V(r) = \frac{V(5.02)}{(5.02)^3} r^3$$

where V(5.02) is the pulse height corresponding to 5.02μm diameter nuclei. V(5.02), of course, can be read from the MCA calibration curve (Figure 3-12), since the channel number corresponding to 5.02 μm diameter is known.

Flow Rate Measurement

The orifice liquid flow rate is a necessary parameter for calculating the number of nuclei per unit volume of water. A 2cc volume is marked on the lower part of the Coulter tube. The time needed to collect 2 cc of water was measured for different pressure drops across the orifice. The results are given in Table 3-2. In most of the experiments, 15 cm-Hg pressure drop across the orifice was used for

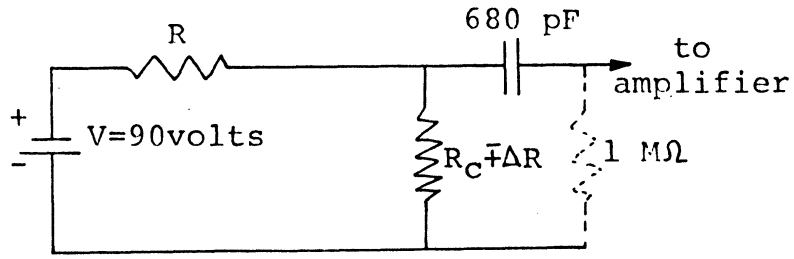

Figure 3-10 Coupling Circuit for the Coulter Counter.

5021

TABLE 3-1

VALUES OF R IN FIGURE 3-10

% Salt in Electrolyte	Resistivity of Electro-lyte Ω - cm	Value of R used, KΩ
Tap water	3800	620
Filtered tap water	3800	620
.05% saline water	1360	220
.1% saline	620	100
1% saline	95	15

5022

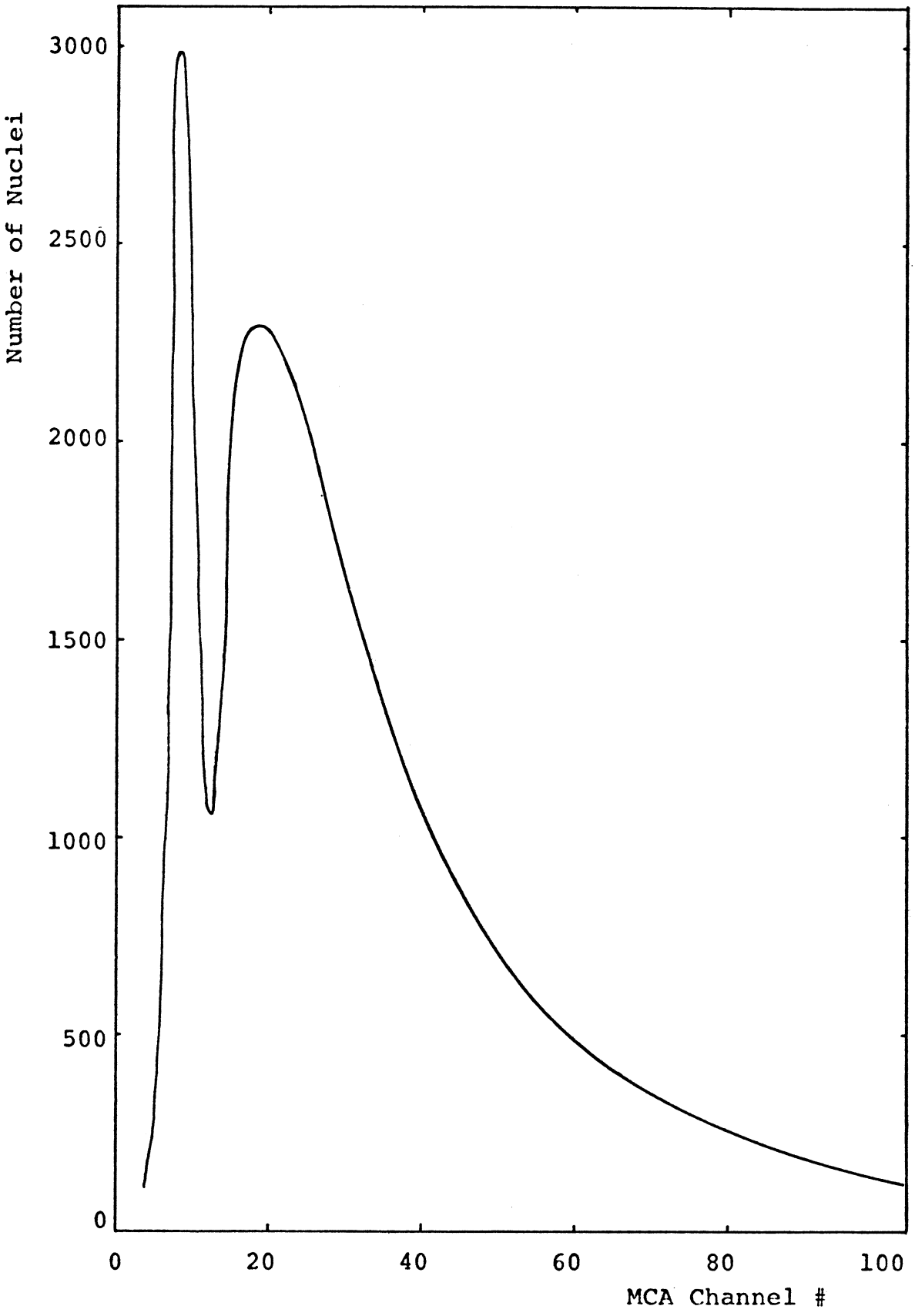

Figure 3-11 Pulse Height Distribution for the 5.02 μm Diameter Latex Particles.

5023

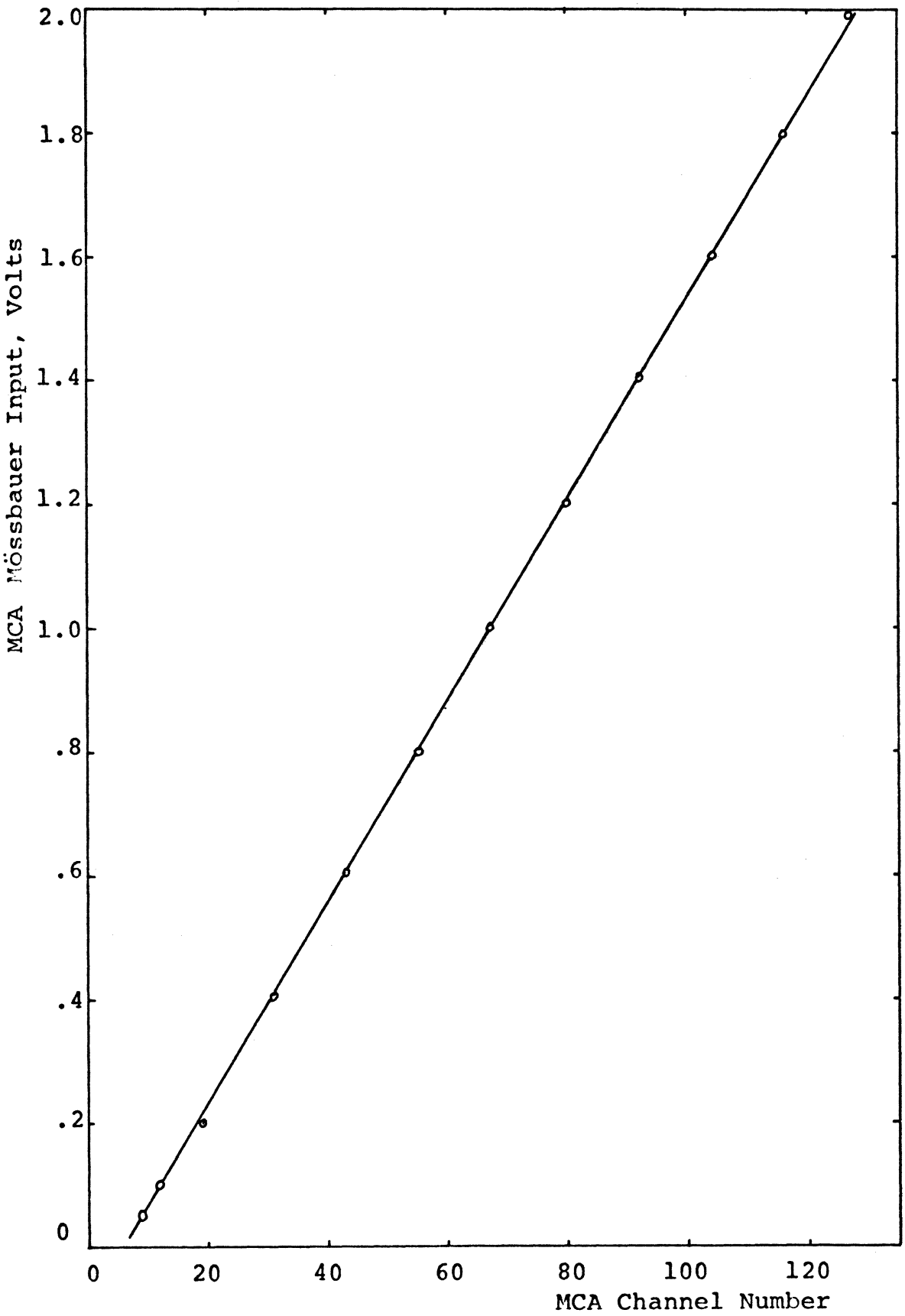

Figure 3-12 Calibration Curve for Multi-Channel Analyzer.

consistency.

TABLE 3-2

PRESSURE DROP ACROSS ORIFICE VERSUS FLOW RATE

Δ P Cm-Hg	Flow Rate cc/min
4	.375
6	.615
10	.851
15	1.043

5025

Light Scattering System

Introduction

The light scattering system consists of a 5 mW He-Ne CW laser and power supply, a lens system to collect scattered light and focus it on the aperature hole, a photo-multiplier tube in a metal enclosure, a power supply for the photo multiplier, and a test section with a window and light trap on it. The lens system was an integral part of the photo-multiplier tube, and was set normal to the laser beam and water flow direction in the test section. Figure 3-13 is a schematic of the light scattering system and Figure 3-8 is a photograph. The photomultiplier (PM) tube power supply is seen in Figure 3-1(c). The laser and lens-PM tube system were mounted on adjustable platforms for easy adjustments. An aperature between laser and test section was used to intercept any diffracted light beams due to the focusing lens, which was mounted on the laser. The outside of the test section, and the inside of the light trap is painted flat-black to prevent any daylight interference

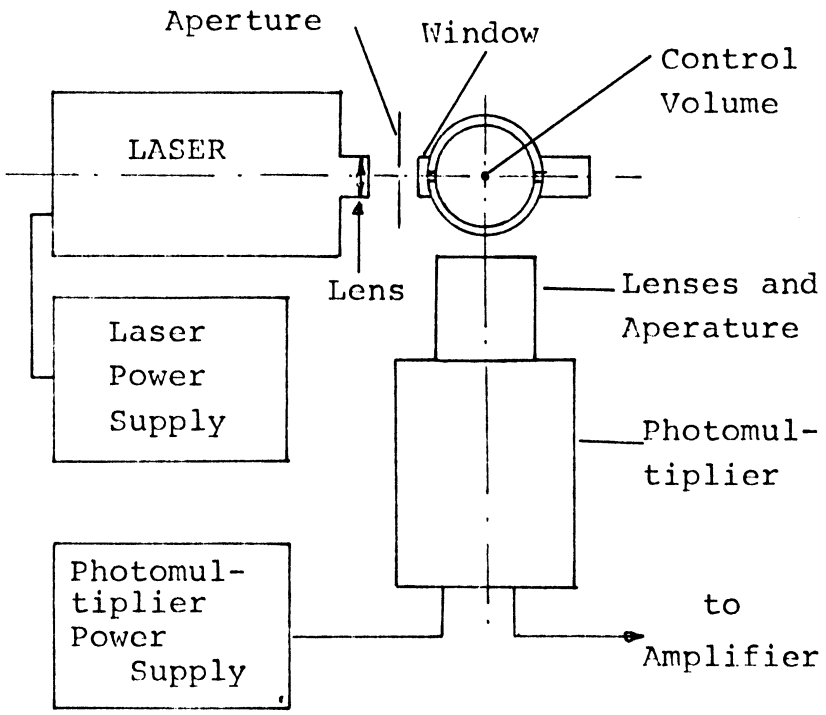

Figure 3-13 Basic layout for light scattering method.

5026

and reflection of the laser light. Figure 3-14 gives the details of the light trap, and the window on the test section.

Lenses and Photomultiplier Tube

A very short focal length (1-inch) and large lens was required to collect the scattered light effectively. A lens system was constructed using three large lenses. The number of lenses should also be limited to keep the reflected light to a minimum. About 4% of the light will be reflected from each surface [17]. Since space was also limited, three double convex lenses were used to construct the lens system. The drawing of the lens system is given in Figure 3-15. Two lenses of 54 mm diameter and 55 mm focal length (fl) were placed at each side of a larger lens having 74 mm diameter and 100 mm focal length. The whole lens system could be screwed in and out along the PM tube and aperture axis to focus the image of the laser beam at the aperture hole. All surfaces inside the metal lens enclosure were covered with velvet paper to prevent any reflections, so that no light not originating at the focal point of the lens system would be able to reach the photomultiplier. The lens-aperture assembly was integrated to the PM tube enclosure using three screws, shown on the aperature assembly in Figure 3-15.

A control volume is formed by the intersection of laser beam and aperature view. The laser beam crosses the test section at the axis. Thus any light scattered along the centerline of the test section will not be diffracted by the water-glass-air interfaces. Since the length of the control volume along the laser beam is ~ 2 mm, it can be assumed that

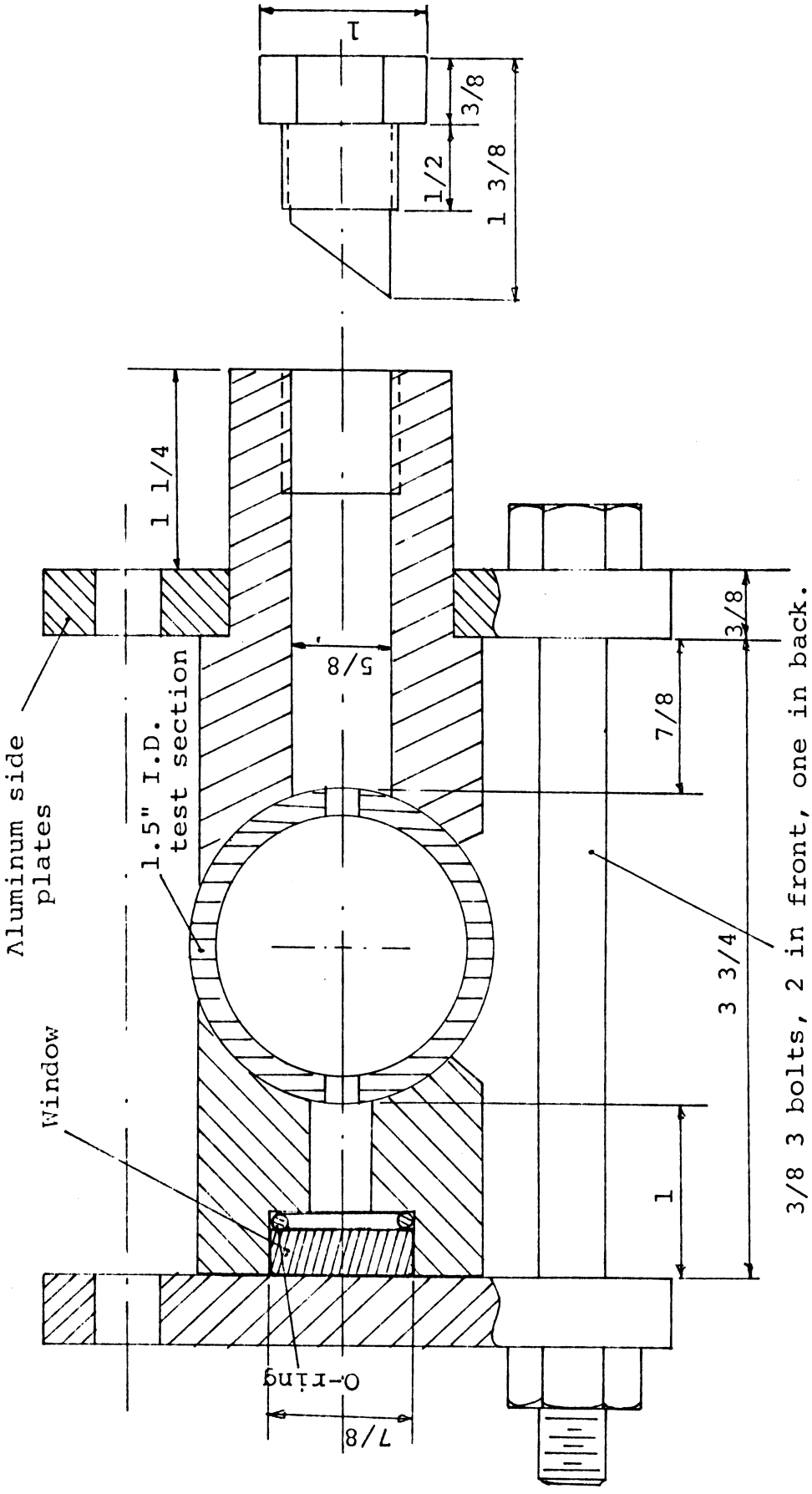

5027

Figure 3-14 Test Section Assembly.

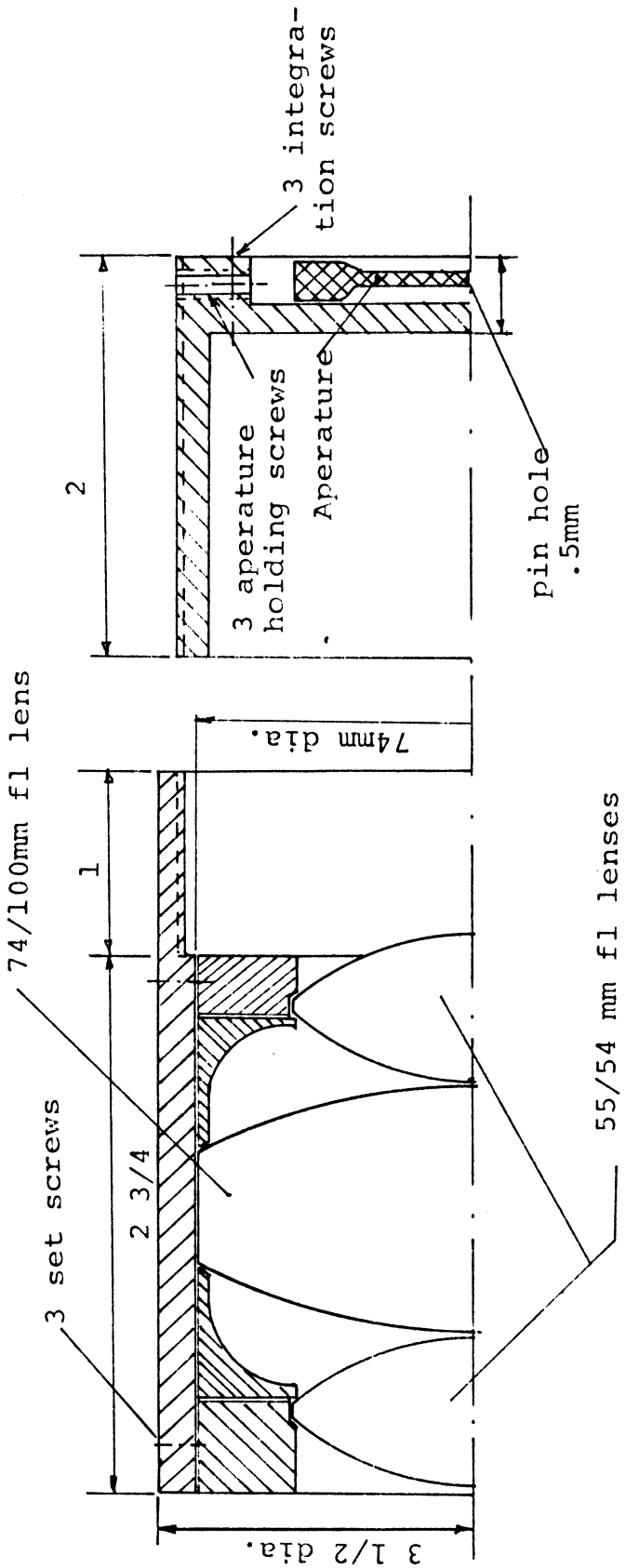

5028

Figure 3-15 Lens and Aperature Assembly

there was no diffraction at the interfaces. The lens system was designed such that all light reaching the first lens, which is scattered by a nucleus in the control volume, will be focused at the aperture hole. The distance between the axis of the first lens and the control volume is ~ 27 mm. Thus a cone with an apex angle of 90^{o} was formed by the light rays raching to the circumference of the first lens from the control volume, and by the lens.

Calibration of the Light Scattering System

There are several parameters that were not known a priori in the light scattering system. Laser beam intensity, collection efficiency of the lens system, fraction of light passing through aperatures and PM tube efficiency are some of these parameters (or variables). In order to obtain a definite relation between nucleus size and amplitude of the PM pulses, the system must be calibrated. Calibration of the system was done using bubbles whose sizes can be calculated from their velocity of ascent in static gas-saturated water, using Stoke's well-known relation. Bubbles were produced using an electrolytic bubble generator. A schematic diagram of the bubble generating system is given in Figure 3-16. A circuit diagram of the square wave generator-divider is given in Appendix E. Design of this frequency divider was required since a slow pulse generator (0.1-10 pulses/sec) was not available. System operates as a frequency counter except that one can get only one pulse out per $2^{n} \times 10^{m}$ pulses fed into the divider, where n=0-3 and m=0-3.

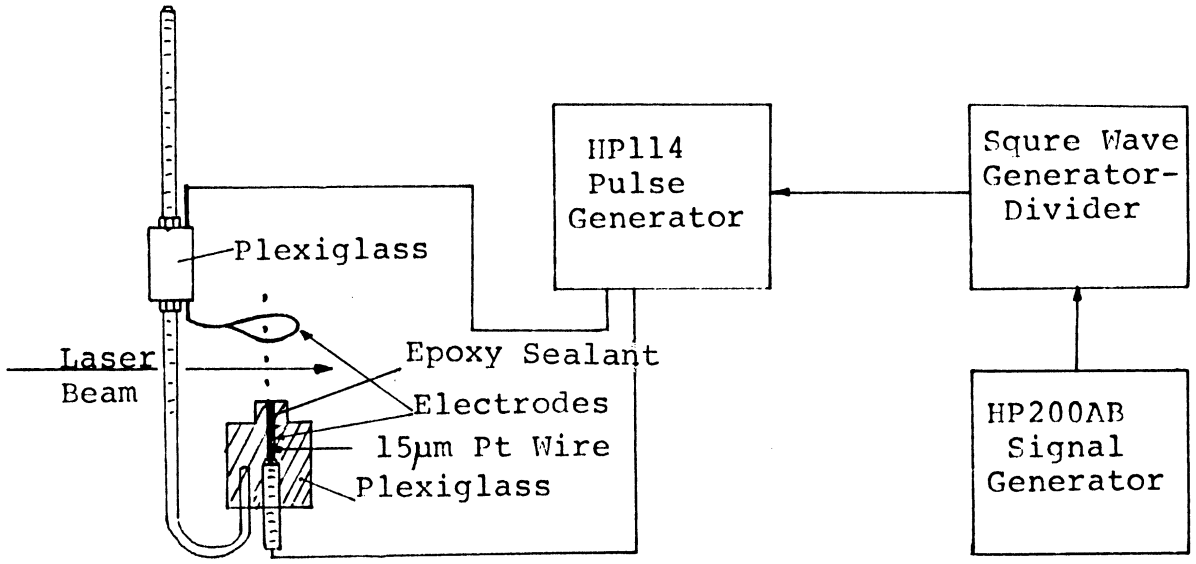

Figure 3-16 Electrolytic Bubble Generating System.

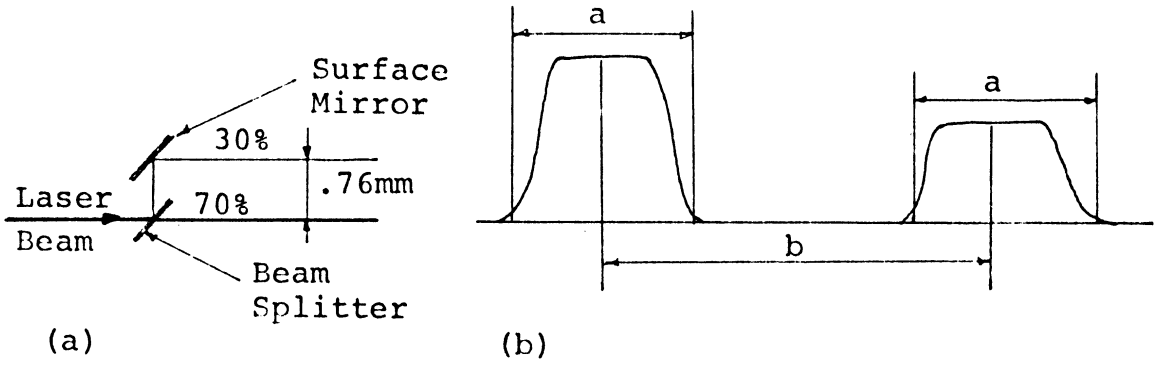

Figure 3-17 Beam Splitter (a) and Output of PM tube when a bubble crosses laser beams (b).

5031

When a pulse is applied to the electrodes, a bubble is generated by electrolysis and ascends under buoyancy. When the bubble crosses the laser beam a pulse, which is proportional to the bubble diameter, is generated at the PM tube. Bubble size can be adjusted by varying pulse amplitude and width on the electrolytic pulse generator. Minimum diameters of the bubbles so generated is ~ 20 μm. A two-component epoxy is used to embed the 15 μm diameter platinum wire in a plexiglass mount. Quality of polishing of the generating surface was very important for the generation of single bubbles of uniform size. Use of ceramic-like material instead of epoxy is recommended for future work. Keller [82] recommended a ceramic dental material.

Any change in bubble size during passage through the laser beam was neglected. The pulse height produced by these defined nuclei yielded calibration points in the scattered light intensity-nuclei size relationship. This function was then used to obtain the nucleus size from the measured pulse height.

To calculate bubble size from ascent velocity, ascent velocity must be measured. This requires knowledge of laser beam diameter, to know distance traveled by bubbles. To be able to measure laser beam diameter, two parallel laser beams were generated using a beam splitter and a first surface mirror. A schematic diagram of the system is given in Figure 3-17. The distance between two beams were adjusted to be about 1 mm. 30% of the laser beam intensity was reflected on the beam splitter surface. Thus the upper beam was weaker than the lower beam. The ratio b/a in Figure 3-17 is also the

ratio of the distance between two beams and laser beam diameter, when constant velocity of ascent is assumed. Table 3-3 gives the results of the measurements.

TABLE 3-3

LASER BEAM DIAMETER MEASUREMENTS

Bright Beam a, msec.	Weak Beam a, msec.	Distance b, msec.	Ratio b/a
1	1	4	4
0.68	0.68	2.8	4.11
0.6	0.6	2.4	4
0.625	0.625	2.5	4

5029

The physical distance between two beams was measured using a telescope and a reticle, and found to be 0.76 mm. Thus laser beam diameter is 190 ± 4 μm. After the completion of the laser beam diameter measurement, the beam splitter was removed. The time, t, which is required for a bubble to traverse the laser beam diameter was measured using a storage oscilloscope. Velocity of ascent, of course, is the ratio of laser beam diameter and time required to traverse the laser beam. Radius of the bubble was calculated using the Stoke's relation [83],

$$R = \sqrt{4.5 \frac{\nu \mu}{(\rho_\ell - \rho_g)g}}$$

where

ν = a/t

μ = viscosity of water

ρ_ℓ = density of water

ρ_g = density of gas

g = gravitational acceleration.

Figure 3-18 gives the relationship between diameter of nuclei and pulse height obtained at the output of the PM tube. The curve is obtained using the calibration points and the theoretically obtained curve which is given in Figure 2-2. Black dots on the curve are the calibration points.

Control Volume and Velocity Profile

The size of the control volume is important for three reasons:

(1) Control volume should be large enough to decrease boundary effects;

(2) It should be small enough to minimize the probability of occupation of control volume by more than one particle;

(3) Size of the control volume is necessary to be able to calculate nucleus concentration in water.

In order to be able to calculate laser beam length inside the cone defined by the aperture and lenses, the lens-PM tube system was moved upwards until pulses almost disappeared ($1/e^2$ point), and then downwards to the $1/e^2$ point where the ratio, $1/e^2$, is the ratio of

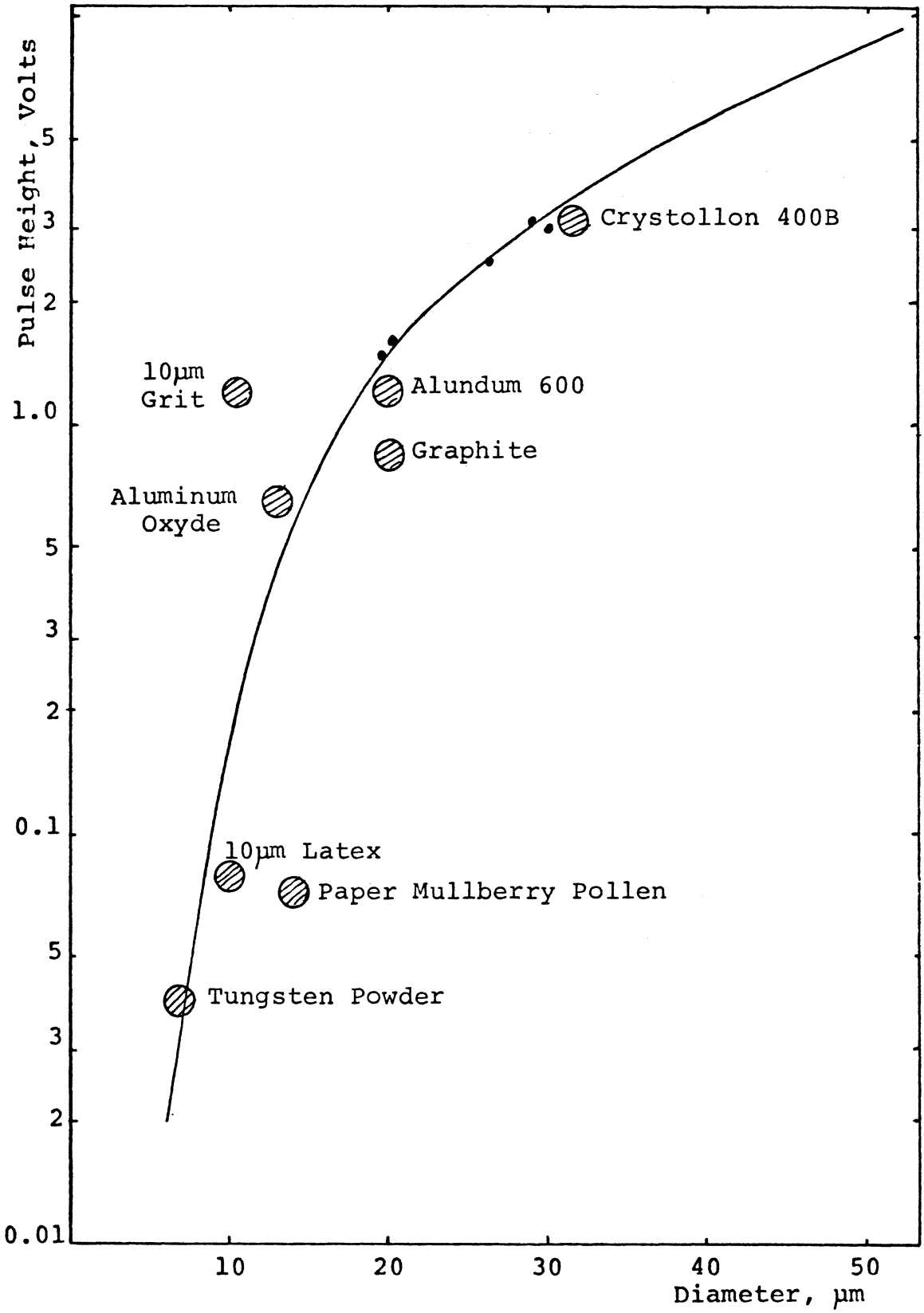

Figure 3-18 Calibratin curve for Light Scattering Method. The black dots are the calibration points with gas bubbles.

5032

intensity at the specified point to the intensity at the centerline of the laser beam. The total distance traversed by the axis of the lens system from the upper $1/e^2$ point to the lower $1/e^2$ point, is equal to the diameter of the cone, ℓ, at the point where the laser beam crosses it, plus the laser beam diameter, a (i.e., ℓ+a). Using this method, the length of the laser beam which is inside the optically defined cone was 1.8 mm. Then, the control volume is

$$V_c = \frac{\pi}{4}(.19)^2 \times 1.8 = 5.1 \times 10^{-5} \text{ cc.}$$

The coincidence effects are found [18] to be less than five percent for this size of control volume for nuclei concentrations up to 2000 nuclei/cc. Actual concentrations measured are ~ 500-4000 nuclei/cc above 6 μm diameter.

Velocity distribution is also important, since it is not uniform across the test section. Any peaking of velocity in the control volume will overestimate the nucleus content, if average velocity of water in the test section is used. Velocity distribution was measured with a 1/16-inch I. D. Pitot tube. The measured velocity distribution is shown in Figure 3-19.

The ratio of average velocity to velocity in the control volume was found to be 1.015. Thus the nucleus content will be underestimated slightly if average velocity is used.

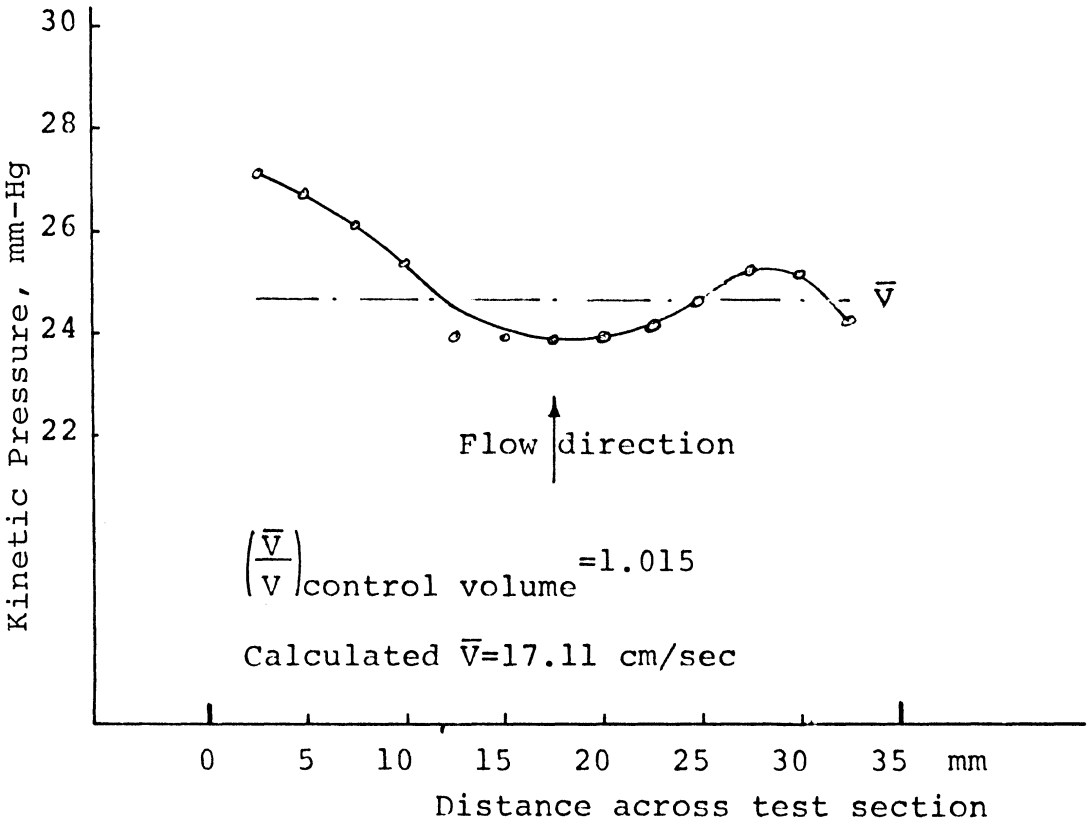

Figure 3-19 Velocity Distribution along the Laser Beam, Across the Test Section.

5033

Pulse Processing Electronics and Equipment

Multi Channel Analyzer

Multi Channel Analyzer (MCA) is an instrument to analyze incoming signals both on an amplitude and time basis. The amplitude analysis of signal pulses to determine pulse height distribution is referred to as pulse height analysis. The analysis of signals on a time basis is referred to as "Multiscaling". This analysis method is used in applications where the relative number of incoming signals as a function of time is to be determined. During a measurement, incoming signals are analyzed by the ND-110 MCA and resulting data is stored in its magnetic core "memory". Data stored in the memory can be observed in analog form, either during or after accumulation, on the cathode ray tube screen of an X-Y oscilloscope. After accumulation, stored data can be read out in digital or analog form.

There are four general types of signals which can be accepted for pulse height analysis: positive signals of 0-10 or 0-100 V, negative signals of 0-2 V, or negative low level signals such as produced by preamplifiers. Only negative signals of 0-2 V are directly applied to the Analog-to-Digital Converter (ADC) section of the MCA. Other signals go through amplifiers and pulse-shaping circuits. The requirements for input signals are very strict time-wise, and neither untreated Coulter nor PM signals satisfy them. The requirements are that the input signal must have an exponential rise, and a duration not more than three or four microseconds with a rise time of not less than one microsecond.

Slowly-varying signals can be applied to the direct-access connector ("Mössbauer"). The analyzer automatically converts such voltages to "pulses" upon the application of a coincidence pulse to the coincidence connector. The amplitude of the pulse formed is equal to the "instantaneous" voltage which existed at the time of occurrence of the coincidence pulse. Coincidence pulse widths of one or two microseconds are recommended for such applications. The input signal must be negative with a range of from zero to two volts. MCA and output equipment is seen at the left hand side of the photograph, Figure 3-11(c).

Peak Detection

Pulse widths of Coulter counter and PM pulses were about 50μ sec and 1 msec respectively. Since no adequate system existed in this laboratory to reduce pulse widths to ~ 2-3 μ sec, it was necessary to build such a system. The system requirements are that the MCA should be gated when the input pulse reaches its peak. The simplest method to generate a gate pulse when signal reaches its peak value, is to differentiate the signal and feed it through a zero-crossing detector. The differentiated signal will cross zero when the signal reaches to its maximum. However, this method was found to be inapplicable since the slightest noise in the signal caused spurious pulses when it was differentiated.

One of the two remaining methods is the "Peak Detecting Sample and Hold" circuit. A circuit diagram for this system is given in

Appendix E. The system requires a binary counter, a digital-to-analog converter, an operational amplifier, a comparator and two gates.

The method employed in building the system which was used for signal conditioning and gating for pulse processing during experiments, was a combination of a Peak Detector and the necessary electronic equipment to generate an MCA gate pulse and reset peak detector. A schematic of the system is shown in Figure 3-21.

Negative pulses from the PM tube were used to generate a trigger pulse, using a TR 104S/N trigger. Trigger pulses were fed through an external input of an HP114 pulse generator. An output pulse was generated at the trailing edge of the trigger output pulse. The output pulse from the HP114 gates the MCA just after the input pulse to the MCA reaches its peak value. The leading edge output of HP114 was fed through external input of HP222A, which is another pulse generator with delay. A delay of about 25 μ sec. was introduced and output of the pulse generator was used to reset the peak detector. The system is then ready for the next pulse when peak detector is reset.

The peak detector was built using two operational amplifiers, a diode and a transistor. The gain of the amplifier was set to 5x which was found to be optimum for proper operation of the peak detector. A circuit diagram of the peak detector is given in Figure 3-22. The signal is tracked by two amplifiers until it reaches its peak. The capaciter is charged and remains so indefinitely when the diode D1

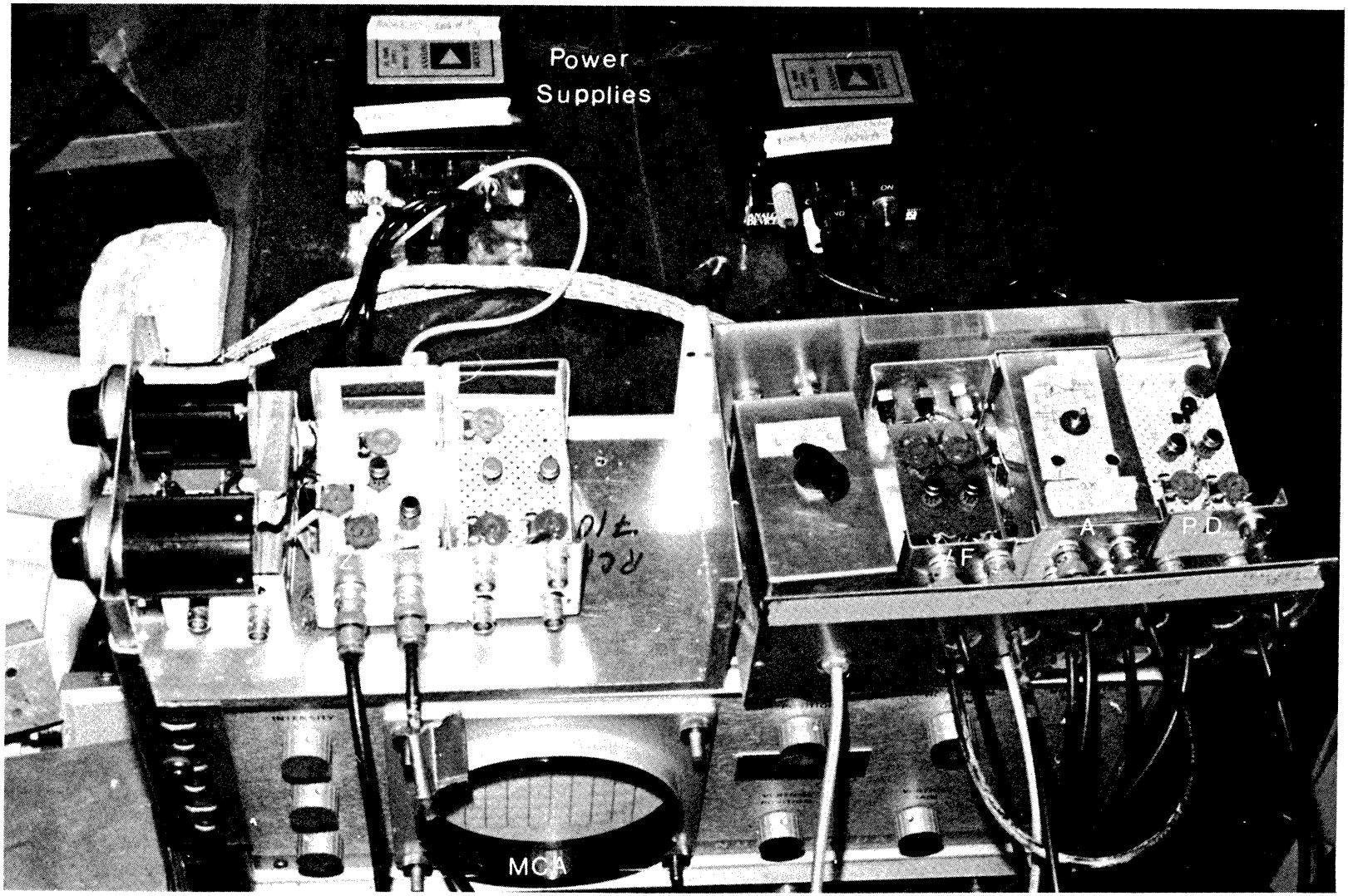

Figure 3-20 Operational Amplifiers and Power Supplies. 5034

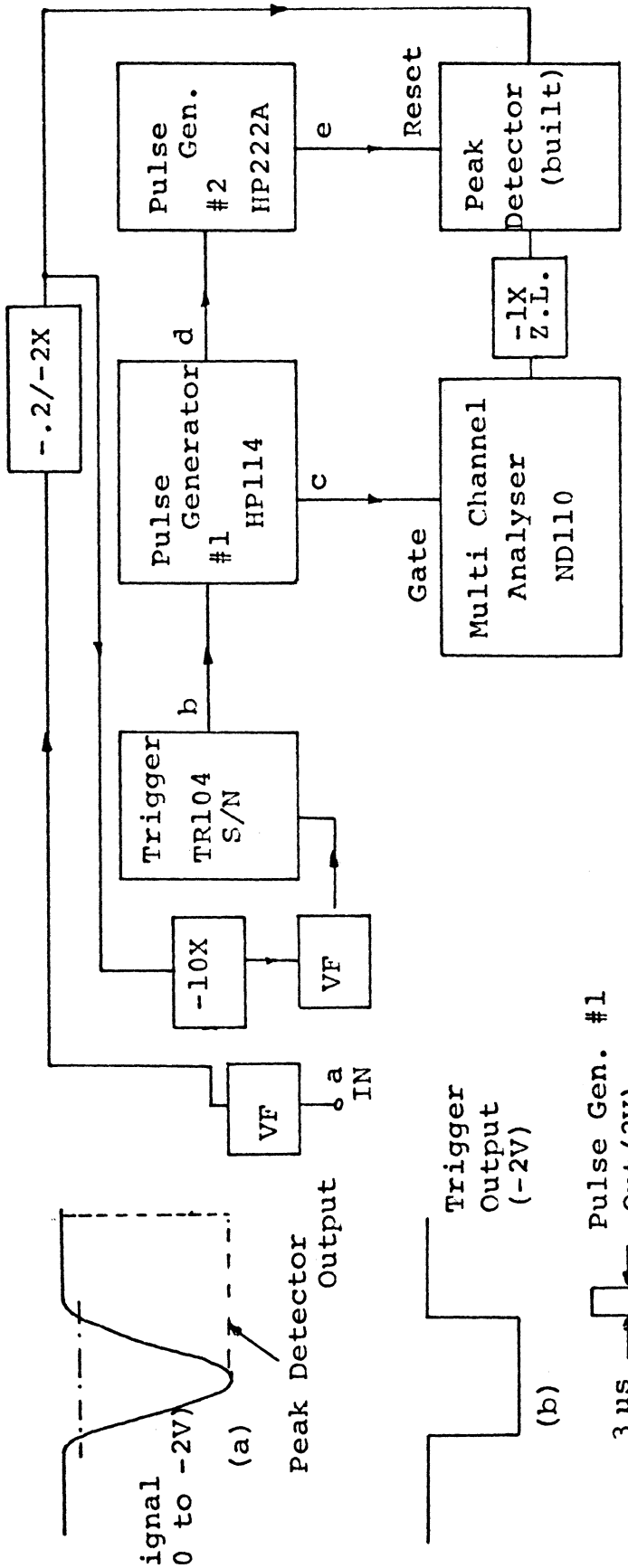

VF: Voltage Follower
Z.L.: Zero Level Adjustment

5035

Figure 3-21 Schematic Diagram of the Pulse Processing System and Wave Forms.

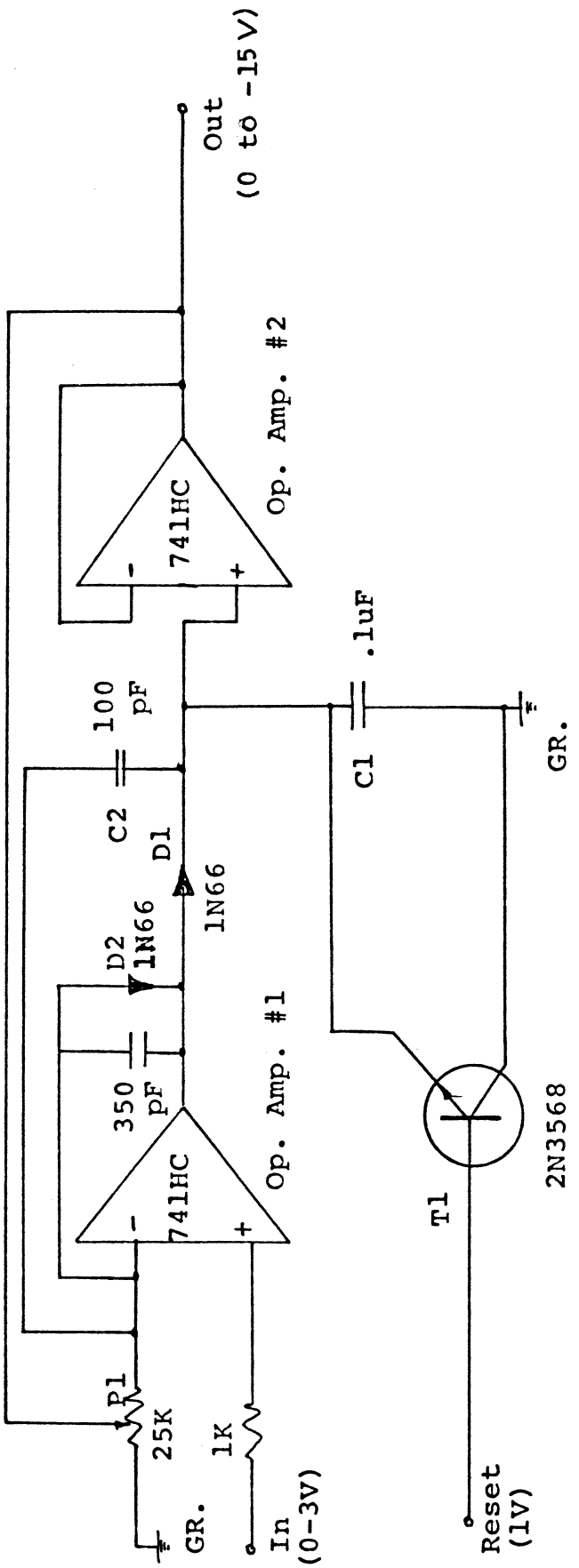

Adjust P1 such that total gain is 5X.

Figure 3-22 Circuit Diagram of the Peak Detector with Reset Circuitry.

5036

is reverse-biased. Of course in practice C_1 will discharge at a rate depending upon the input impedence of the operational amplifier (Op. Amp.) no. 2, and leakages of C_1, C_2, T_1 and D_1. It was found for this system that leakage was negligible for the durations used (about 1 msec. at most). Transistor T_1 discharges C_1 when a positive gate pulse is applied on the base of the transistor. Potentiometer P_1 was used to adjust the gain of the first Op. Amp., while Op. Amp. no. 2 had a fixed gain of unity. Capacitors C_2 and C_3 and diode D_2 were used to improve the frequency response of the peak detector.

Measurement of the Acoustic Pressure

Introduction

The vibrational motion of the tip of the horn immersed in the test liquid produces sound waves which are transmitted through it. As the power to the acoustic horn is increased, the amplitude of the pressure waves increases. If the negative pulse of these sound waves reduces the pressure in the test liquid below a certain value, cavitation may occur therein. The amplitude of these pressure waves can be measured either directly or indirectly. Direct methods are, of course, more reliable, but have some disadvantages. In a high temperature fluid like liquid sodium, the disadvantage would be the material limitations for the pressure probe. Most pressure probes for dynamic pressure measurements utilize piezoelectric crystals which are temperature-limited. PZT-5A has the highest Curie point (365°C) among all PZT materials, and maximum recommended operation

temperature is 250°C. Lead Metaniobate ($PB(NbO_3)_2$), manufactured by General Electric Co., has a maximum Curie point of 550°C. and ~ 450° C. operation temperature.

If a direct measurement of pressure must be made, the pressure probe must be sufficiently close to the horn. Interference to the pressure field will occur if the pressure probe is not small enough. Surface irregularities may also cause initiation of cavitation on the probe which then may be damaged. Thus the pressure probe must be located far enough from the surface of the horn tip to avoid these difficulties. A serious disadvantage that cannot be overcome, is that of distortion and even complete loss of signal, when cavitation starts. Distortion will cause error to the RMS value of the signal, which is required to evaluate the pressure amplitude. It was because of the non-availability of very small pressure probes, and the distortion and loss of the signal at the initiation of cavitation, that direct measurements of the pressure was abandoned.

A theoretical expression describing the pressure field, and experimental verification of this theoretical expression using water, was made by Nystrom in this laboratory [27]. The expression is a function of geometry, various fluid parameters, and parameters describing the motion of the tip of the horn. The expression for a rigid wall container with baffled geometry approximation is

$$P(\bar{z},\bar{r}) = \bar{\ell}\bar{k}\rho_o A\omega c\left[\frac{\lambda^2 \cos[\bar{\ell}\bar{k}(1-\bar{z})]}{\bar{\ell}\bar{k}\sin(\bar{\ell}\bar{k})}\right.$$

$$\left. + 2\lambda \sum_{j=1}^{\infty} \frac{\cos[\bar{K}_j(1-\bar{z})]\, J_o(\alpha_j \bar{r}) J_1(\alpha_j \lambda)}{\alpha_j \bar{H}_j J_o^2(\alpha_j)}\right] \qquad (3\text{-}1)$$

where

$\bar{\ell} = \ell/a$ $\qquad$ $\bar{w} = w/c$

$\bar{z} = z/\ell$ $\qquad$ $\lambda = b/a$

$\bar{r} = r/a$ $\qquad$ $\bar{K}_j = \bar{\ell}(\bar{k}^2 - \alpha_j^2)^{1/2}$

$\bar{k} = a\bar{w}$ $\qquad$ $\alpha_j = j^{th}$ zero of J_1

$\bar{H}_j = \bar{K}_j \sin \bar{K}_j$

ℓ = length of the vessel

a = radius of the vessel

ω = frequency of horn

c = sound speed in medium.

The above expression would more accurately predict the pressure field inside the cavitation vessel at conditions far removed from any resonant condition or mode, since at resonant conditions, equation (3-1) predicts infinite pressures which are not realistic. The number of resonance frequency modes encountered increases as the length of the vessel increases [27].

For the system which was used in these investigations, the length of the vessel was 16 inches and the diameter 1.5 inches. Solution of equation (3-1) has predicted pressures at least 10x measured.

Thus it was concluded that, at least one, or perhaps several, resonance modes were playing an important role. Therefore, this method was not used. The method actually employed is discussed later.

The amplitude of the horn tip which was necessary for the solution of equation (3-1) was measured using two independent methods: an 800x microscope, and a KD-38 Fotonic Sensor. Figure 3-23 is a plot of counter balance crystal output versus peak to peak horn-tip amplitude.

Calibration of Counter Balance Crystal

The indirect method of pressure amplitude measurement selected here uses an accelerometer, consisting of a single crystal, bonded to the top of the acoustic horn assembly (Figure 3-5). If a sinusoidal voltage signal is applied to the driving PZT piezoelectric crystals of the transducer assembly, the resulting displacements transmitted through the transducer assembly will vary sinusoidaly. If we select an arbitrary reference at any point in the transducer assembly, and if we let y be the vibrational displacement about the reference point, then

$$y = y_o \sin \omega t \qquad (3-2)$$

where

y_o = maximum displacement

ω = angular frequency of vibration

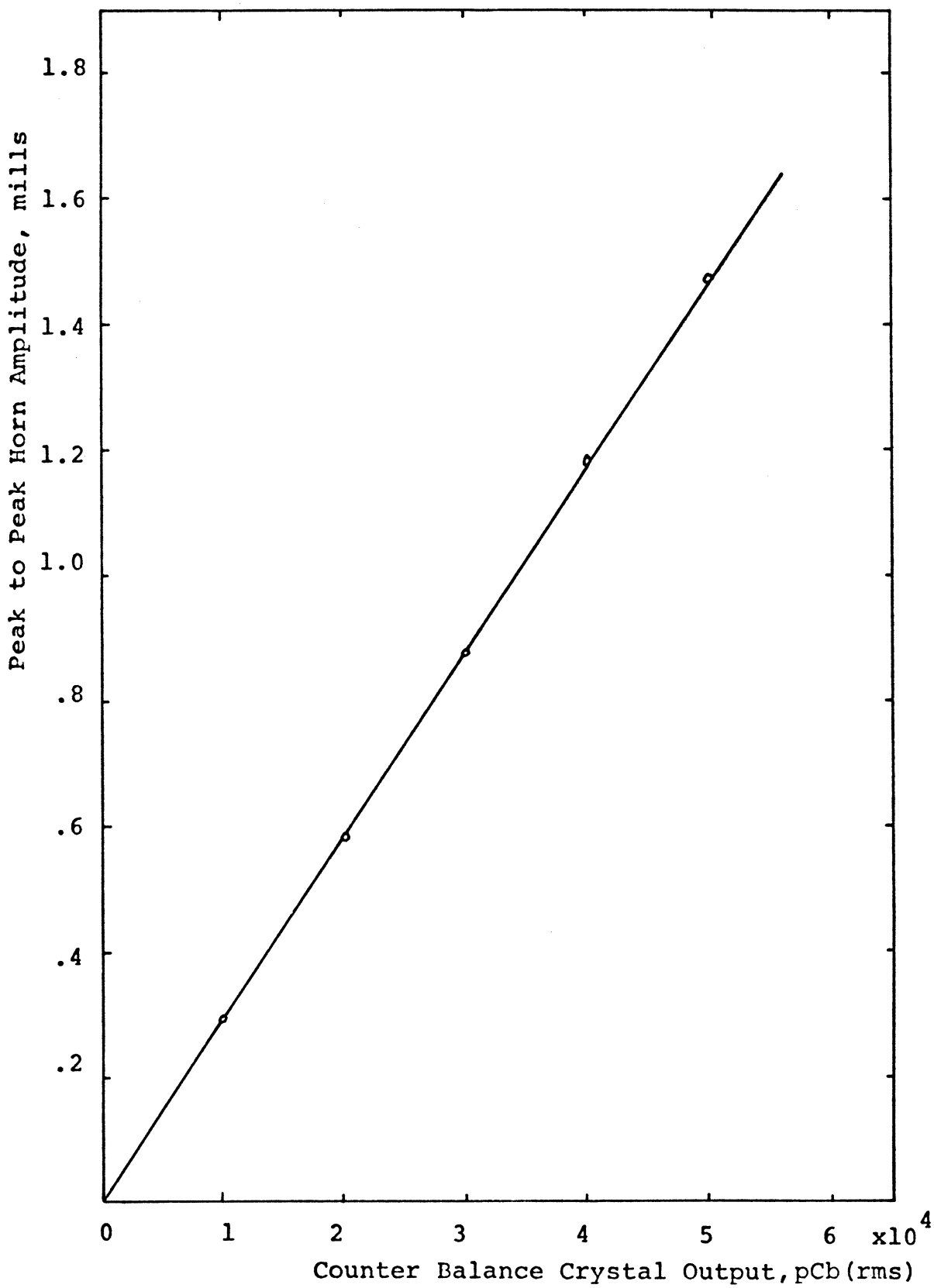

Figure 3-23 Horn Amplitude Versus Counter Balance Crystal Output.

5037

The acceleration, a, at the reference point can be obtained by differentiating equation (3-2) twice

$$a = \frac{d^2y}{dt^2} = -\omega^2 y \qquad (3-3)$$

Thus acceleration at any point in the transducer assembly is proportional to the particle displacement at that point.

A PZT-4 piezoelectric crystal, identical to the crystals used to drive the transducer assembly, was attached to the top surface of the counter weight. A contact cement known as Permabond 102 was used to attach the crystal to the counter weight. An electrical connector was also cemented to the top surface of the crystal using silver paint and Permabond 102. Thus voltage produced by the counter weight crystal (CWC) can be monitored using a charge amplifier and VTVM or oscilloscope.

In order to establish the relationship between the CWC charge output, and the pressure in the test water, acoustic pressure had to be measured. Measurement of the acoustic pressure was accomplished using Kistler pressure transducer 603A. Transducer was placed near the surface of the horn, and its output was monitored using a Kistler 566 charge amplifier. The same amplifier was also used to measure charge on the CWC. The calibration curve, thus obtained, is shown in Figure 3-24. Liquid pressure on the surface of the horn was obtained by extrapolating the data points to zero horn distance, on the pressure distribution curve (Figure 3-25). When obtaining the data for Figure 3-24, a pressure of about 70 psig was maintained in

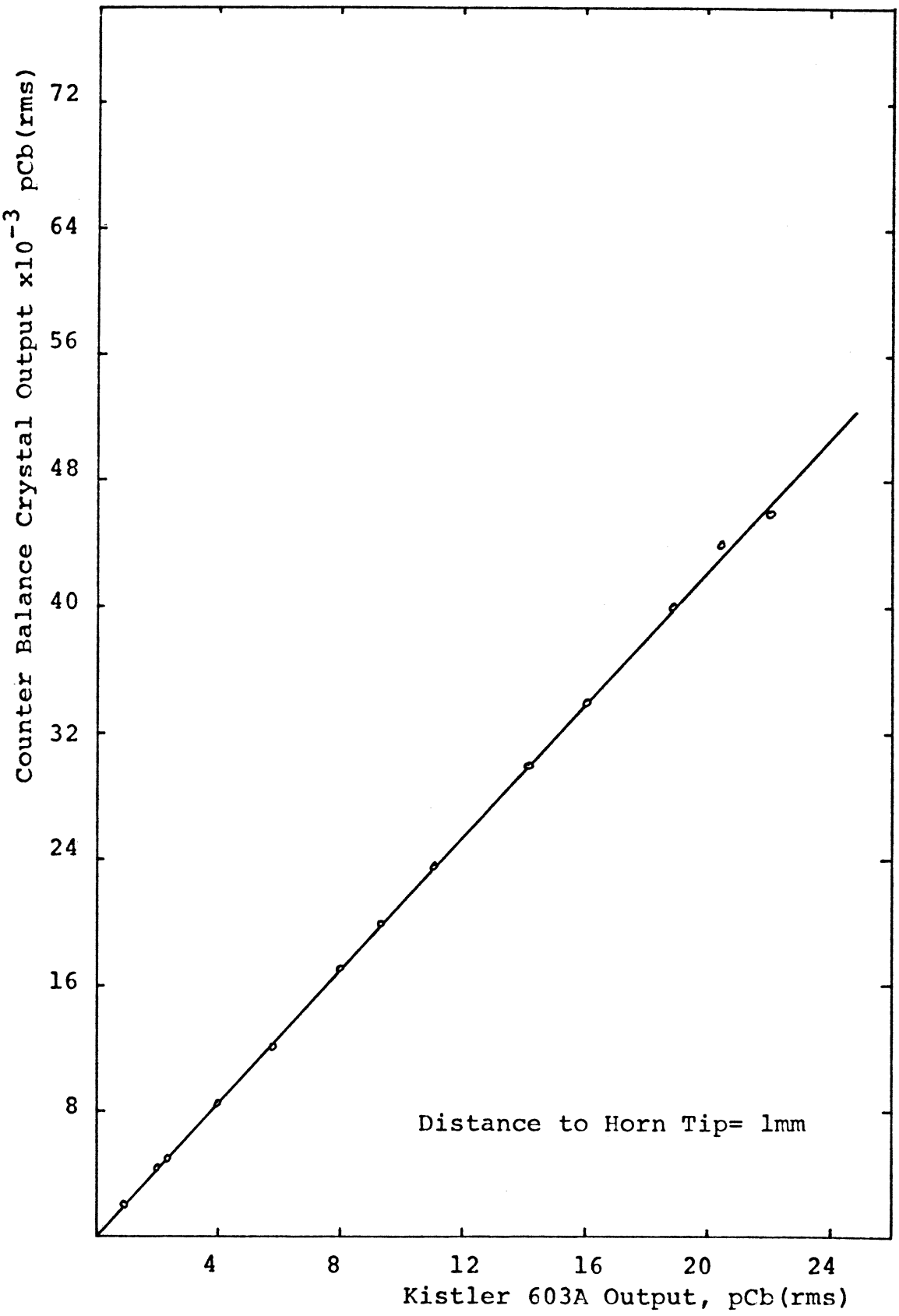

Figure 3-24 Calibration Curve for Counter Balance Crystal with Kistler 603A Pressure Transducer.

5038

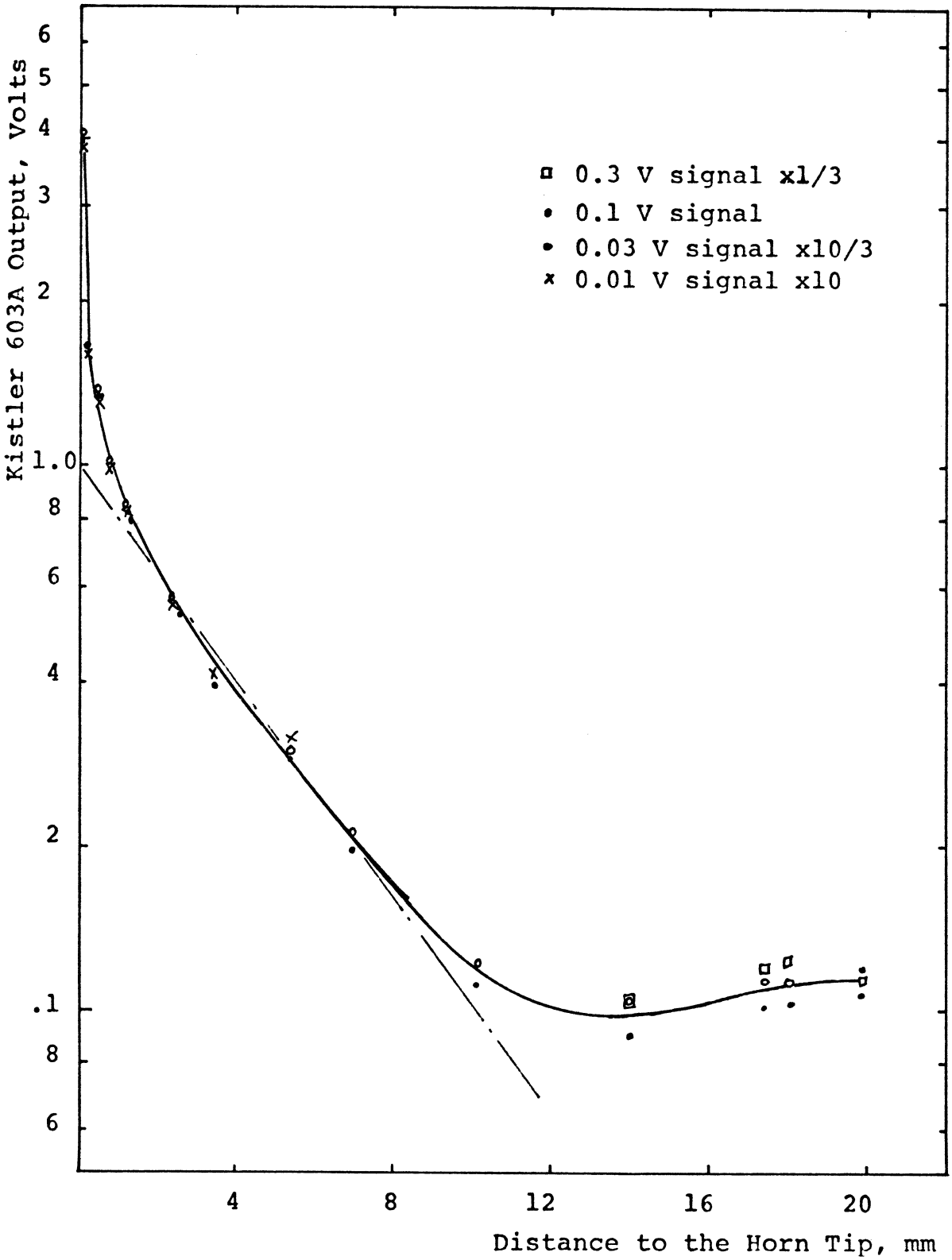

Figure 3-25 Pressure Intensity as a Function of Distance to the Horn Tip Along the Test Section.

5039

the system to prevent cavitation. Figure 3-25 was obtained for different values of pressure amplitudes, but normalized to the results obtained for 0.1 V signal generator voltage. As it is seen, different amplitudes of vibration did not effect the pressure distribution along the axis of the vessel.

Sensitivity of the Kistler pressure transducer, according to the manufacturer, is 0.35 pCb/psi. The calibration curve, Kistler pressure transducer versus pressure, for the transducer is given in Figure 3-26. Thus measured sensitivity of 0.335 pCb/psi is only about five percent less than the factory calibration. A decrease in sensitivity of piezoelectric crystals is expected due to aging. Figure 3-27, final calibration curve, is obtained using the data presented on Figures 3-24, 3-25 and 3-26. This calibration curve, thus, relates the counter weight weight crystal output to the actual pressure very close to the horn tip.

Typical waveforms observed during calibration is given in Figure 3-28.

Detection of Cavitation Inception

A survey of methods for the determination of cavitation inception for water tunnel tests is given by Acosta et al. [86]. Historically, the existence of cavitation was first observed with the unaided eye under natural illumination. Erratic and often unreproducible results have led to such visual observations being carried out under stroboscopic illumination. Methods developed for the detection of the inception of acoustic cavitation can generally be classified in three groups:

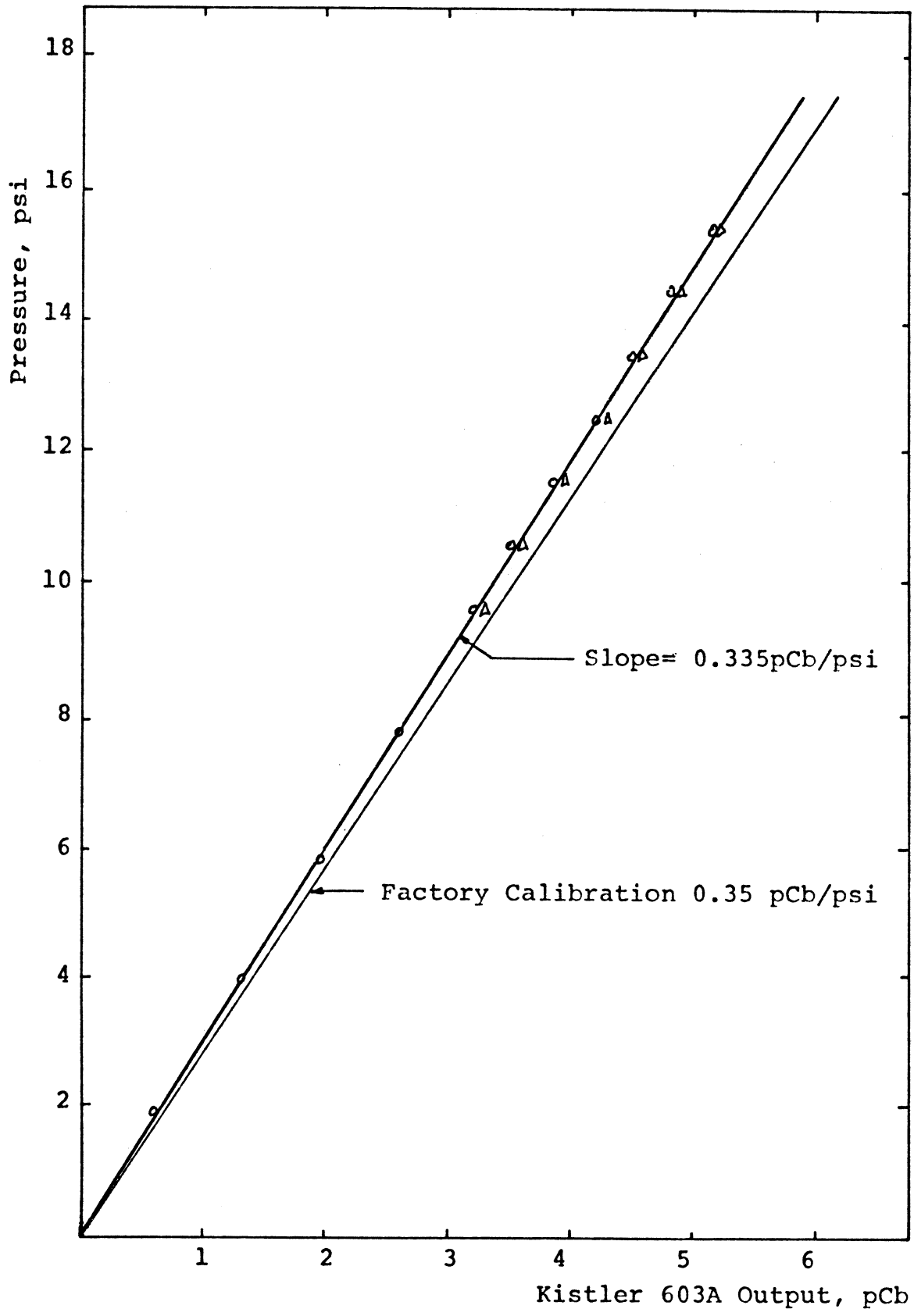

Figure 3-26 Calibration Curve for Kistler 603A Pressure Transducer.

5040

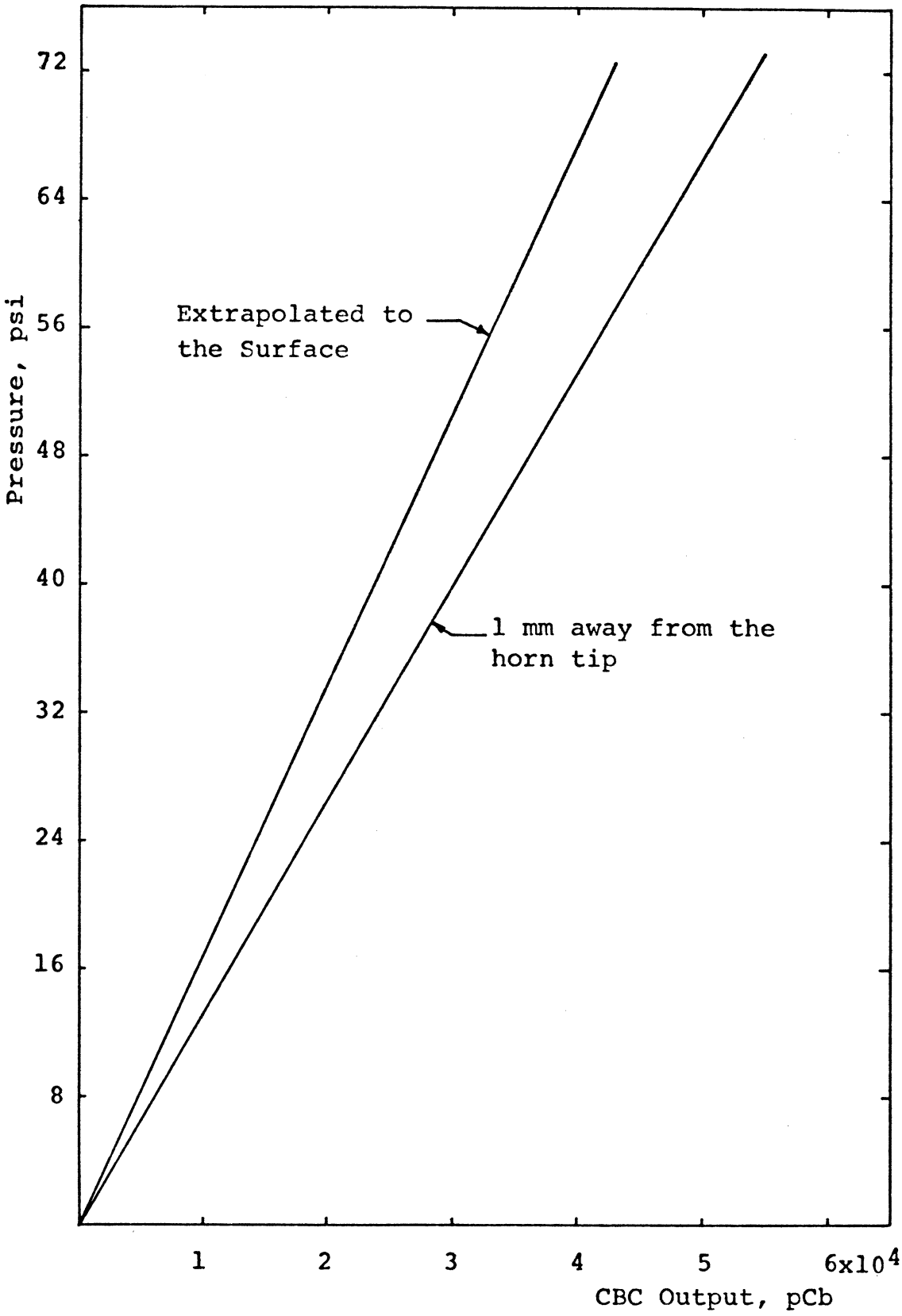

Figure 3-27 Pressure in the Water as a Function of Counter Balance Crystal Output.

5041

(1) visual observation, (2) acoustic detection, and (3) light-beam interruption.* Whichever the method of inception determination, the question of inception definition has not yet been standardized.

Cavitation formed in slightly degassed water occurs as small, almost explosive ruptures. Each individual cavity is very short-lived, disappearing completely in most cases in a time of about half a cycle of the acoustic frequency. Some "resonate" and persist for numerous cycles, sometimes long enough for "rectified diffusion" to be important. Each occurrence of a rupture and subsequent bubble collapse is accompanied by a loud snap, that could be heard in a quiet room.

Acoustic cavitation inception pressure could be defined as the peak sound pressure at which a certain number of cavitation events are detected per second. Cavitation inception exhibits a hysterisis effect [87]. For example, relatively large pressure amplitudes may be required to start cavitation. If one then reduces the amplitude, cavitation may persist until the amplitude has been reduced ~ 20-30 %. The pressure amplitude at which cavitation stops is called "desinent cavitation threshold". Conolly [88] defined the inception cavitation threshold as the desinent cavitation threshold. A uniformity among other investigators, however, exists, and they [24, 25, 26] define

*The light signal from sonoluminescence has also been used [101], but this is not as yet a widely accepted method.

cavitation threshold as the pressure amplitude at which cavitation starts. Thus, in this investigation, cavitation inception threshold pressure will be defined as the pressure amplitude corresponding to the inception of cavitation.

When visual detection of cavitation inception is used, usually, a dark field illumination is necessary. Illumination is done using high intensity lamps to be able to detect the smallest bubble observable by the unaided eye. The room should be dark, and observations should be made against a dark background.

Acoustic detection of inception may also be used. Noise is generated due to cavitation bubble collapse, and can be seen in hydrophone output as a signal imposed on the pressure signal. Even individual bubble collapse may be observable by this method.

Light beam interruption to signal cavitation inception has been employed successfully by Keller [17] and others previously ([16], e.g.) The method used in this investigation for the detection of cavitation inception was functionally as that of Keller. A He-Ne continuous wave laser with an output of about 1 mw was used as light source. Figure 3-30 is a schematic of the system.

It was observed that cavitation usually starts at the center of the horn tip. Vaporous cavitation spread so quickly that about 2/3 of the horn surface was covered with cavitation bubbles almost instantaneously with only slight additional increase of horn amplitude. Thus, exact position of the laser beam along the horn surface was not very important. When the gas content of the water was saturated or oversaturated,

cavitation occurred at different intensities, depending on the pressure amplitude. Thus it was necessary to define an intensity of cavitation for inception.

Measurement of Total Air Content

Even when many bubbles are present, typically most of the gas contained in the water is dissolved gas. The total air content of the water sample was measured with a modified commercial Van-Slyke apparatus (Figure 3-29). To measure the gas content of the test water, a 10cc sample must be injected into the Van Slyke. The sample is then agitated while under vacuum, until all gas is mechanically removed. Five minutes of agitation was found to be sufficient to remove all the gas in the sample. The pressure of the gas was then measured when compressed to 1 cc. Its volume at normal temperature and pressure is calculated assuming it to be a perfect gas.

The gas content of water is reported in terms of gas at STP per unit volume of water. Air concentration is given by

$$C_o = \frac{10\ \Delta P \times 273}{760(273 + T)} \text{ volume \%}$$

where ΔP is the pressure difference in mm-Hg between the 1 cc compressed gas, and the expanded gas after all gas removed from the agitation flask. T is the temperature of water in degrees - C.

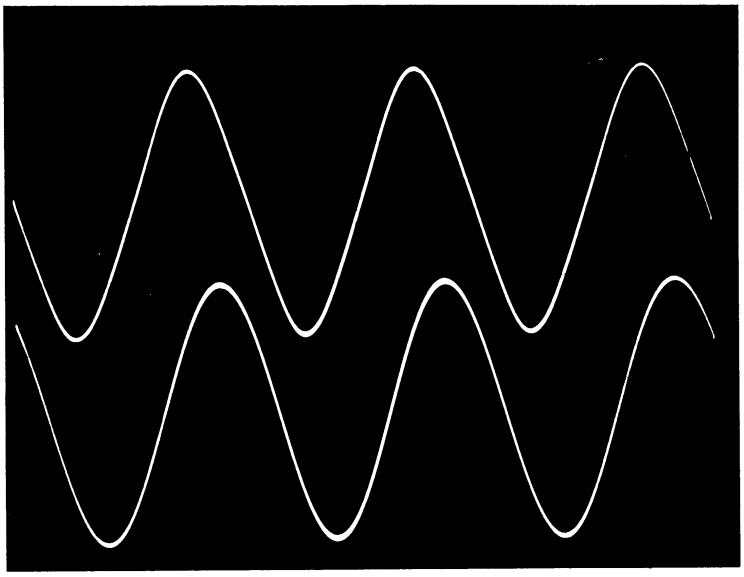

Figure 3-28 Typical Waveforms Observed. Upper, Counter Balance Crystal Output, 1000 pCb/cm; Lower, Kistler 603A Output, 0.5 pCb/cm.

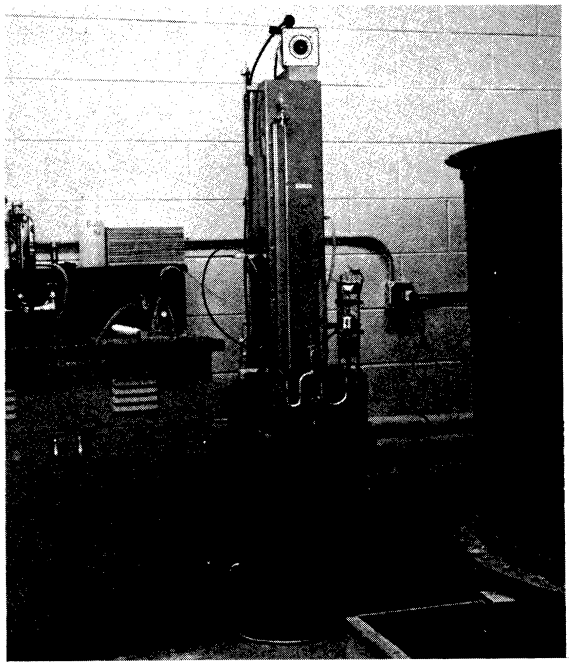

Figure 3-29 A Photograph of Van Slyke Gas Apparatus.

Fast Neutron Sources

Flux and Energy Spectrum

Different types of neutron sources have been used for the study of neutron irradiation effects upon bubble nucleation. Most of the work so far done has been either with neutron generators or (α, n) sources. A Picker-Dresser neutron generator was used by Finch [78] producing 14 Mev neutrons at a rate of 10^8 neutrons/sec. For the radiation sources the target atom has usually been Be^9, the alpha emiters have been Ra [76], Po^{210} [77], Am^{241} [79] and Pu^{239} [14, 79, 89]. The main disadvantage of a Ra source is its high γ-ray background, about 6500 gammas per neutron. The neutron energy spectra of such sources are variable even among these nominally the same, and they are known only approximately. The energy varies from zero to a maximum of 13.1, 10.9, 11.4 and 10.7 Mev for Ra, Po, Am and Pu, respectively. The average energy is about 4.5 Mev.

The data would be more easily interpreted if more nearly monoenergetic neutrons produced by particle accelerators were used [79].

Cosmic ray neutrons with energy equal to or higher than 10 Mev can produce oxygen recoil nuclei higher than 2.5 Mev. Flux density of cosmic ray neutrons having energies 10 Mev or above is $2\text{-}12 \times 10^{-4}$ neutrons/cm^2-sec. [76, 79] at sea level which is about 7% of the total cosmic ray neutron radiation.

The neutron source in the present investigation was a Pu^{239}-Be neutron source. The total strength of the source was 1.2×10^6 n/sec. An

approximate energy spectrum is given in Figure 3-31 [90]. Neutron energies of the source vary from zero to 10 Mev. The average energy of the source was about 4.5 Mev [79].

Safety

The National Committee on Radiation Protection (NCRP) has formulated basic rules and recommendations concerning exposure to ionizing radiation [91]. The maximum permissible dose (MPD) to the most critical organs, accumulated to any age, shall not exceed five rems multiplied by the number of years beyond age 18, and the dose in any 13 consecutive weeks shall not exceed three rems. Thus the maximum allowable accumulated MPD = (N-18) x 5 rems, where N is the age in years, and is greater than 18.

Assuming that three rems is accumulated in 13 weeks, average dose rate is 5.8 m rem/hr. Since 1 neutron/cm^2-sec. of 10 Mev neutron gives a dose rate of 0.21 m rem/hr, and Pu-Be source has a strength of 1.2×10^6 neutrons/sec. the safe distance, ℓ, assuming a spherical isotropic source, would be

$$\frac{1.2 \times 10^6}{4\pi \ell^2} = \frac{5.8}{.21} \Longrightarrow \quad \ell = 59.5 \text{ cm.}$$

Assumption of spherical symmetry may be very approximate, since cylindrical source containers (1" dia., 2" long) have thicker top and bottom compared to wall thickness.

Measurements showed that one meter distance to the source guaranteed only about 2.5 m rem/hr. exposure. Thus when handling

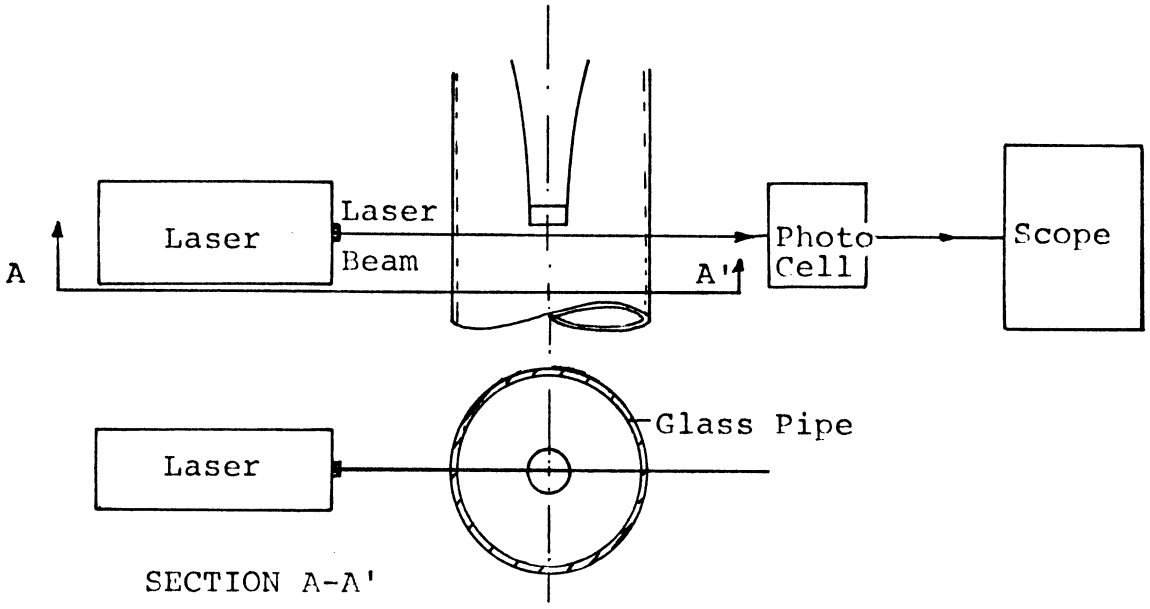

Figure 3-30 Light Beam Interruption Method for the Detection of Cavitation Inception.

5044

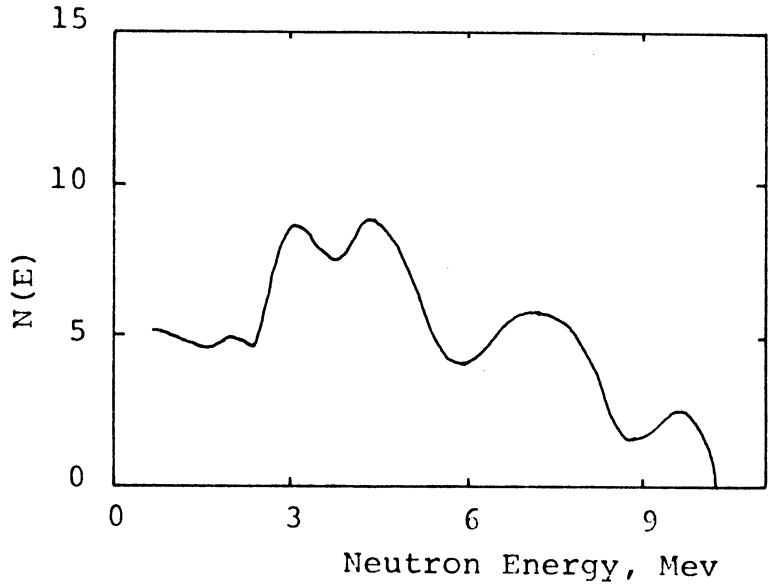

Figure 3-31 Neutron Energy Spectrum for Pu-Be Fast Neutron Source.

5045

the source, one meter was considered to be the minimum safe distance. Figure 3-32 gives safe distance as a function of dose rate for 10-30 Mev fast neutrons.

Since Plutonium is very poisonous material, handling of the source should be done very carefully so as not to drop and possibly crack it. For occupational exposure, maximum concentrations of 2×10^{-12} μC_i/cc for bone and 4×10^{-11} μC_i/cc for lung is allowed in the air [91].

Magnetic Field

The electromagnetic system used consists of a six-inch electromagnet and a power supply (Figure 3-1).

The electromagnet consists of two coils placed on a yoke to produce a magnetic field when current is supplied (Figure E-3). The magnet cooling system requires a water flow of ~ 1 GPM to insure proper cooling for continuous duty at high currents. Rated current is 1.45 amps/winding-section. A regulated portable magnetic power supply, rated at 1.4A and 820 V, is used as a current source for the electromagnet.

An approximate gap field as a function of magnetic current and gap width is shown in Figure E-4. The measured magnetic field was 5.7 K Gauss at 1.4 amperes as indicated on the magnet power supply current meter for a gap of 2.14 inches as used for the experiments.

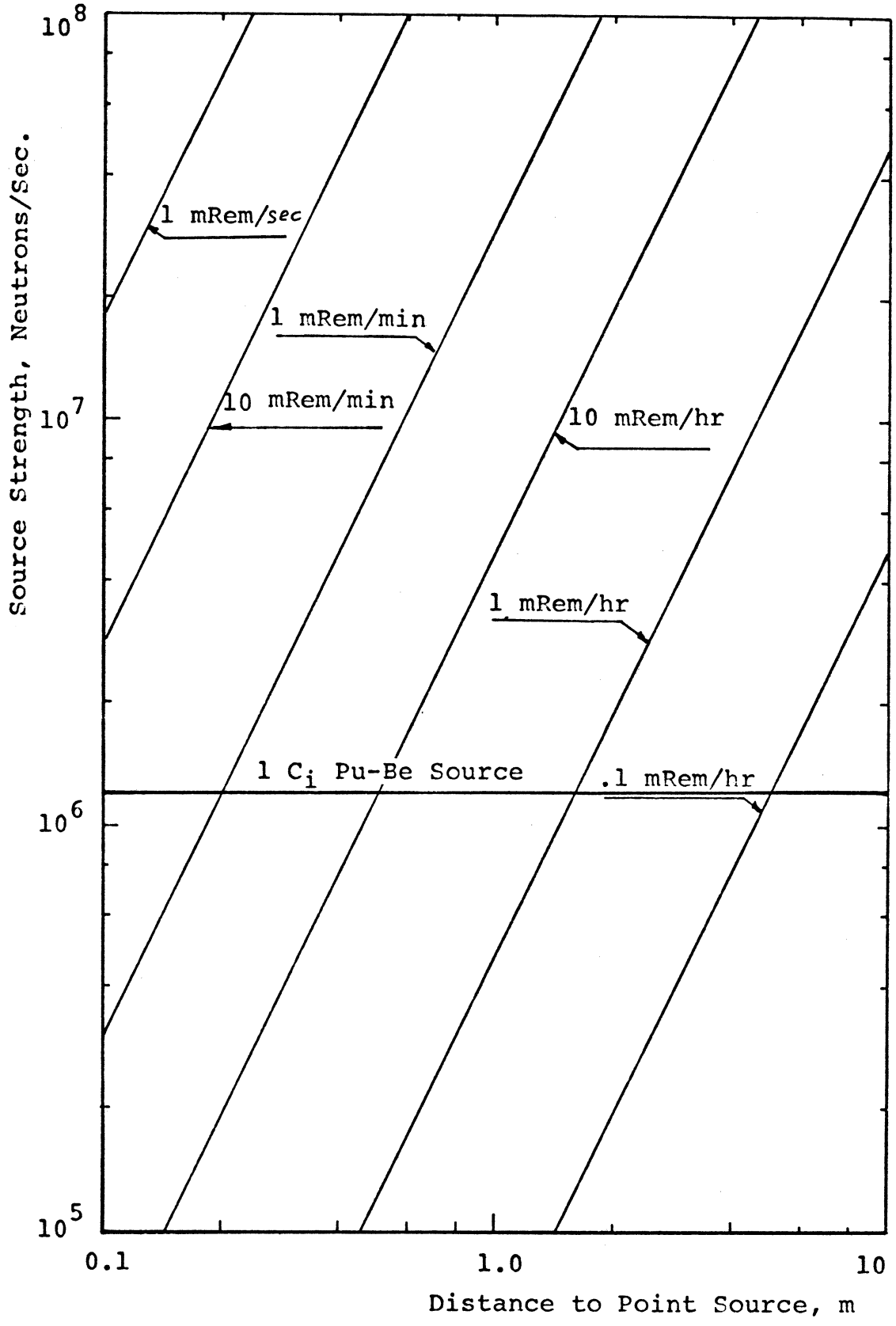

Figure 3-32 Radiation Dose Rates Due to an Isotropic Point Source of Fast (10-30 Mev) Neutrons.

5045b

CHAPTER IV

EXPERIMENTAL INVESTIGATIONS AND RESULTS

Comparative Measurements

The Coulter counter and light scattering methods are evaluted for the measurement of nucleus spectra in water. Neither methods can distinguish between gas bubbles and suspended solid particles. Calibration of the Coulter counter used spherical latex particles. For the light scattering method small (spherical) bubbles were used for calibration. Thus both methods were calibrated using spherical nuclei. For purposes of interpretation, the nuclei present in water must then also be considered as spheres, even though it is realized that the nuclei can survive only as a result of contamination of the bubbles with solid particles.

Each system was calibrated with one type of nuclei only. No consideration was given to the scattering behavior of suspended particles of different refractive indices or shape, or to the varying electrical resistivity of the different nuclei.

To determine whether these techniques would give satisfactory information of nucleus spectra in water, a series of tests were carried out. Water with different qualities concerning nucleus content were tested with both methods, and the results were compared. To see the response of the Coulter counter to the electrical conductivity of the test sample (electrolyte), different concentrations of salt in the water samples were used. Table 4-1 gives the properties of the water

samples used.

Figure 4-1 gives the spectrum plotted as pulse height for the same sample of water using two different nucleus spectrum measuring methods. Figure 4-2 gives the spectrum for tap water with different salt concentrations, as compared to the spectrum obtained by the light scattering method.

Figure 4-3 shows a typical Coulter spectrum for conducting particles, namely graphite. Obviously not all particles in the water sample are conducting. Thus both positive and negative pulses are obtained.

The results of the comparative measurements are summarized in Table 4-2. As it will be noted, further addition of salt (i.e. $\geq 0.2\%$ by mass) did not increase the measured percentage of nuclei detected by the optical method appreciably, which reaches a level of about 60% for $\sim 0.1\%$ salt by mass. Of course the absolute accuracy of the optical method also is not known so this degree of agreement is encouraging.

Nucleus Spectrum Measurements Using Light Scattering Method

Selection of Light Scattering Method

Dependency of pulse height or nuclei spectrum on electrolyte conductivity is a serious difficulty for the Coulter counter. As explained in the last section measurements for tap water showed that the total number of nuclei measured in the range 5-8 μm diameter with this instrument was only 20% of the number of nuclei measured by the light scattering method. While the instruments can be made to agree relatively closely by salt addition to the Coulter sample, this could be a

TABLE 4-1

PROPERTIES OF WATER SAMPLES

USED IN THE EXPERIMENTS

Sample	NaCl % salt (mass)	% gas (volume)	Particles added	Size of particles (dia) μm
Tap Water	0	2.16	-	-
	0.05			
	0.1			
	0.2			
Filtered and Degassed	0	0.54	graphite	20 and less

5046

TABLE 4-2

RESULTS OF THE COMPARATIVE MEASUREMENTS

% Salt in Tap Water	% of Laser 5-8 μm	in the Range 6.5 - 8 μm
0	19.85	7.89
0.05	36.58	25.36
0.1*	61.6	45.12
0.2	60.38	48.74

*Different water sample

5047

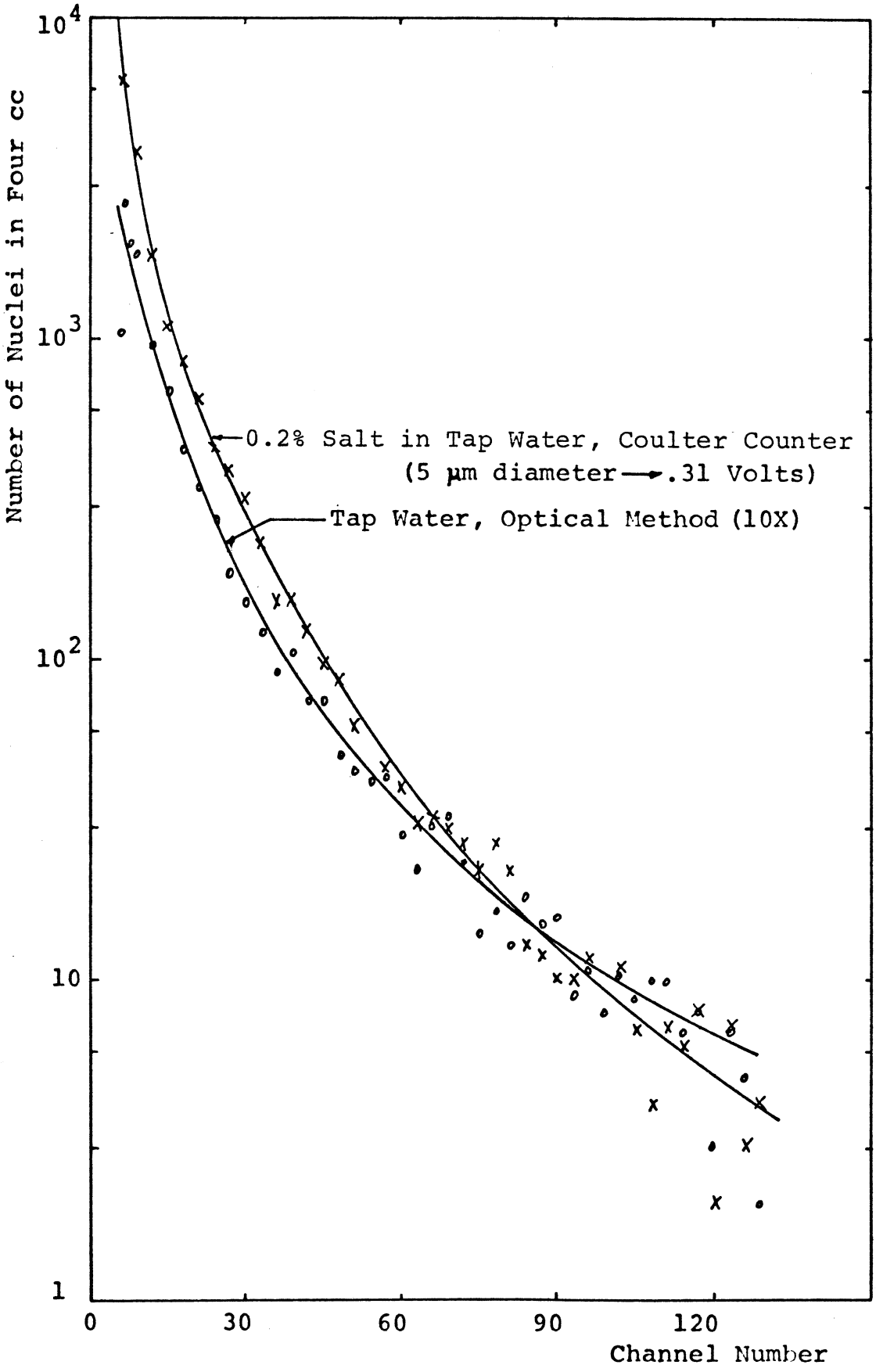

Figure 4-1 Nucleus Spectrum as Stored in MCA.

5048

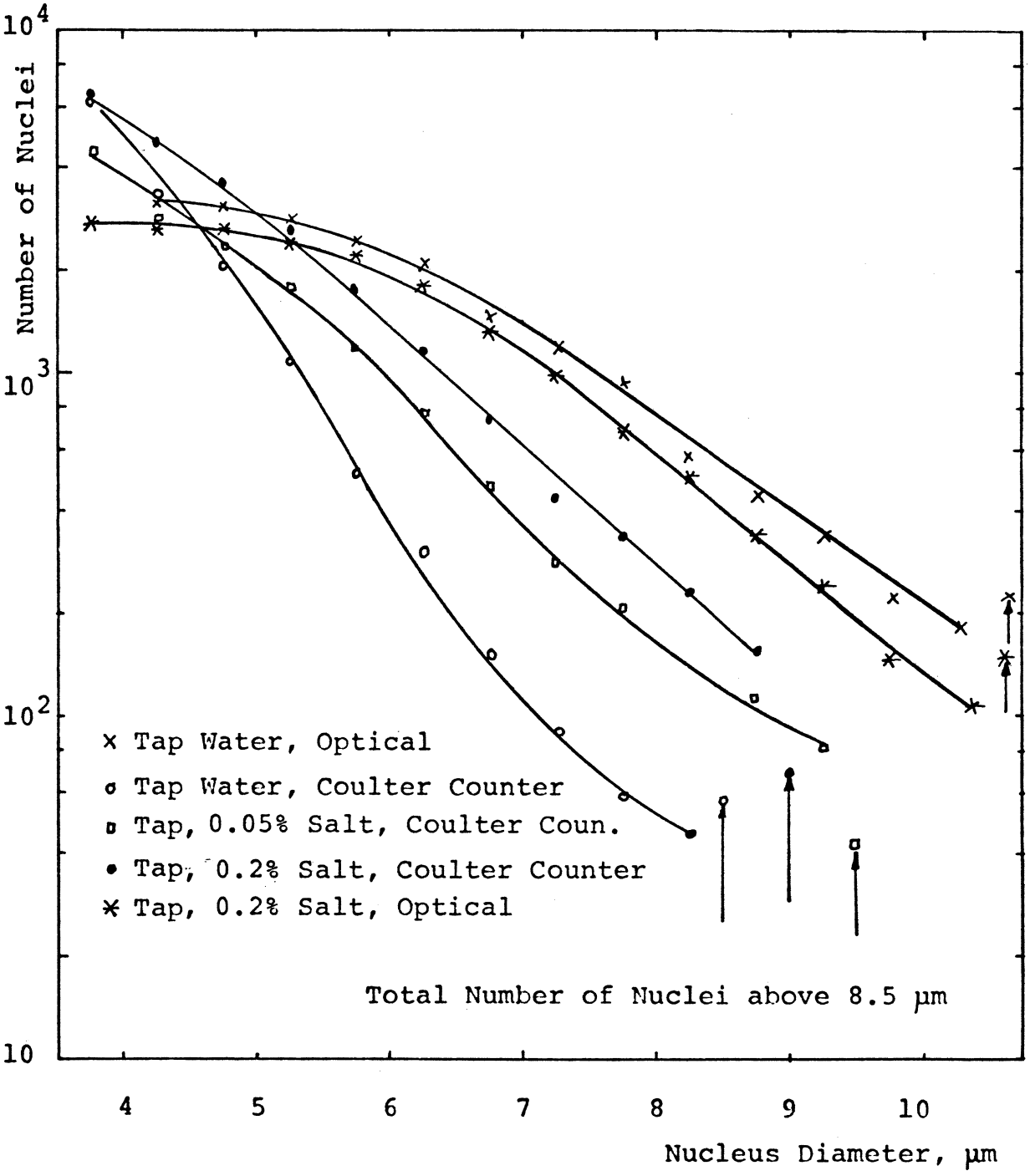

Figure 4-2 Nucleus Spectra Obtained Using Coulter Counter and Light Scattering (Optical) Methods with Different Salt Concentrations for Four Cubic Centimeter Tap Water Sample.

5049

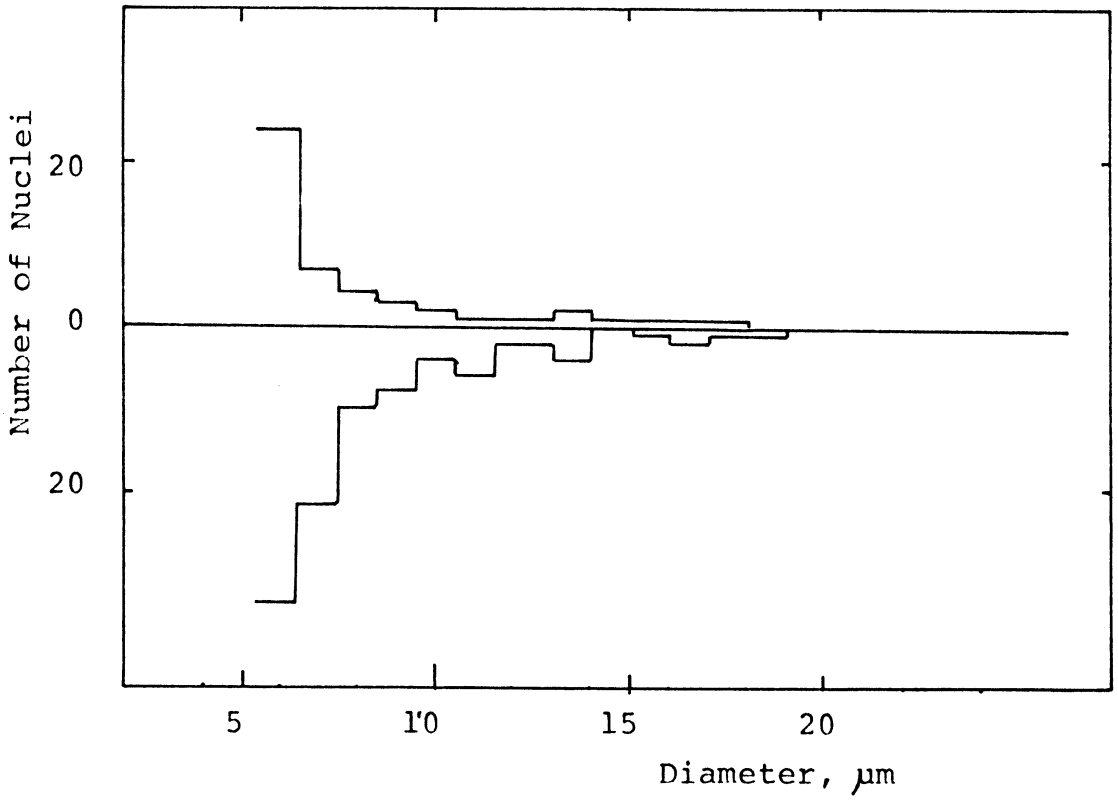

Figure 4-3 Nucleus Size Histogram of Graphite Obtained With the Coulter Counter.

5050

troublesome difficulty in some cases. As already mentioned, this total number of nuclei measured by the Coulter counter is increased to about 60% of the nuclei measured by the light scattering method after adding some salt (~ 0.1% by mass) into water to increase electrolyte conductivity. This suggests that a great number of nuclei are particles which have conductivities of at least the conductivity of tap water. In fact, ~ 1/3 of the total number of pulses were negative above 4 μm diameter [18]. This result may support the model of a gas nucleus surrounded by solid impurities or housed within a crevice in such a solid particle.

Since salt addition to the test water is not desirable in practice, the further development of the light scattering (or some other) method to measure nucleus spectrum is desirable in water containing gaseous and solid particles.

Properties of particles which were used to check the response of the light scattering system are given in Table 4-3. Particles were added to filtered (0.2 μm pore size), degassed and distilled water. The properties of the particles extended from black (graphite) to white (10 μm grit), from spherical (latex, puff ball spores) to very irregular shapes (silicon carbide, graphite), from non-conducting (latex) to highly conducting (graphite, tungsten powder), and had diversity of other varying qualities like homogenity, transparency, surface roughness or wettability. To get some information about the shape and size of particles added to the water, samples of the powders were cast in a polyster cast, and polished for microscopic examination [18]. In the histograms of these particles for which the most probable diameter was

TABLE 4-3

PROPERTIES OF THE PARTICLES USED IN

SOLID PARTICLE RESPONSE MEASUREMENTS

Substance	Color	Size (μm dia)
Tungsten powder	dark gray	6 μm most probable
Puff ball spores	brown	4-5
Paper mulberry pollen	yellow	14-18
Latex	white	6-14
Graphite	black	20 μm and less
Crystollon 400 B	dark gray	30 μm and less
Al_2O_3 powder	gray	12 μm and less
Alundum 600	gray	30 μm and less
Grit	white	10 μm

5051

known, this diameter was compared with the measured peak. Of the other powders investigated, only the maximum size was known. These histograms are not as informative as those where the most probable size is known, but they give some information about the light-scattering behavior of the respective substances, by comparing the measured maximum particle size with known maximum size. The known particle sizes and the corresponding measured pulse heights are shown in Figure 3-18. The solid line in Figure 3-18 is the calibration curve obtained using bubbles of known size and Mie theory.

Most of these experimental points lie fairly close to the curve for spherical bubbles, indicating that the scattering behavior of tiny particles do not differ substantially from that of bubbles [18, 92]. Thus, although

this optical method for determining nucleus size and number cannot distinguish between gas bubbles and solid particles, the nucleus spectrum so measured is closer to the real spectrum in water than that obtained from the Coulter method. The light scattering method was thenceforth alone for the nucleus measurements in this study.

Nucleus Spectrum Measurements

During the spectrum measurements the pump was run at 60% of rated voltage, sufficient to circulate the water at 17 cm/sec. in the 1.5-in. cm I.D. glass piping of the loop. Sampling time was varied from 1 minute to 10 minutes (corresponding to water samples of ~ 1 - 10 cc), depending on the quality of water and the experiment. For most spectrum measurements, sampling time was 4 minutes.

Most of the nucleus spectrum measurements were done together with cavitation inception pressure measurements. In this section, spectra were plotted on the same graph to see the effects of different variables. These variables are: time, gas content, temperature and particle content of the sample.

Spectrum measurements were done in two steps to cover a larger range in nucleus size. For the first step, pulse heights were stored in the MCA after amplifying by 10x. The pulse height range thus stored covers the nucleus diameter range of 4 to 10.5 μm. For the second step, the PM pulses were not amplified, and stored directly in the MCA. This pulse height range covered nucleus diameter range of 7.5 to 21 μm. A total diameter range from 4 μm to 22 μm is thus covered. The pulse

heights originating from larger than 22 μm diameter nuclei were stored in the end channels of the MCA. The storage of pulse heights larger than the MCA range was accomplished by saturating the zero-level-adjusting-amplifier.

Conversion of pulse heights to the corresponding nucleus diameters are next required. To accomplish this, pulse height spectra were integrated for the diameter ranges involved, using the trapezoid rule. A computer program for the numerical integration of the spectra was prepared (Appendix F).

The importance of settling time on the cavitation inception pressures and nucleus spectrum have been observed by other investigators, including Ahmed [13] and others in this laboratory and elsewhere. Bubbles, stabilized or free, will shrink in size due to diffusion, or reach the surface due to buoyancy, just after filling the system. Continuous nucleus reduction both in size and number is seen on Figure 4-4. The rate of size dimunition decreased with time so that finally the spectrum became relatively constant after about 36 hours.

The total gas content of water plays an important role on cavitation inception. Cavitation will be essentially "gaseous" unless the water is undersaturated. Figure 4-5 shows the effect of degassing on the spectrum, starting with slightly undersaturated water (96% saturated) down to about 21% of air saturation at STP.

The effect of temperature on the spectrum is not easy to evaluate, since there is also a time effect on the spectrum. Any correction of the spectrum for the time decay of nuclei is obviously uncertain.

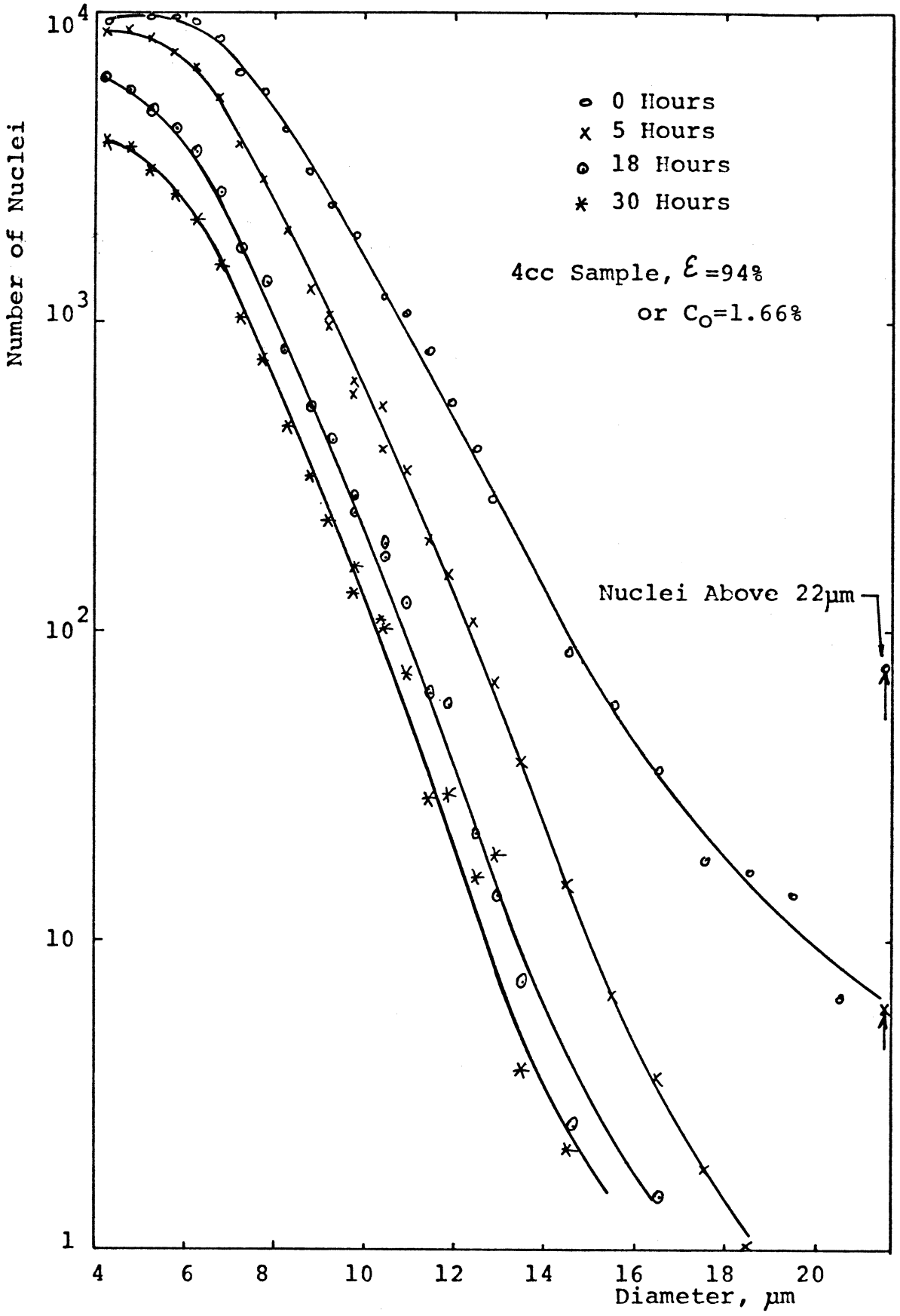

Figure 4-4 Effect of Waiting Time on Nucleus Spectrum of Tap Water.

5052

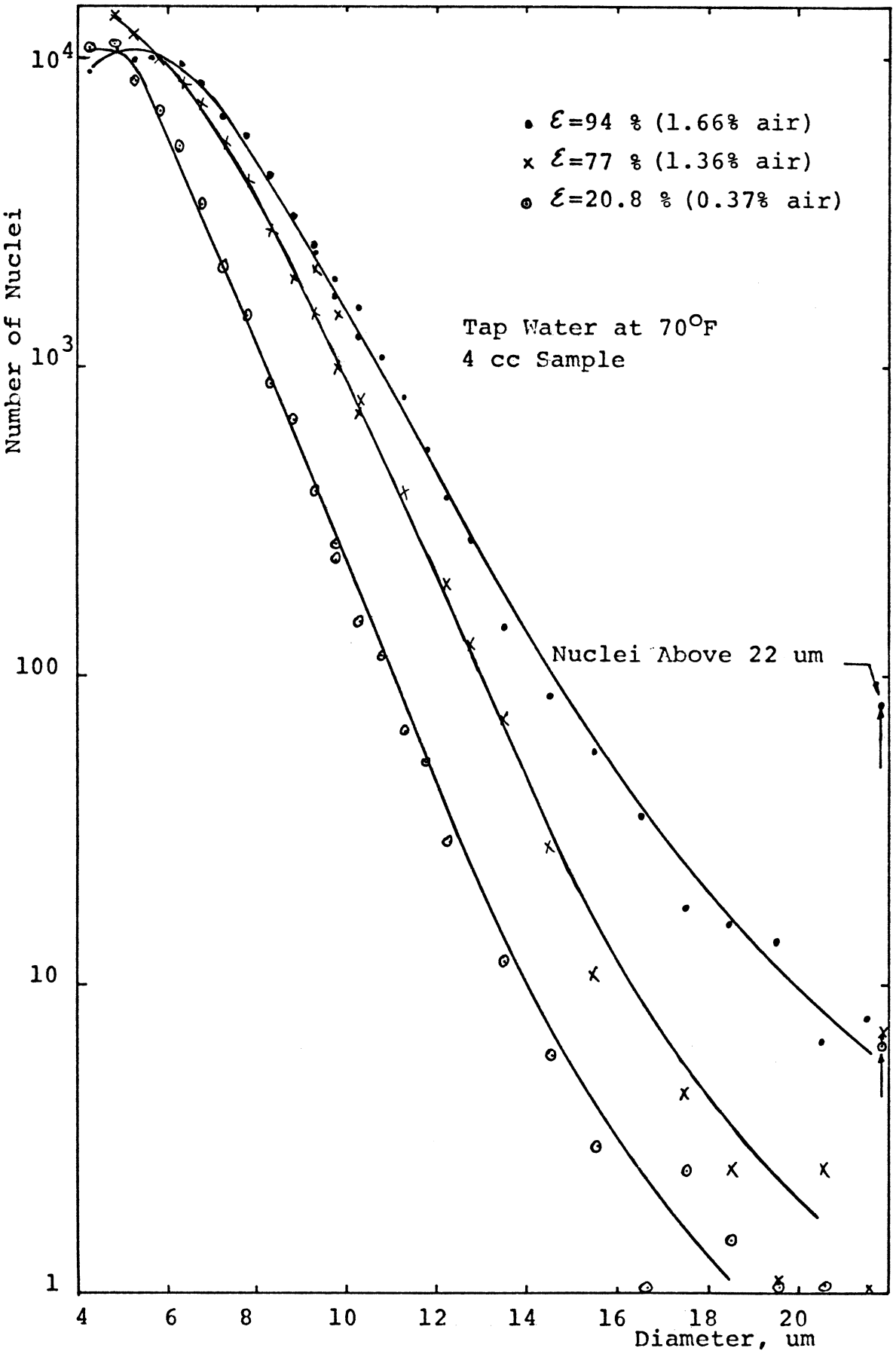

Figure 4-5 Effect of Degassing on Nuclei Spectrum.

5053

An approximate decay of nuclei by time can be estimated using Figure 4-4. The time interval on Figure 4-6, which shows the spectrum at different temperatures, for $70^{o}F$ and $140^{o}F$ is about 12 hours. The estimated time effect is also indicated on Figure 4-6. The effect of temperature on nucleus spectrum for 24 hour-old filtered and degassed water is shown in Figure 4-7.

The most important variable affecting nucleus spectrum for the tap water samples used was the solid particle content of the sample. The tap water spectra obtained using tap water on the one hand, and filtered (0.2μm pore size) tap water on the other, is given in Figure 4-8.

There was no detectable effect of a 5.9 K Gauss magnetic field on the spectrum or on nucleation threshold. The effect of the 1 Ci Pu-Be fast neutron source on the spectrum was only very slight. However, nuclei counts increased slightly with the irradiation, so that the effect was statistically valid (see Table 4-4 and 4-5). Addition of polymer (Separan AP30) also did not change the spectrum noticeably.

To measure the effect of fast neutron irradiation on nucleus count, a second Pu-Be source of the same strength was placed close to the nucleus spectrum measuring system in addition to the one which was placed at the cavitation section for cavitation inception measurements. The distance from the center of the source to the axis of the pyrex pipe section where the counting system was located, was about 1-3/8 inch. The total number of pulse heights above 200 mv (~ 4μm nucleus diameter) were counted to measure the effect of irradiation

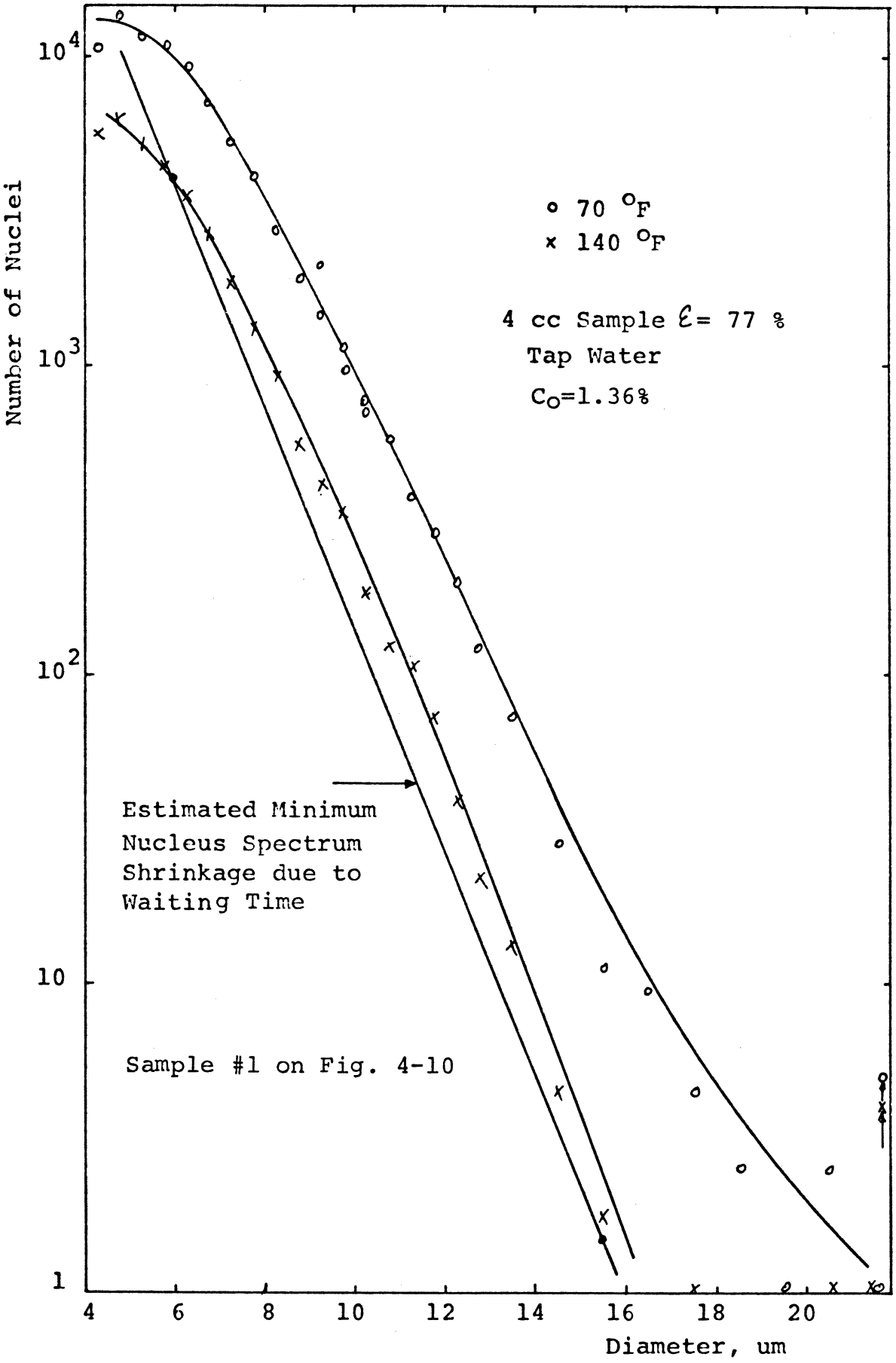

Figure 4-6 Effect of Temperature on Nucleus Spectrum.

5054

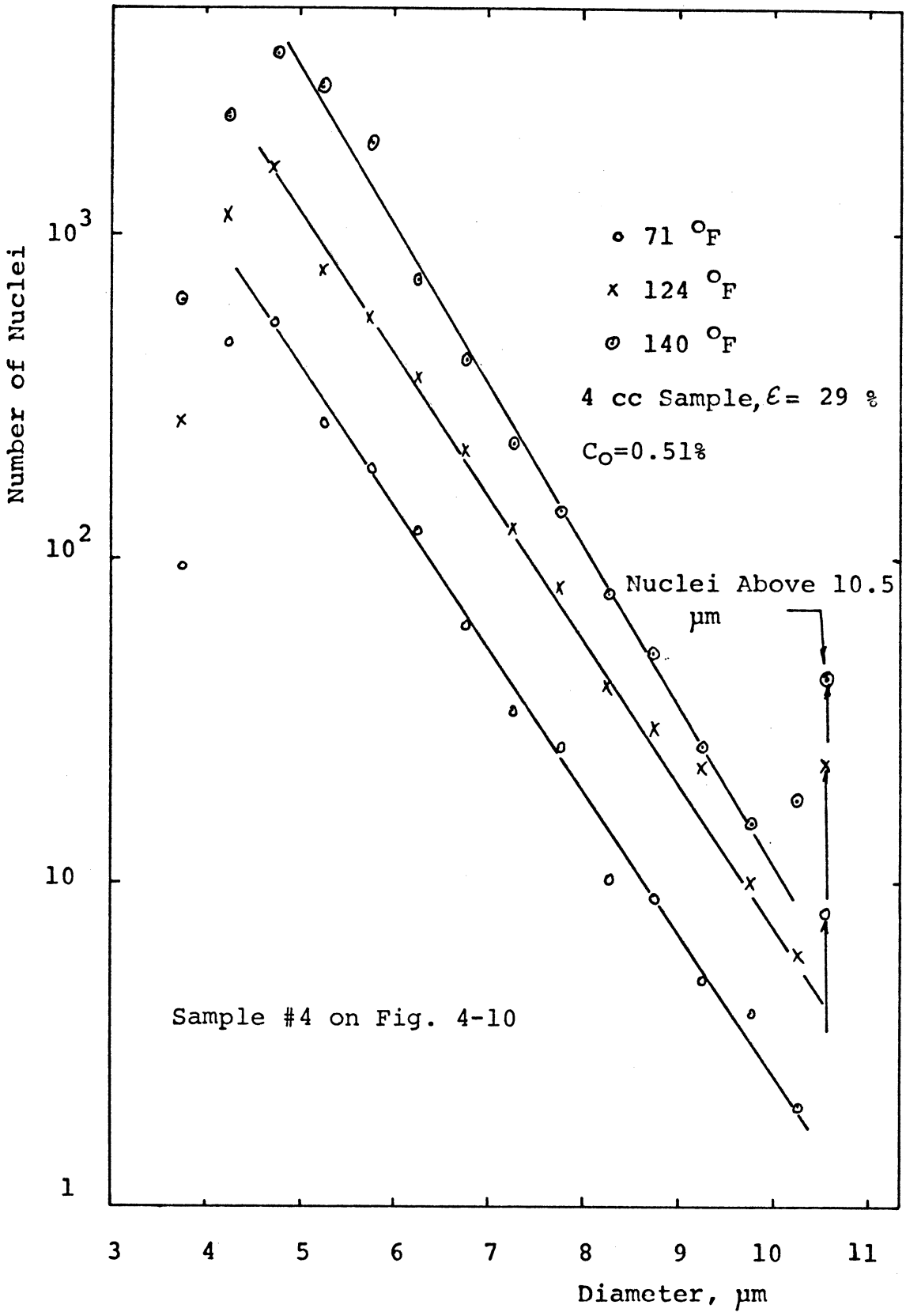

Figure 4-7 Effect of Temperature on 24 Hour Old, Filtered (2 μm), and Degassed Tap Water.

5055

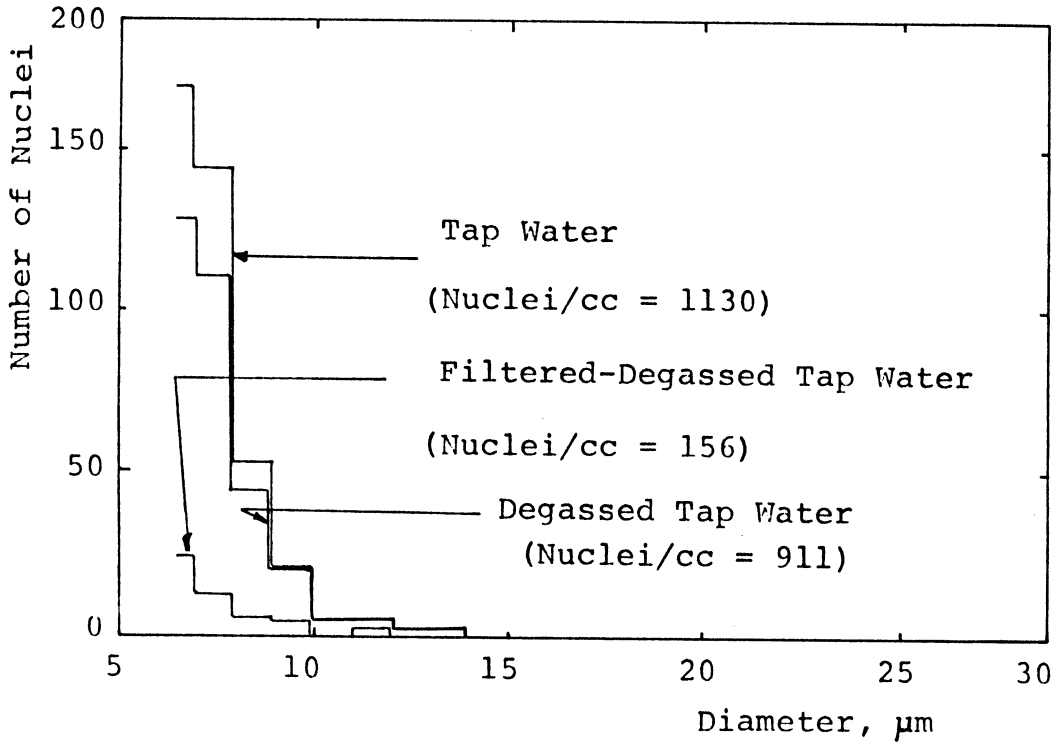

Figure 4-8 Nucleus Size Histogram of Untreated , Filtered and Degassed, and Degassed Tap Water.

5056

on nucleus count. The loop was short circuited for this experiment, so that large amounts of filtered water was not necessary. The results are given in Tables 4-4 and 4-5.

TABLE 4-4

EFFECT OF IRRADIATION ON NUCLEUS COUNT FOR FILTERED (0.45 μm), Degassed (C_o = 0.63%), AND DISTILLED WATER

	nuclei counts/5 min.				
	No Source	Source	No Source	Source	No Source
	9429	8654	8125	7549	6889
	9188	8805	7892	7335	6741
	9055	8597	7766	7127	6642
		8434			
Averages	9224	8622	7927	7337	6757
% increase		.55		-0.07	

Average increase ≅ 0.24 %

5057

The effect of cavitation on nucleus spectrum is given in Figure 4-9 for distilled, partially degassed and filtered water. For this experiment, the stilling tanks were removed and the loop was shortened. The pump was run at very low speed (40% of input voltage) to make sure that there was no nuclei generated by the pump. Cavitation duration was about 9 minutes and cavitation intensity was about that of the inception point (~ 5.7 bars).

TABLE 4-5

EFFECT OF IRRADIATION ON NUCLEUS COUNT

FOR DEGASSED (C_o = .4%) AND FILTERED (2μm)

TAP WATER

	Nuclei count/5 min.				
	No source	Source	No source	Source	No source
	38795	38635			
	39498	37563	73957	71957	69102
	38695	36939	36332	36012	34059
Averages	38996	37712	36540	35989	34387
% increase	-.15%			1.48%	

Average increase $\tilde{=}$ .65%

5058

Cavitation Inception Pressures

Inception pressure measurements were made using tap water as a test fluid under different nuclei content conditions. The pump circulated the water at about 17 cm/sec in 1.5-inch I.D. pipes. Thus, the water velocity in the vicinity of the horn tip was also about 17 cm/sec. When a liquid in which there are pre-existing nuclei is introduced into a sound field, cavitation will appear as soon as nuclei find themselves in a region where the sound pressure is sufficient for their growth. There will then be a certain probability of observing cavitation in the liquid under a fixed pressure field. This probability will depend on the nuclei distribution, as well as the duration of acoustic

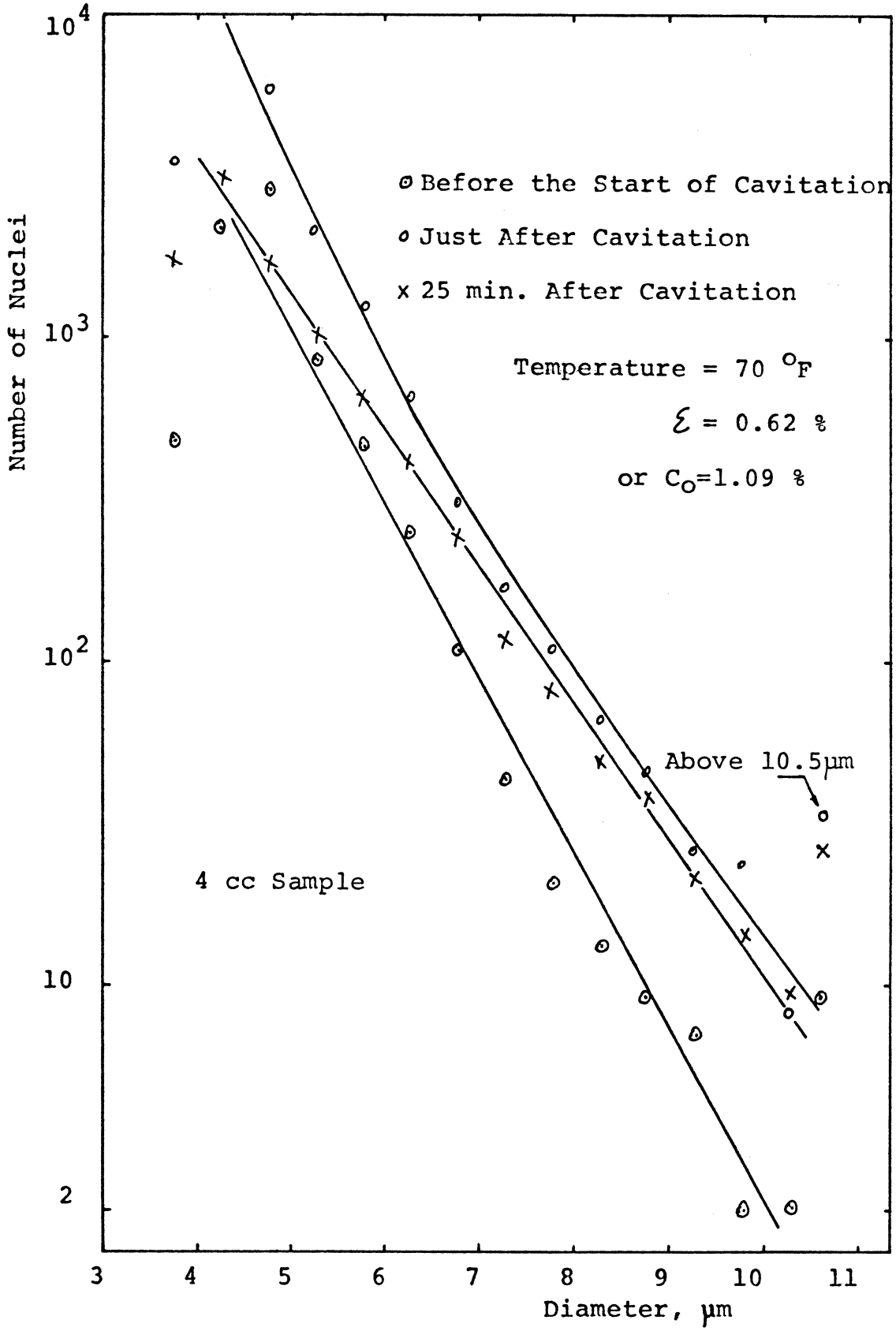

Figure 4-9 Effect of Cavitation on Nucleus Spectrum for Distilled, Filtered(.45 μm) and Degassed Water.

5059

pressure and flow speed. Messino et al. [93] found that the majority of cavitation events occurred in less than 4 sec. after the sound field turned on. They found it plausible to assign events with delay shorter than 4 sec. to the pre-existence of suitable nuclei in the liquid. When water is flowing the waiting period should decrease proportionally depending on the flow speed. An accepted procedure for the threshold measurement is to increase the sound amplitude in steps. After each step, sound field is left for a certain period, Δt_1, and turned off for a duration of Δt_2. Whenever a cavitation event is detected, the sound field is turned off for a period Δt_3. Since most of the investigators worked with stationary systems, their only water flow was caused by the acoustic field itself ("acoustic streaming"). The water sample being irradiated by the acoustic field changes rapidly due to the imposed flow. For the experiments conducted for this investigation Δt_2 and Δt_3 were about 0.1 second. 0.1 sec. was calculated using the length of acoustic field of about 1.7 cm and a flow speed of about 15 cm/sec. through this field.

The acoustic pressure was increased manually at a linear rate of about 0.2 bar/sec. in the range where there was a finite probability of having a cavitation event. The rate of increase of acoustic pressure in regions where there was almost no probability of cavitation, was faster.

Cavitation threshold measurements were done for different qualities of water. The effects of temperature, waiting time, magnetic field, fast neutron irradiation and addition of different types of

particles were also investigated.

The effect of temperature on cavitation inception is given in Figure 4-10 for two samples of slightly degassed water, degassed water, and filtered and degassed water. Points denoted as "theoretical" will be explained later. Sample #1 on Figure 4-10 is slightly degassed such that at higher temperature water will be about air saturated. 77% air saturation at room temperature will be 100% air saturated at about 110°F. Sample #2 was about 46% air saturated and reaches full air saturation at 140°F. Air saturation as a function of temperature for water is given in Figure 4-11. Dotted line is the extrapolation of the data available up to 86°F.

Sample #3 is the same sample as for #1. Degassing was done at about 135°F to further reduce gas content. Cavitation inception measurements were done for sample #3 when water sample was about 24 hours old. Sample #4 was a filtered and degassed sample. A 2μm pore size, in-line filter was used to filter the water sample during filling of the system. Degassing is accompanied by running the circulation pump at full speed and evacuating the system with a vacuum pump continuously.

Nucleus spectrum for samples #1, #2, #3 and #4 are given in Figures 4-6, 4-12, 4-13 and 4-7 respectively. Spectra in Figures 4-7 and 4-13 are for two samples of water which were settled for about 12 hours after degassing. The decrease of spectra as temperature increases is due to faster settling time compared to growing time

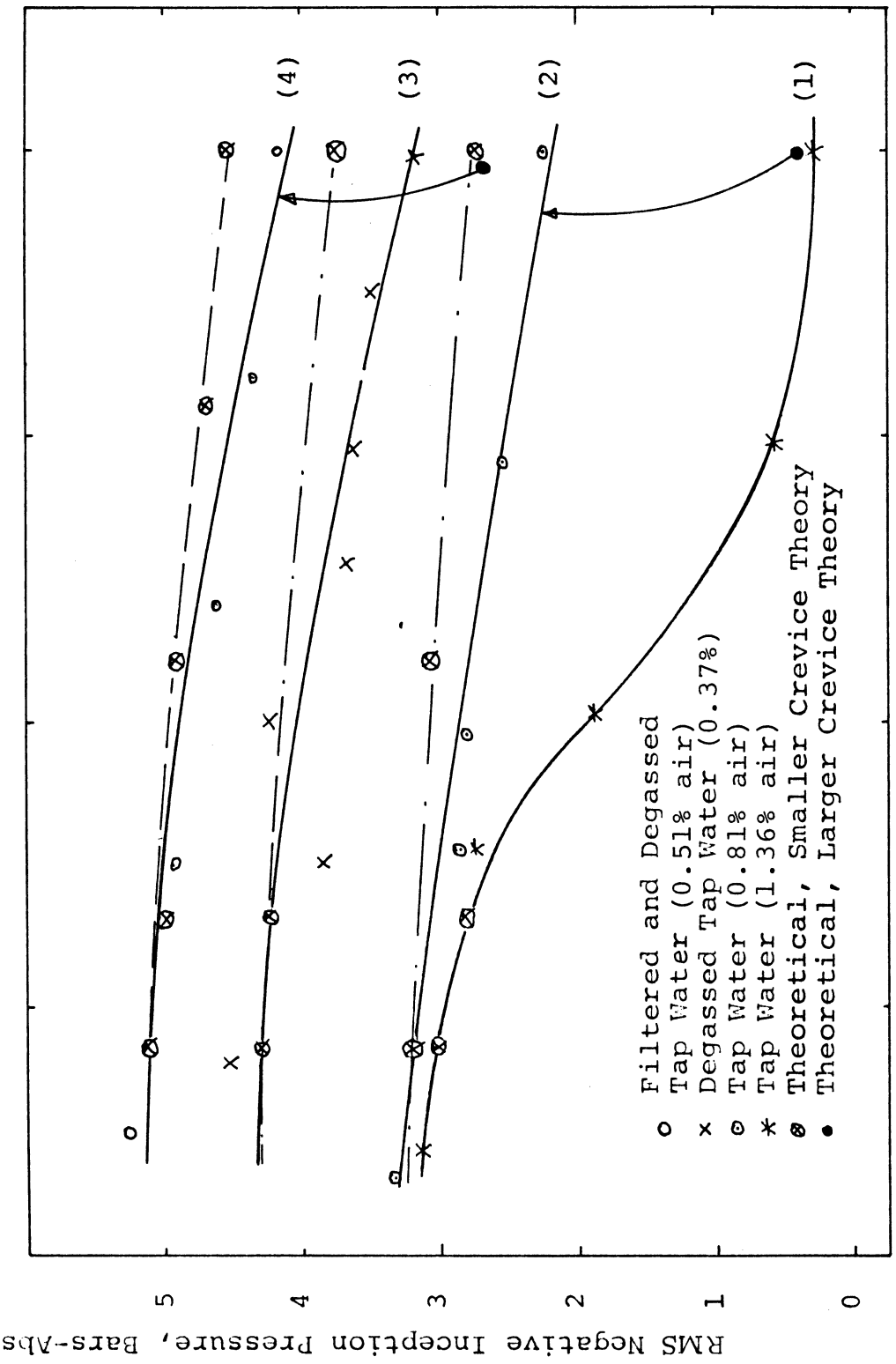

Figure 4-10 Influence of Temperature on Cavitation Inception Pressure.

5060

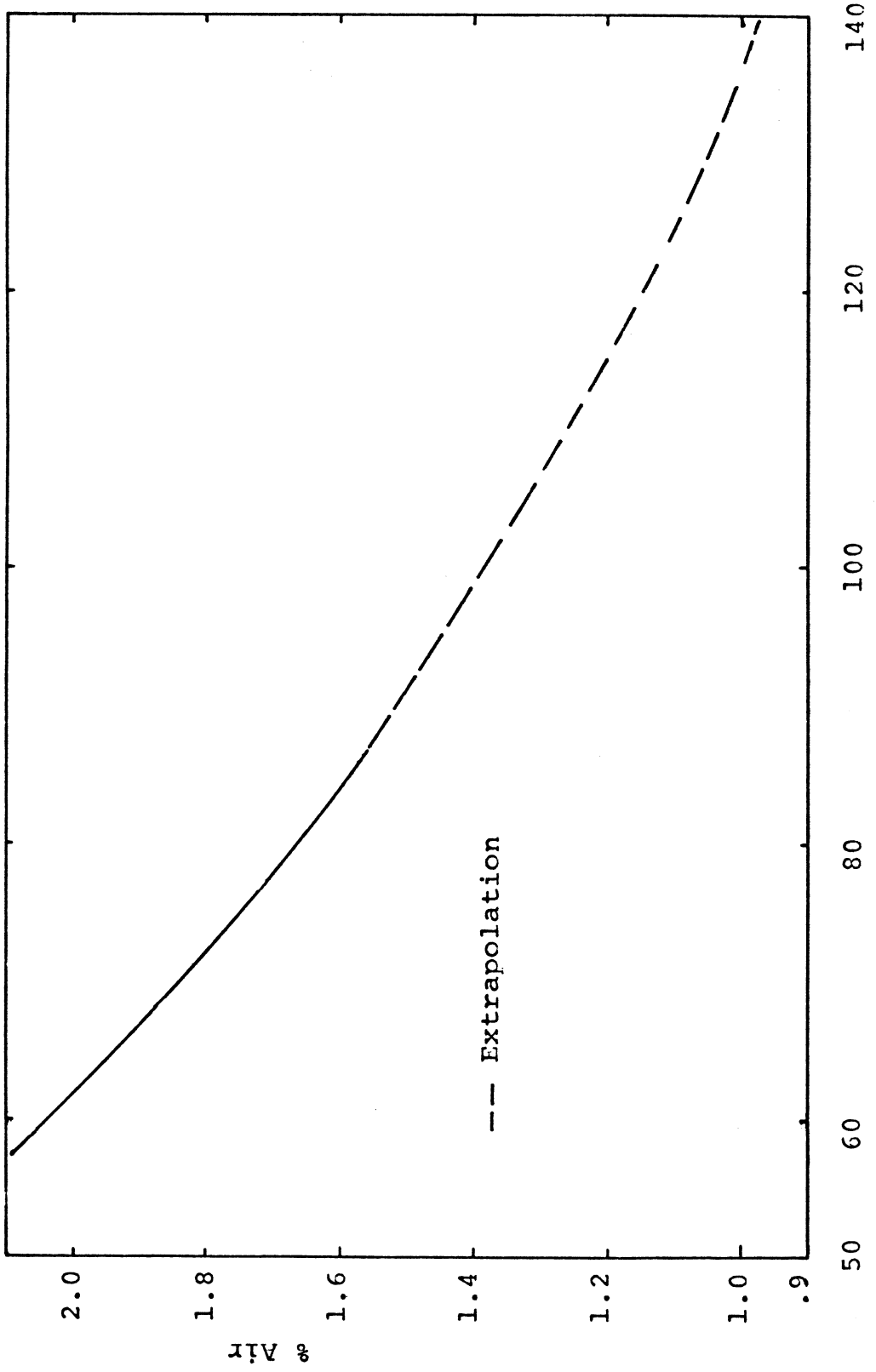

Figure 4-11 Air Saturation of Water as a Function of Temperature at one Atmosphere.

5061

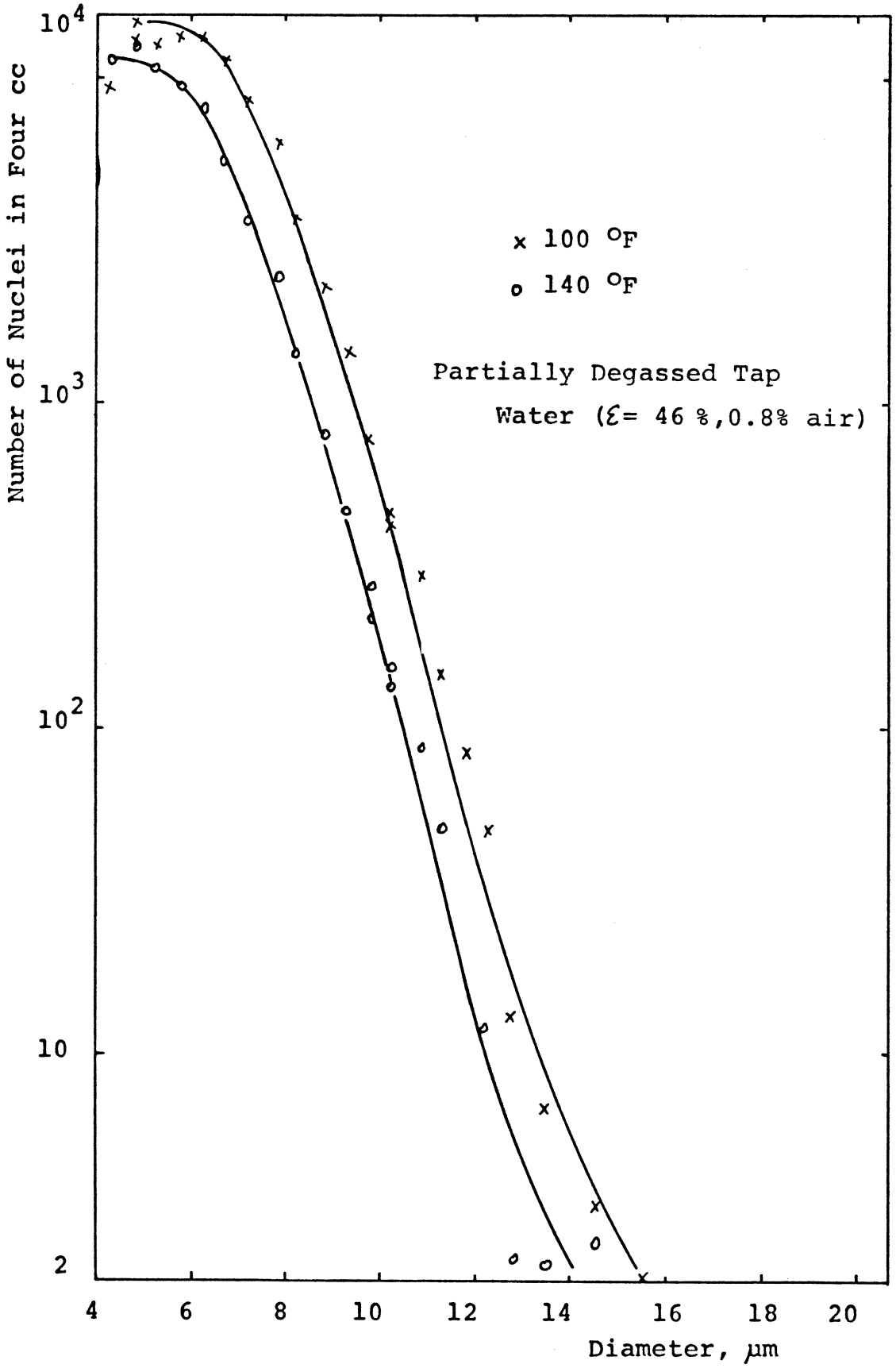

Figure 4-12 Nucleus Spectrum for Sample #2 in Figure 4-10.

5062

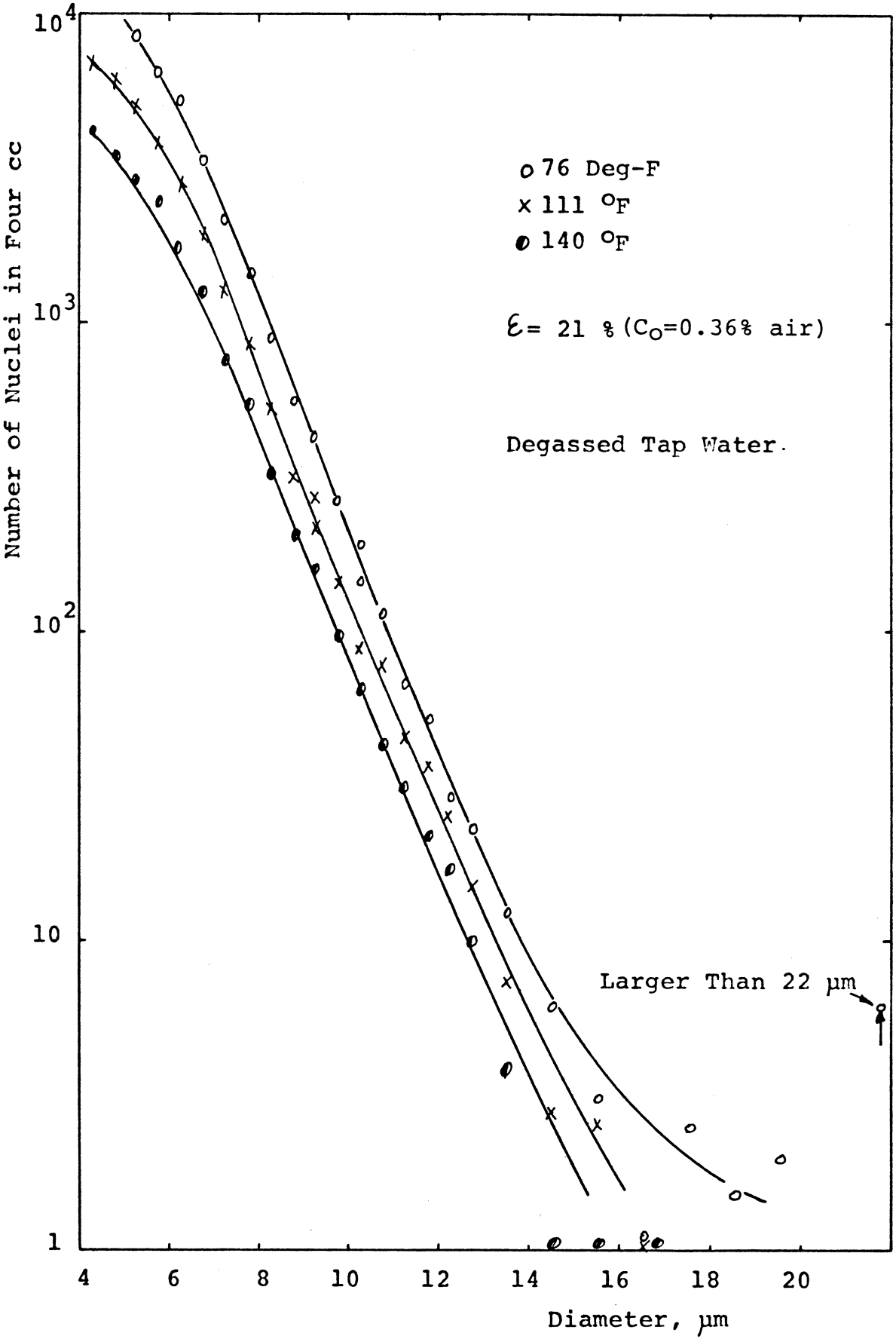

Figure 4-13 Nucleus Spectrum for Sample #3 in Figure 4-10.

5063

of nuclei by temperature.

The effect of air content on cavitation inception pressures is shown in Figure 4-14. Two samples are shown. The first is for ordinary tap water, the second for filtered tap water. A 2μm pore size, in-line filter was used for filtering. An inception point which belongs to a different tap water sample is also shown in the same figure. Degassing is accomplished by circulating the sample under vacuum. Van Slyke gas content measurements were always made at least twice. If two measurements differed appreciably the measurement was repeated. Nucleus spectra at cavitation inception are given in Figure 4-15 and 4-16.

The effect of waiting time on cavitation inception pressure is given in Figure 4-17. Waiting time effects on nucleus spectrum is given in Figure 4-4. Sample was slightly undersaturated (94% of saturation). Temperature of sample was monitored continuously. It was about $74.5^{o}F. \pm .5^{o}F.$ during the course of measurement.

Fast neutron and cosmic ray irradiation effects on cavitation inception is reported by various investigators [75-79]. To investigate this effect, one or two Pu-Be sources of each 1 C_i (1.2×10^6 neutrons/sec) were placed in the stilling tank #2. No measurable effect of neutron irradiation was found either on the cavitation inception pressure or on the nucleus spectrum when sources were in stilling tank #2.

About 3% decrease with neutron irradiation of cavitation threshold was measured for a sample of degassed tap water (sample #1) which had been in the system for about 52 hours. The variation of

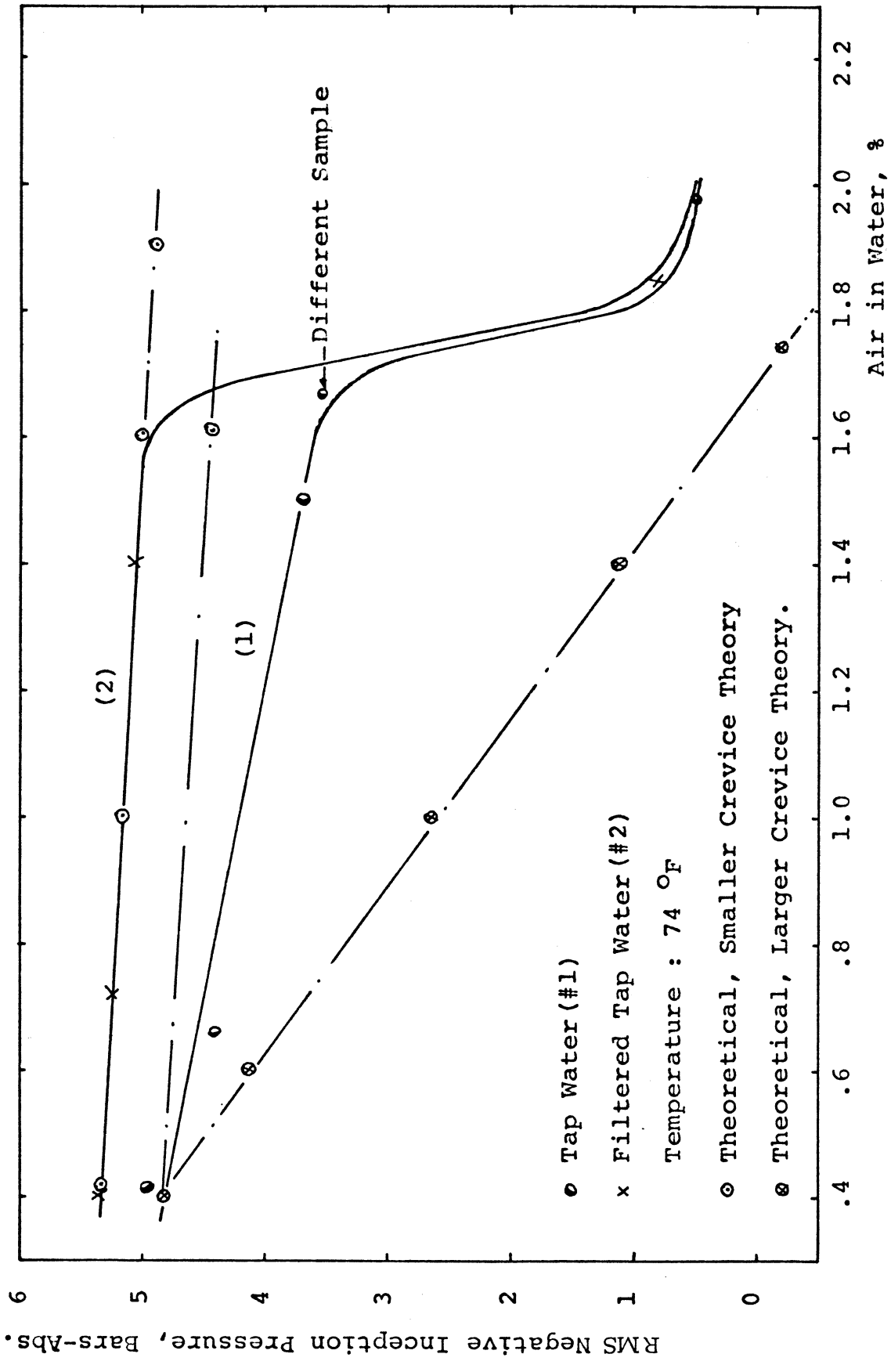

Figure 4-14 Effect of Air Content on the Inception Pressure for Cavitation.

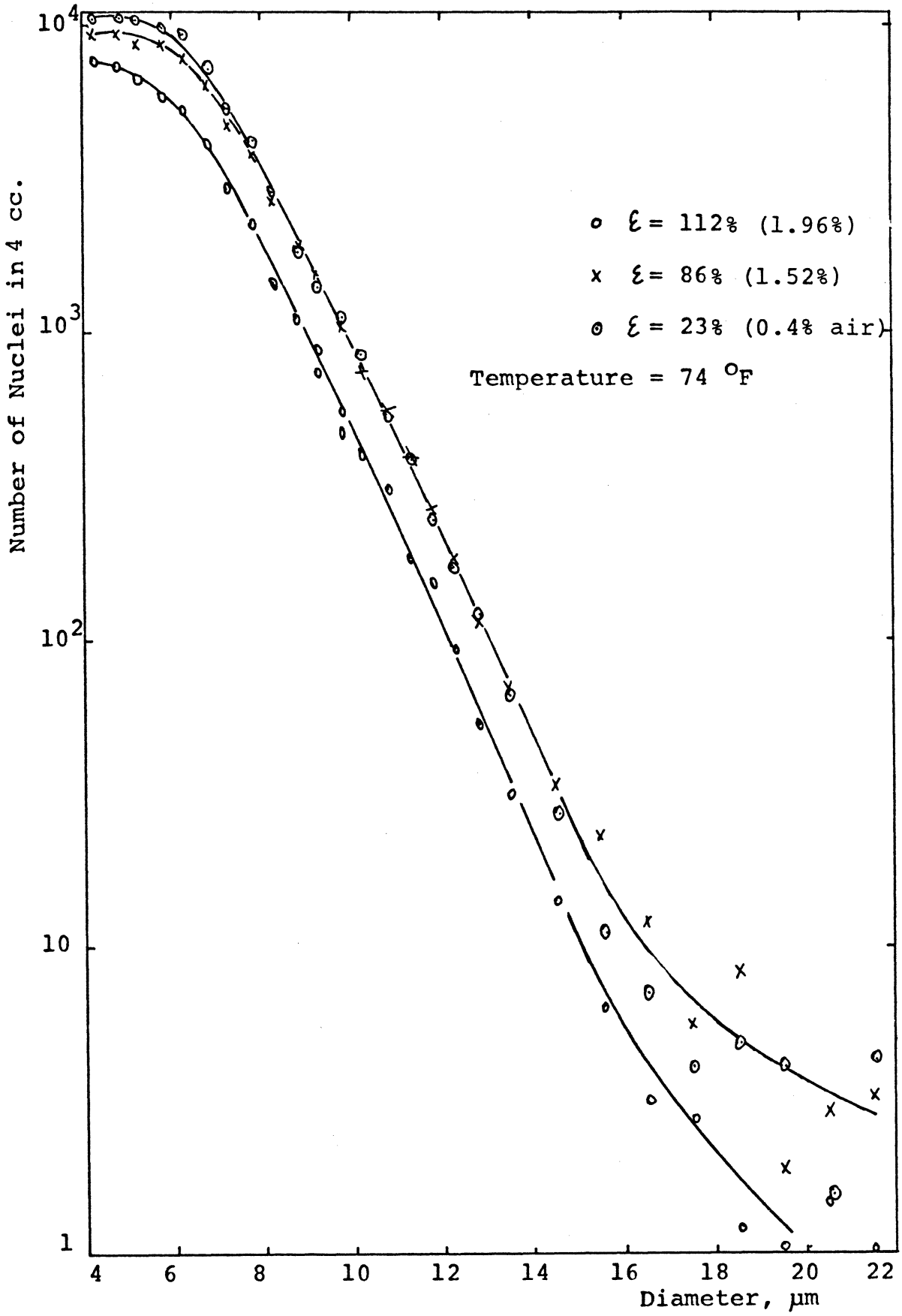

Figure 4-15 Nucleus Spectrum for Sample #1 in Figure 4-14.

5065

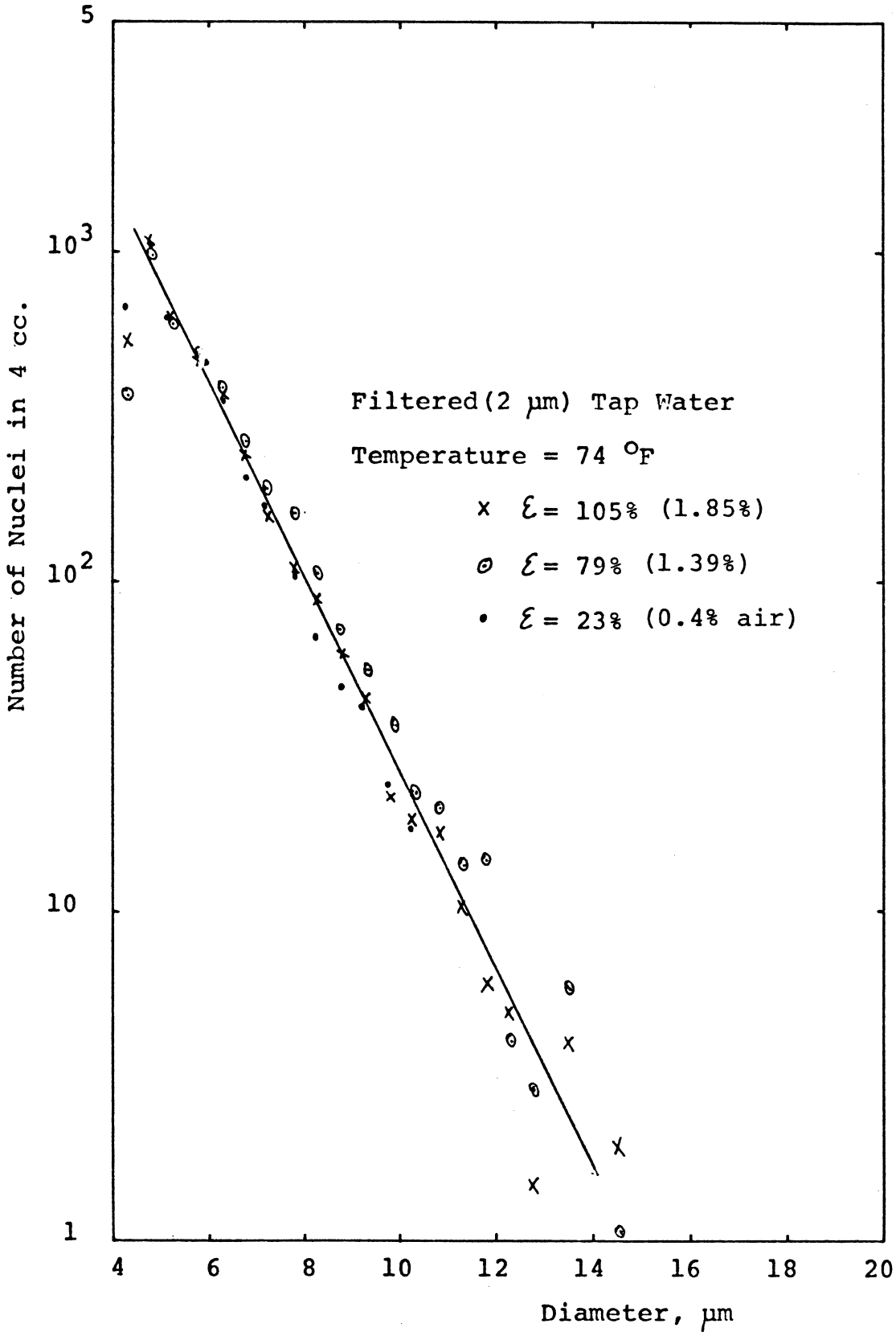

Figure 4-16 Nucleus Spectrum for Sample #2 in Figure 4-14.

5066

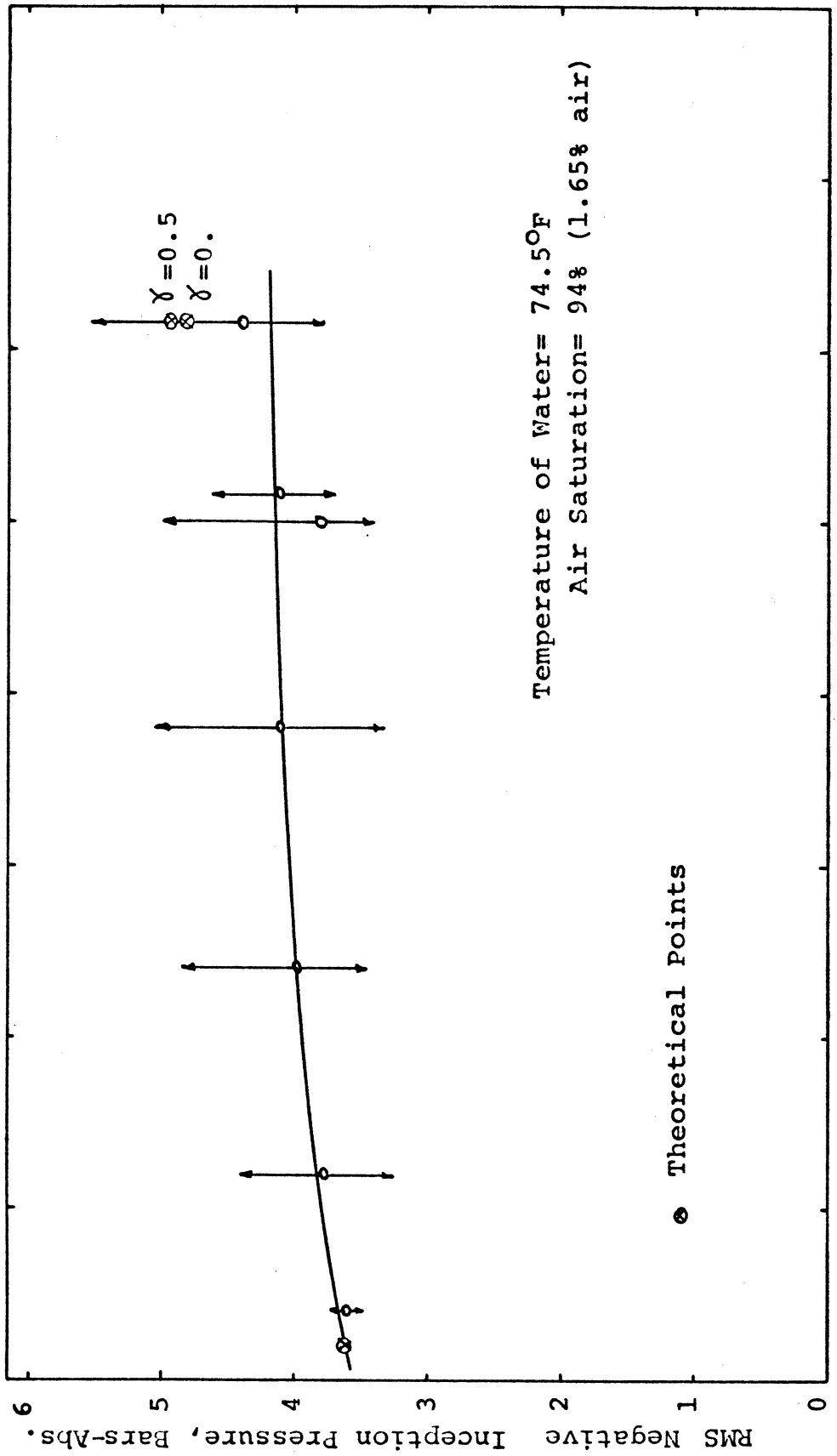

Figure 4-17 Effect of Waiting Time on Cavitation Inception Pressure for Slightly Degassed Tap Water. 5067

inception pressure for cavitation is given in Figure 4-18. The neutron source, in this case, was just outside the cavitation vessel. The distance between the centerline of the vessel (pipe) and source was $\sim 1-\frac{3}{8}$ inch.

Decrease of cavitation threshold was less when the inception point of the sample was low. Table 4-6 gives the results obtained using a filtered (2μm) and degassed tap water sample (#2) at room temperature (74°F.) and 40% pump speed so that circulation rate was relatively low. Each cavitation inception pressure is an average of $\geq$ 15 inception measurements.

No effect of a 5.9 K gauss magnetic field in the cavitating region was seen on cavitation inception measurements.

The effect of the addition of different particles to the degassed and filtered (2μm filtered) tap water, on the cavitation inception pressures, were also investigated. The flow system was "short-circuited" (no stilling tanks) and the pump was run at 40% rated voltage (117 VAC). At this pump speed water velocity was 9 cm/sec. Since the nuclei concentrations of the added particles were not known, the results obtained are qualitative only. Properties of the particles used in these experiments are given in Table 4-3. Table 4-7 summarizes the experimental results obtained. Inception pressures given on the table are averages of at least ten measurements. Total water volume in the loop was about 1 gal. Water, after degassing, was circulated for 10 min. before any measurements were taken. Air content of the samples were about 30% of saturation at room temperature (C_o = 0.53% air).

TABLE 4-6

RESULTS OF IRRADIATION EFFECTS ON CAVITATION INCEPTION

FOR FILTERED TAP WATER

Process	Time elapsed hours	Average inception pressures, bars.				
		No source	Source	No source	With source	No source
Fill and measure (C_o = 1.75%)	0	No effect of irradiation is seen.				
Degass (C_o = .39%)	1					
Measure	4	5.72	5.73	5.82 5.88	5.77 5.89	6.04 5.98
Averages		5.72	5.73	5.84	5.83	6.01
% decrease		.7%		1.55%		

Average cavitation threshold pressure decrease $\cong$ 1.1%

5068

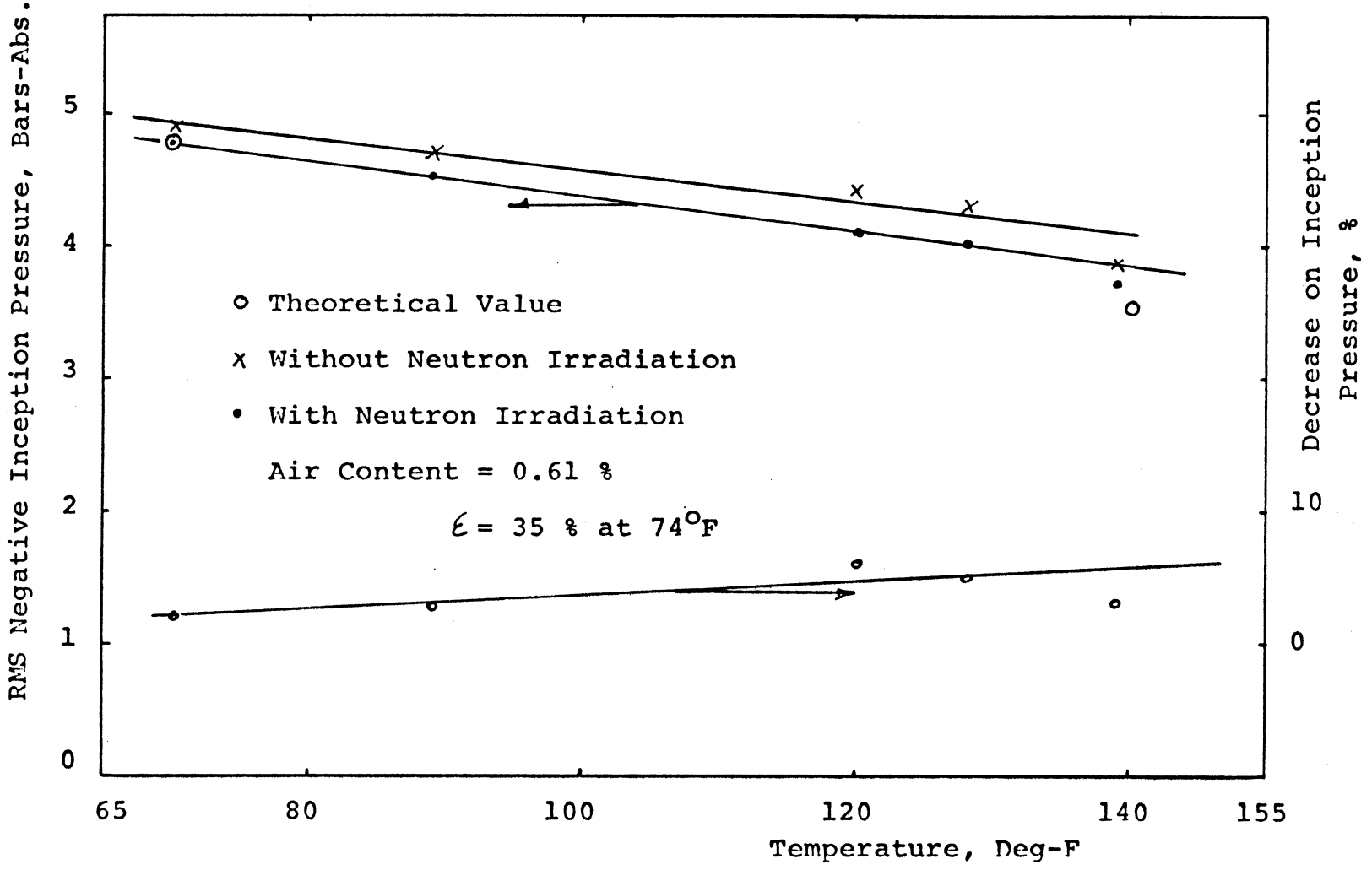

Figure 4-18 Influence of Fast Neutron Irradiation on Inception Pressure for Cavitation.

5069

TABLE 4 - 7

EFFECT OF PARTICLE ADDITION ON THE CAVITATION INCEPTION PRESSURES FOR DEGASSED AND FILTERED (2μm)TAP WATER

Sample #	Particles added	Inception pressures, -Bars-RMS		Amount added or counts before/after	% Decrease on inception
		Without particles	With particles		
1	6-14μm Latex	6.1	5.13	3 drops of solution	15.8
2	"	6.56	5.47	1 drop of solution	16.5
		5.26	5.16	3 additional drops	3.86
3	14-18μm Paper Mulberry, 6-14μm latex	5.93	7.65	10 drops of paper mulberry solution	-28.8
		7.65	5.65	1 drop of latex solution	26.2
4	Tween 80 (Wetting agent)	6.04	7.71	2 drops	-25.3
5	Graphite (≥20μm)	6.34	6.01	5 drops of solution	5.08
6	Graphite (≥20μm)	6.59	6.05	40/270	8.2
7	12.5 μm AlO_3, Tween 80	6.45	5.42	10 drops of solution	16
		5.42	6.33	1 drop of Tween	-14.5
8	Alundum 600 (≥20μm	6.05	6.04	35/380	- 0.2
9	"	5.92	6.03	10/270	- 1.75
10	Crystolon 400B(SiC) (≥30μm)	6.62	5.11	5/250	22.9
11	Latex 5.02μm	6.15	6.18	25/30	- 0.37

The effect of polymer addition is given in Table 4-8. A polymer solution of 100 cc was prepared using 0.5 cc of polymer, and 3 cc of methanol and water. The concentration of polymer in the short-circuited loop was about 0.05 ppm/drop-of solution by volume. Tap water samples were used for the experiment with two different degrees of air content.

TABLE 4-8

EFFECT OF POLYMER (SEPARAN AP 30) ADDITION

ON CAVITATION INCEPTION PRESSURES

Sample #	Air content % of Saturation (% air)	Inception pressures, bars		Concentration ppm	% increase
		Before addition	After addition		
1	30 (0.53%)	6.0	7.03	.05	17
			7.0	.1	17
			7.27	.25	21
2	51 (0.9%)	4.75	4.76	.25	0
			5.05	1.0	6.3

5071

CHAPTER V

COMPARISON OF THEORY AND EXPERIMENTS, AND DISCUSSION OF THE RESULTS

Nucleus Spectrum Measurements

Comparative Measurements

Nucleus spectra of quiescent tap water taken with the Coulter counter show [18] that water contains particles of electrical conductivities ranging from much more to much less than tap water. Therefore, this method presents difficulties in measuring the nucleus spectrum of water. The spectra would not be completely reproducible because of the large range of electrical conductivities of the particles present. Large positive Coulter counter pulses could arise from relatively small particles with very high resistivity, where as small Coulter pulses may be caused by big particles with a resistivity close to that of the water. Thus there is not a one to one correspondence in general between particle size and pulse height, and in addition the results depend importantly on the water conductivity. The assumption that water contains only nuclei with much higher resistivity than the water itself is not in general applicable. However, this situation is necessary if the Coulter counter results are to be considered reliable. In the experiments, even after adding a certain amount of salt to the water (up to 0.2%), negative pulses were measured indicating the presence of particles with higher conductivity even than that of this water–salt solution. Addition of salt increased the number of nuclei which have larger

resistivities than that of the elctrolyte. For example, the ratio of negative pulses to positive pulses was 0.72 for tap water, 0.17 for tap water with 0.05% salt, 0.09 for tap water with 0.1% salt and almost zero for tap water with 0.2% salt thus giving some idea of the maximum particle conductivity in these experiments. Of course these particles may be composite solid-gaseous aggregates such as might result from gaseous bubbles whose surface is contaminated with particulate matter which also stabilizes the bubble against outward diffusion of the gas.

The above ratios are the ratios of pulses which were measurable. The nucleus range for positive pulses corresponds to 5-8 μm particle diameter. The same pulse height ranges were used for both positive and negative pulse counts. The ratio of number of negative pulses to positive pulses for 3.5-8 μm diameter nucleus range is 1.35. Under the conditions that resistivity of particles are too far from the resistivity of water, negative pulses will be proportional to radius of particles, R, instead of R^3 as is the case for positive pulses. The ratio of pulse heights for positive and negative pulses of a given radius is

$$\frac{(\rho_o/A^2)(\frac{4}{3}\pi R^3)}{(2/A)\rho_o R} = \frac{2R^2}{A} \ll 1.$$

This means that pulse heights for particles which are more conductive than the electrolyte will be larger, compared to the positive pulses generated by less conductive particles, compared to electrolyte, of the same size. The ratio is 1:480 for 4μm diameter nucleus for the 70 μm diameter Coulter tube orifice used in these experiments.

Figure 4-1 and Table 4-2 summarizes the results of the comparative measurements in Chapter 4. Two measurements of the nucleus spectrum were made using the light scattering method for each nucleus spectrum obtained using the Coulter counter; once before and once after the Coulter counter measurement. The spectra obtained before the start and at the end of the experiment differ by no more than about 20 %, using the light scattering method.

Comparison between the spectrum obtained using the Coulter counter with the 0.2% salty water, and the spectrum obtained using optical methods, indicate that there were particles in water which had conductivities close to that of tap water. Comparison of the various Coulter tests with water of different conductivities indicates the same thing. The relationship between nucleus size and number for the two methods of measurement was found to be very similar. Slopes of these two curves, if approximated by a linear relationship, are about the same for nuclei having diameters larger than 5.5 μm (Figure 4-2). The leveling-off of the optical system spectrum is because of the electronic system.

The peak detector will gate the MCA for larger pulses, if partial coincidences of two or more pulses occur. Figure 5-1 may help to explain the situation. Only at time t_2, at which time the pulse crosses the trigger level of the trigger, the MCA will be gated. At this time the peak detector output will be the pulse height of the larger nuclei. These pulses are shown by the dotted lines in the figure. Partial or full coincidences of nuclei will increase when nucleus

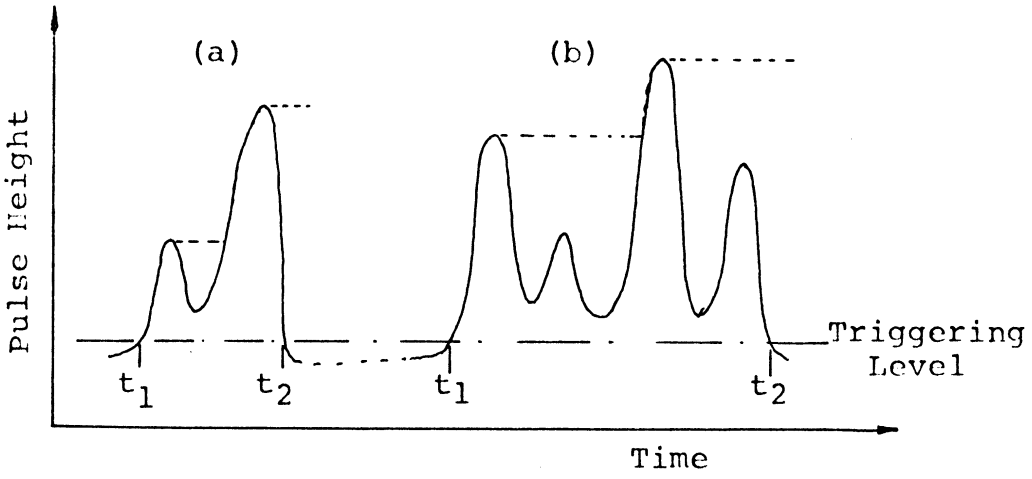

Figure 5-1 Partial Occupation of Control Volume by More than One Particle.

5072

concentration increases. The relative probability of two and three nuclei being in the control volume ($\sim 0.5 \times 10^{-4}$ cm^3) is given in Figure 5-2 [18]. Thus coincidence error for nuclei having diameter $\gtrsim$ 5 μm is about 7% for the light scattering system. Coincidence error for Coulter counter is about nil.

The electronic system was so adjusted that pulses of amplitude $\geq$ 0.1 V would be absolutely stored in MCA. 0.1 V pulse height corresponds to ~ 5 μm nucleus diameter at 10x amplification.

As Table 4-2 indicates, the number of nuclei counted in the 5-8 μm diameter range by Coulter counter in 0.2% salt water is only about 60% of the nuclei counted by the light scattering system for the same nucleus size range. If the system cannot tolerate ~ 0.2% salt, or if it is not practical to use an additive, the Coulter system cannot be used for nucleus size or spectrum measurements. Nevertheless, this method is useful for measuring the nucleus spectrum in disturbed water where free gas bubbles predominate over other particles as in a water tunnel system, as has already been done for sometime in this laboratory [13].

Effect of Different Variables on Nuclei Spectrum in Water

The most predominant effect on nuclei spectrum is obtained by filtering the water. By filtration, most of the large nuclei are removed by the filter. The effect of filtration is clearly seen in Figure 4-3. Particles larger than the filter size (2 μm pore), persist in the system. Some of these large particles no doubt come from the

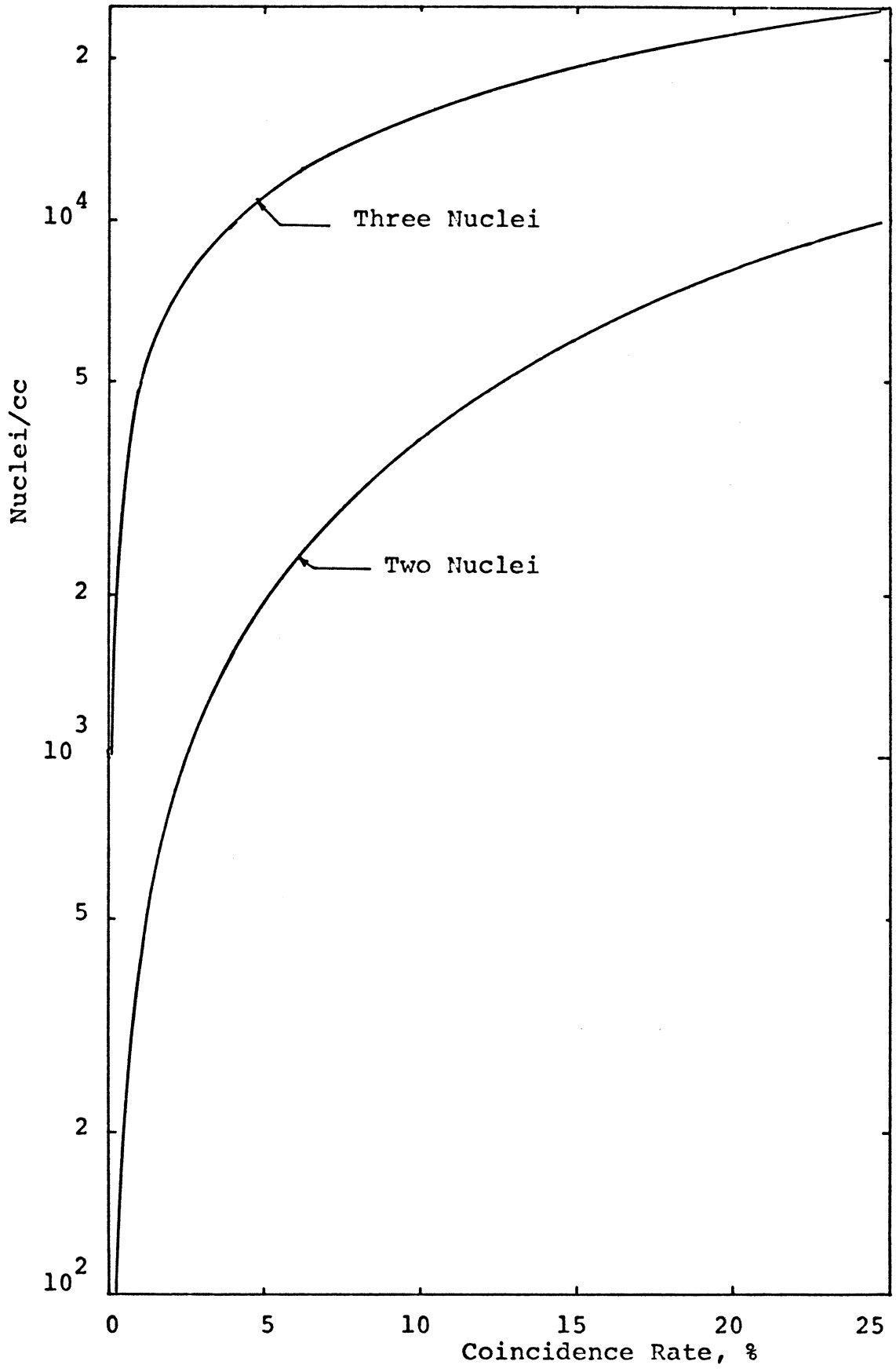

Figure 5-2 Relative Coincidence Rate for Two and Three Nuclei

system walls, but most of them actually apparently pass through the filter, perhaps due to non-uniformity of pore size.

Another variable which effects the nuclei spectrum is the air content. Effect of air content is given in Figure 4-5. As is observed, degassing is not as effective as filtration in reducing nuclei spectrum. A comparison of the nuclei spectra of gas saturated and degassed tap water makes clear that the main part of the scattered light of nuclei in unfiltered tap water must originate from the contaminated particles in the water. The spectrum after degassing shifted to moderately smaller sizes of nuclei. In degassed water, the gas cavities are maintained to some extent within crevice or pores, where they cannot contribute to the light scattering. A settling time effect is not important in the degassing effect experiments, since any settled particles will be stirred up during degassing.

The effect of settling time on nucleus spectrum also is important. During such time, large bubbles will float to the surface, small bubbles will dissolve, large particles will settle and air in the pores will shrink as they reach equilibrium with the surrounding water. Equilibrium was approached asymptotically with time (Figure 4-4). Relatively time-stabilized nuclei spectra were obtained only after 36 hours of waiting time.

Measurements of the effect of temperature is most difficult since that of time is also inevitably involved. About 8 hours was needed to complete measurements and to increase temperature of water from about $70^{\circ}F$ to $140^{\circ}F$. Temperature should increase nuclei size due

to expansion of entrapped gas and vapor, and decrease in air solubility, increasing entrained air for fixed total air. As solubility of air decreases in water, some of the previously dissolved air will diffuse into the bubbles in the crevices or other nuclei. Since the dissolved volume is very large compared to the entrained, a small change in temperature and hence gas solubility may have a large effect on entrained spectra. Contrary to what was expected, however, a decrease in nuclei size and number was found for a temperature increase for tap water (Figure 4-6). This result, however, is misleading since the effect of waiting time is not considered. When estimated shrinkage of nuclei size and number is plotted on the same figure, using pure waiting results (i.e. Figure 4-4) an increase of nuclei size and number results. A 70 hour stilled sample of degassed water showed an increase in nuclei size and number for larger nucleus size for temperature increased from 70°F. to 130°F. Figure 5-3 shows the spectrum as a function of pulse height rather than nucleus diameter.

Cavitation also caused a large increase of nucleus size and number (Figure 4-9). This is partly due to the growth of gas bubbles in the crevices and elsewhere due to rectified diffusion. Also when large bubbles are broken up by cavitation, more and more nuclei are generated. It will not take very long to dissolve free air bubbles, so generated, but shrinkage of bubbles to the equilibrium state in the crevices obviously takes longer, since the effects of cavitation on nuclei spectrum persists at least 20 minutes, from these data.

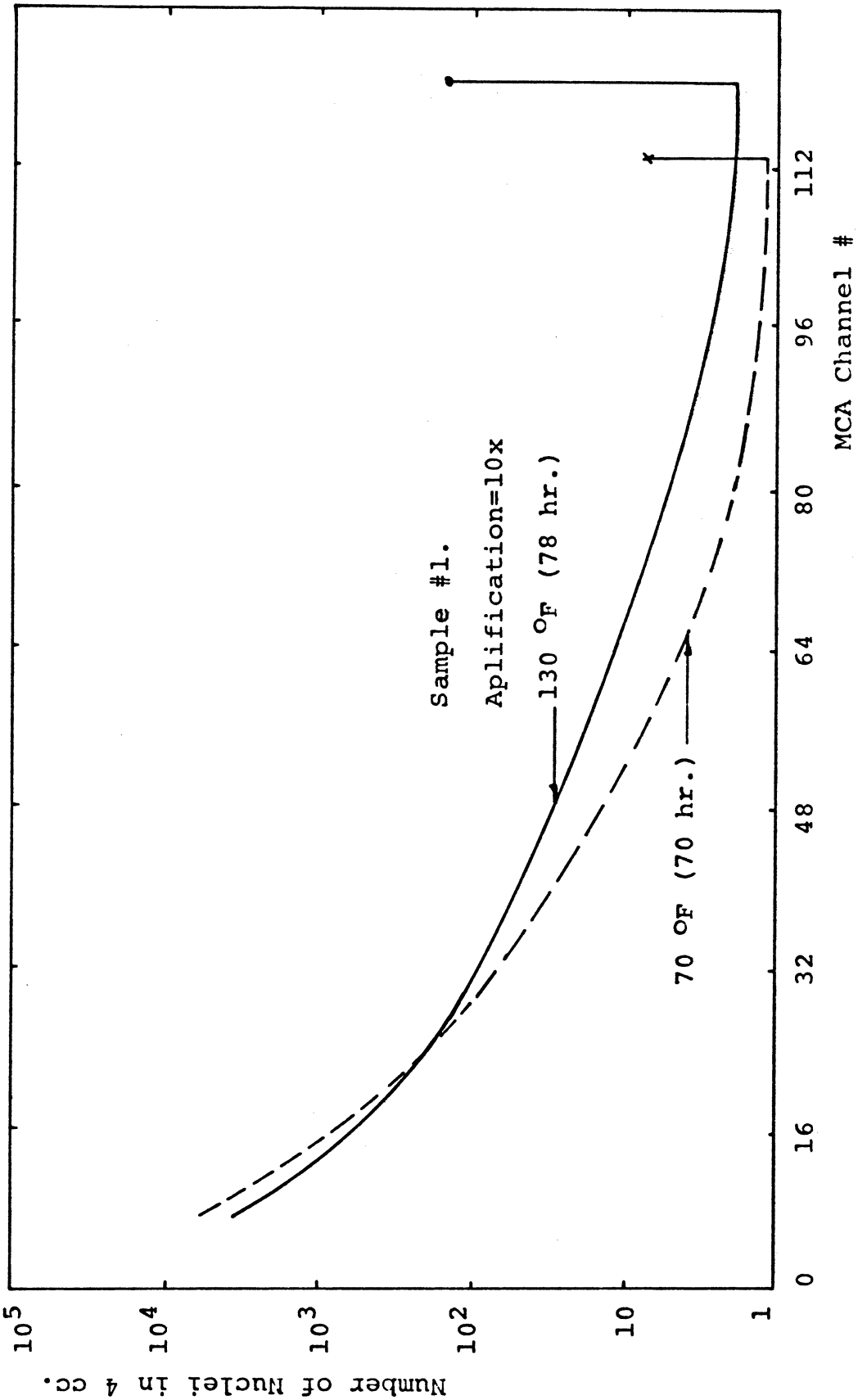

Figure 5-3 Degassed Tap Water at Two Different Temperatures after 70 Hours.

5074

Cavitation Inception Pressures

Effect of temperature

The effect of temperature increase is to decrease the inception pressure for nucleation. The variables which are influenced by temperature are vapor pressure P_v, surface tension σ, internal gas pressure P_g and contact angles, since they are all functions of surface tension and/or gas solubility. Contact angles are very important, since they directly affect the nucleation pressure as in equations C-6 and C-7. Since, when surface tension decreases, contact angles α_A increases and α_R decreases, the net result of all this is to decrease the cavitation threshold for gas entrapped in crevices as temperature increases. The maximum critical nucleus size (see Appendix C, Table C-1) for 0.77% of air saturation is 12.5 μm dia. This diameter is less than here measured by the light scattering method, using tap water. The critical nucleus size for 29% air saturated water is about 4μ. This size is also smaller than what was found in filtered tap water. Thus for all the samples in Figure 4-10 larger crevice theory will be applicable since measured nuclei are larger than calculated.

Neglecting dynamic effects, the pressure balance is

$$P_A = P_H - \gamma P_g - P_v + 2\sigma/R \qquad (5-1)$$

where

$$R = a/|\cos(\alpha_R - \beta)| \quad \text{for } \alpha_R > \beta$$

$$= a \qquad \alpha_R < \beta$$

for smaller than critical size crevices.

Since contact angles and crevice size are not known, the direct a priori evaluation of inception pressure is not possible. In order to test the theory, for each curve, the factor $\cos(\alpha_R - \beta)/a$ is solved using the measured threshold at $77^{\circ}F$. Equation (5-1) is then used to predict how the threshold would vary on the basis of the temperature dependence of P_v and P_g.

The crevice diameter, 2d, where the interface is located, does not change for most of the crevices during the temperature increase if $P_g \leq 1$ atm. In this case the only change due to rise in P_v and P_g will be on the radius of curvature. The value of γ in equation (5.1) does not affect inception values more than 10%. The higher the value of γ the lower the threshold. The value of γ will be larger for non-degassed water as compared to degassed, since the concentration gradient will be larger at the boundary of bubble and water.

Writing eq. (5-1) for two different temperatures

$$P_{A_1} = P_H - \gamma P_{g_1} - P_{v_1} + 2\sigma_1 \left| \frac{\cos(\alpha_R - \beta)}{a} \right|_1$$

$$P_{A_2} = P_H - \gamma P_{g_2} - P_{v_2} + 2\sigma_2 \left| \frac{\cos(\alpha_R - \beta)}{a} \right|_2$$

or

$$P_{A_2} = P_H - \gamma P_{g_2} - P_{v_2} + (P_{A_1} - P_H + \gamma P_{g_1} + P_{v_1})\left(\frac{\sigma_2}{\sigma_1} \frac{\left|\cos(\alpha_R - \beta)/a\right|_1}{\left|\cos(\alpha_R - \beta)/a\right|_2}\right) \qquad (5-2)$$

Since α_R and β does not change significantly with temperature and "a" is assumed to be constant

$$\frac{\left|\frac{\cos(\alpha_R-\beta)}{a}\right|_2}{\left|\frac{\cos(\alpha_R-\beta)}{a}\right|_1} \cong 1.0 \qquad (5-3)$$

An increase in temperature will cause the interface to move away from the apex (recede) due to the expansion of the gas in the crevice for some crevices.

The theoretical thresholds, using equation (5-2) and (5-3), are shown in Figure 4-10.

The theoretical analysis presented above will not be applicable for tap water with 77% air saturation, since water sample becomes super-saturated at about 100°F. Super-saturation will cause stabilization of nuclei in large and even non-conical crevices, so that cavitation inception pressures should drop drastically.

As temperature of the water increases, solubility of air in water decreases. This increase in saturation pressure will cause expansion of the bubbles. During the expansion, partial receding of interface may occur. Although not very realistic, let us assume that this receding occurs without any change in advancing contact angle (i.e. $\alpha = \alpha_A$). Receding will increase radius of crevice, a, at the interface. Then equation for larger crevice theory

$$P_A = P_H - \gamma P_g - P_v + (P_H - P_g - P_v) \times \frac{\cos(\alpha_R-\beta)}{\cos(\alpha_A-\beta)} \quad \alpha_R > \beta \qquad (5-4)$$

will be applicable.

Writing it in terms of a reference cavitation threshold pressure,

$$P_{A_2} = P_H - \gamma P_{g_2} - P_{v_2} + (P_H - P_{g_2} - P_{v_2}) \frac{P_{A_1} - P_H + \gamma P_{g_1} + P_{v_1}}{P_H - P_{g_1} - P_{v_1}} \tag{5-5}$$

No doubt eqn. (5-5) over-estimates the decrease of inception due to temperature increase because nucleation radius will be large compared to the previous case. Taking $77^{\circ}F$ inception pressures as reference, inception pressures found using equation (5-5) are also marked on Figure 4. 10 for $140^{\circ}F$.

Effect of Gas Content

Before analyzing the results, it may be helpful to understand the degassing process in the system. To start, assume that the tap water is over-saturated at room temperature. For equilibrium, the interface will then bow out and vice-versa for under-saturated. The radius of curvature, R, is determined by

$$P_g + P_v = P_H + \frac{2\sigma}{R} \tag{5-6}$$

The minimum radius of curvature is reached when either R = a, or the interface starts receding from the apex of the crevice. For smaller crevices than the critical size the interface is at the mouth of the crevice; for larger ones, it is below the mouth of the crevice. When a vacuum is applied for degassing, the interface will be pulled out of the crevices. The crevice, of course, will still be filled with air. When degassing is terminated, the air-water interface will either

remain at the mouth of the crevice, or advance with advancing contact angle until force equilibrium is achieved. The partial pressure of the air in the crevice may then either be smaller, larger, or equal to the partial air pressure in water depending on the contact angles and β.

For diffusion equilibrium, partial gas pressures must be the same inside and outside the cavity. Thus for large crevices with large α_A and large β, the interface may remain stationary, but the contact angle will decrease to increase radius of curvature of the interface during equilibrium.

For small crevices, which are larger than the critical size but did not nucleate during degassing and crevices with small α_A or small β the interface will advance with α_A and remain stationary. For crevices smaller than the critical size, the interface will not advance. It is obvious that a sample of water will nucleate easier, if it contains larger crevices. For a filtered water sample which does not have larger particles than critical size at the lowest air content, degassing should not effect very much on the nucleation pressures. Similar trend is seen in Figure 4-4 for filtered tap water.

Nucleation will occur when

$$P_A \geq P_H - \gamma P_g - P_v + 2\sigma/R \qquad (5-7)$$

where $R = |a_o/\cos(\alpha_R - \beta)| \qquad \alpha_R > \beta$

$= a_o \qquad \alpha_R \leq \beta$

a_o = the radius of the crevice at the crevice mouth.

Thus the only variable which affects the inception pressure is γ and P_g. γ is equal to the ratio of volumes before and after nucleation, if the gas diffusion is neglected. Assuming a value of 0.5 for γ and taking 0.4% gas content as a reference point, the calculated points are shown in Figure 4-14. The equation is

$$P_{A_2} = P_{A_1} - \gamma(P_{g_2} - P_{g_1}) \qquad (5\text{-}8)$$

which is derived using equation (5-7) and taking $\cos(\alpha_R - \beta)/a_o$ as constant.

For crevices which are larger than critical size as degassing continues the equilibrium interface gets closer and closer to the apex, decreasing radius of crevice at the interface. Thus more and more negative pressures are required to nucleate such a crevice. Tap water samples shown in Figure 4-14 has the same trend. In tap water most of the crevices are larger than critical size, thus inception pressure is given by Equation (5-4). Inception pressures P_A, predicted by Eqn. (5-4) taking inception pressure at 0.4% air content as reference are also shown in Figure 4-14. Experimental values differ considerably from the predicted values. This discrepancy may partially be due to crevices having large apex angles, and larger advancing contact angles. In this case, just after degassing the interface would advance further than it would have ordinarily if air content were reduced. Since advancing of interface will cause

reduction in interface radius when nucleation starts, inception thresholds will be larger than predicted by equation (5-4). When water is saturated

$$P_A \cong P_H - \gamma P_g - P_v, \qquad (5\text{-}9)$$

and bubble size becomes very large. In real cases, since there may not be too many very large nuclei, P_A will be larger than predicted by Eqn. (5-9) for finite rate of cavitation events.

Effect of Settling Time

The tap water sample used in the measurement of settling-time effect on cavitation inception pressure contained 1.65% air (.94% of saturation at the sample temperature of ~ 74°F.). As seen in Figure 4-4, the number of larger nuclei decreases as waiting time increases. However, change in particle spectrum does not necessarily imply any change in the crevice radius at the air-water interface. Consider two crevices in large and small particles with the same apex angle, 2β, and advancing and retarding contact angles. The only variable is then the size of the crevice, a_o, or the depth of crevice. For smaller crevices, the diameter of the crevice at the interface is smaller than for larger crevices. Thus when larger particles settle to the bottom, nucleation can come only from smaller crevices which are carried by smaller particles. Smaller diameter at the interface, thus, implies larger thresholds.

If we assume that crevice radius at the interface is proportional to the particle size, inception pressures, taking one of the inception

points as reference, can be calculated. Particle sizes (Figure 4-4) are 20 and 15μm at the beginning and at the end of the experiment respectively. Taking threshold at 1 pm as reference (Figure 4-17),

$$P_A = P_H - \gamma P_g - P_v + \frac{2\sigma}{a} \cos (\alpha_R - \beta)$$

Taking $\gamma = 0.5$ and $(\alpha_R - \beta) = cst$, one gets

$$P_A = 5.24 \text{ atm.}$$

at the end of the test period. The calculated and reference point is shown in Figure 4-17.

Effect of Addition of Particles

The experimental results are given in Table 4-7. It is expected that if nuclei larger than those already existing in the water are added the cavitation threshold will decrease. The resultant effective nuclei size will depend on the size and shape of the particles added. Wetting properties are also very important, since the radius of bubbles at cavitation inception will depend on contact angles.

The following conclusions can be reached by analyzing the data in Table 4-7:

(a) The larger the particle size, the smaller the inception threshold. The largest particles used were ~ 30 μm (Crystolon 400B*). About 23% decrease in threshold was

*Crystolon abrasive is produced from a mixture of silica sand, petroleum coke, sawdust and salt packed around a graphite core in a resistance-type furnace. A heavy electric current is passed through the core producing temperatures as high as 4500°F. At these temperatures, crystals of silican carbide form from the sand and coke.

observed when these are added.

(b) Use of 2 drops of wetting agent (Tween-80) increases the threshold more than 25%, due presumably to its effect on contact angles.

(c) Addition of paper mulberry pollen increases threshold ~ 30%. This increase, however, is attributed to the wetting agent (Tween 80) which is used to prepare the solution of Paper Mulberry pollen.

(d) No threshold decrease is found when small particle size of latex (5.02 μm) are used. Measured threshold drop is ~ 16% for 6-14μm diameter latex. This drop increased when more particles were added.

(e) No or small threshold increase is observed when Alundum 600 is added to the filtered and degassed water. The result implies that these particles are well enough wetted so that crevices larger than those already existing do not occur.

(f) Referring to sample 3, addition of Paper Mulberry pollen particles, plus "Tween 80" (used as a wetting agent) increased threshold ~ 29%. Addition of one drop of 6-14 μm latex decreased the threshold to a value which is lower than the original nucleation pressure for the water sample itself. The result indicates that all or most of the wetting agent, which was with the 14-18 μm pollen particles, has been deactivated (i.e., utilized) by the particles, which

existed in the water sample prior to the addition of the latex particles.

(g) Graphite ($\leq$ 20 μm) seems to be less effective than latex (6-14 μm) in affecting the threshold. Since graphite is considered to be hydrophobic, the advancing contact angle is small for the water-air interface, which implies that the radius of the crevice in the interface must be smaller at equilibrium compared to a crevice with larger advancing angle. Also, it may be that the graphite had smaller crevices than a spherical latex particle.

Effect of Polymer Addition

The effect of polymers on drag reduction in water is well known. A good review is given by Hoyt [94, 96] for example. Recently, studies on the effect of polymer additives on cavitation have also been made. Meulen [95] found > 30% reduction of desinent cavitation number in tunnel cavitation studies using 500 ppm Polyox WSR-301 and a stainless steel cavitating body. He found also that cavitation on a teflon-nosed body was hardly affected by polymer addition.

Two experiments were here conducted to see the effect of polymer (Separan AP30) on threshold. In degassed tap water, addition of 0.25 ppm polymer increased cavitation threshold ~ 21%. For slightly degassed tap water (0.9% air) the effect of the same amount of polymer was zero, and 1 ppm increased threshold only ~ 6%. The decrease in threshold increase may also be attributed to the degradation of the

polymer by time, since fresh polymer solution was not prepared for the slightly degassed tap water test.

No effect of polymer addition on nuclei spectrum was found.

Effect of Neutron Irradiation

Two different samples of water were used to measure the effect of fast neutron irradiation. Sample #1 was degassed (0.61% air) tap water. Waiting time for the water sample before experiments were conducted was about 50 hours. The nuclei spectra for sample #1 is given in Figure 5-3 for 70°F and 138°F. Sample #2 was filtered (2μm) and degassed (0.35% air) tap water. Threshold for the second sample was expected to be higher than for the first, since the second was filtered. The first sample had larger inception pressure, since (a) it was aged water, (b) particle content was less than sample #2, even though it was not filtered. Obviously filtering was not very effective for sample #2, since the tap water sample happened to have more particles on that particular day than usual. Nuclei spectrum for filtered-degassed tap water (i.e. sample #2) is given in Figure 5-4.

If only energy deposition from impacted oxygen nuclei is considered, the experimental results cannot be verified, since oxygen knock-on atoms can only create about 0.2 μm diameter nuclei. The tension required to expand a 0.2 μm dia. nucleus about 15 bars at room temperature (~ 70° F.). Total nuclei count measurements, however, prove that there is an increase in nuclei count when the

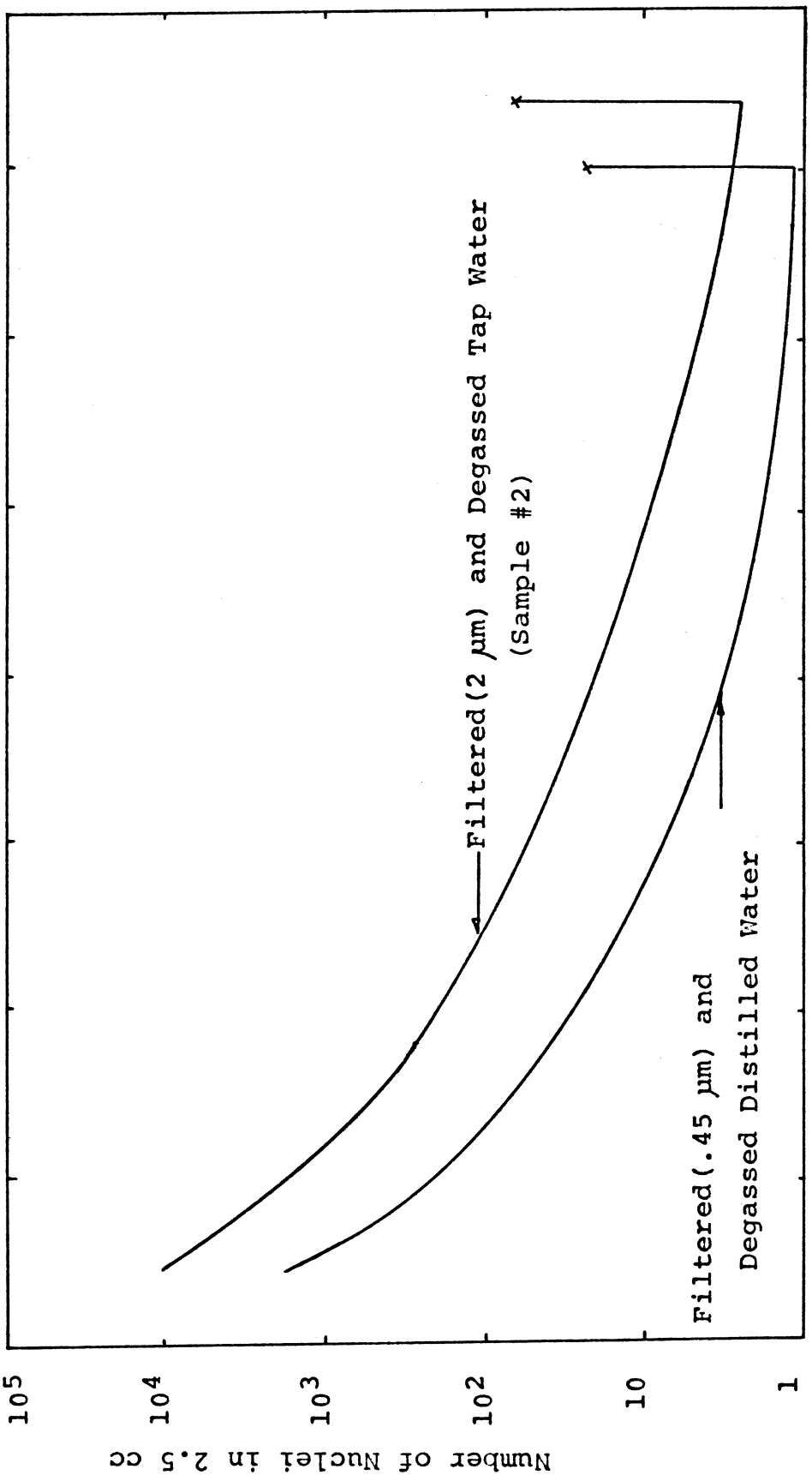

Figure 5-4 Nucleus Pulse Height Spectrum for Tap and Distilled Water at 70 $^{o}_{F}$

5075

neutron source is placed near the sample. The results, if an 0-2% increase in nuclei count can be considered dependable, prove that the following are possibilities for the creation of larger nuclei:

(a) A mechanism to combine together many ~ 0.2 μm diameter nuclei must exist;

(b) Nuclei larger than 4 μm are created directly; or

(c) Existing small nuclei size is increased by the radiation.

Substantial large scale recombination to create > 4 μm diameter is not to be expected since the probability of creation of many bubbles at the same position in water is low. Direct creation of 4 μm bubbles, however, is also not expected, since the total deposition of the 10 Mev neutron energy would create only 0.1 μm radius vapor bubble. Thus the only possibility remaining is the creation of vapor bubbles on the particle surfaces or near the water-air interface in a crevice. If such a vapor bubble is created near the interface, it will combine with the gas bubble and expand it. This expansion may be appreciable, since the pressure in a gas bubble is only about gas saturation pressure in the liquid. The pressure inside an 0.1 μm radius bubble is ~ 15 atm. Thus, if expansion of such a bubble into a crevice at one atmosphere is assumed the original volume of 0.1 μm radius bubble will increase ~ 15-fold. Similarly, a bubble created near to a particle surface may stick to the surface, and expand onto non-wetting surfaces, since the radius of curvature will decrease as illustrated in Figure 5-5.

The effect of temperature on threshold, with and without source, is given in Figure 4-18. Taking the 70°F inception pressure as a

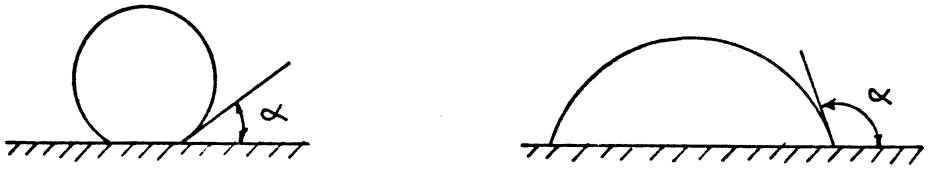

(a) (b)

Figure 5-5 Bubble on a Wetting (a), and a Non-Wetting (b) Surface.

5076

reference, an energy deposition rate of ~ 1.32 Mev/μm is obtained from equation (2-24). Assuming the energy deposition rate is constant the cavitation threshold is calculated at 140°F, using the same equation for σ and h_{fg} at 140°F (i.e., σ = 66 dynes/cm, h_{fg} = 1013 Btu/lb). The radius of bubbles created will increase from 0.25 μm at 70°F to 0.31 μm at 140°F. Equation

$$P_A = P_H + \frac{2\sigma}{R}$$

is used to evaluate the radius for the reference point at 70°F and threshold at 140°F. The calculated point is also shown in Figure 4-18. The calculated value is fairly close to the measured cavitation threshold pressure.

No appreciable induction or decay time was found for the effect of fast neutron source on cavitation threshold, and nuclei count for nuclei diameter $\geq$ 4 μm. Sette, et al. [76] and Finch [78] found a cumulative effect. Many minutes or even an hour of exposure to neutrons was required to "weaken" the water and the "strength" returned after a similar interval, after the exposure was terminated. Greenspan [79] has found no induction or decay time for the effect.

Finch [78] observed about a 30% decrease on cavitation threshold when neutrons are used. His neutron flux of 10^8 neutrons/sec and energy of 14 Mev mono energetic neutrons from Picker-Dresser neutron generator was larger than used in these experiments. A maximum of ~ 6% decrease of threshold was found for degassed (0.6% air) and calmed (52 hrs.) tap water. Pyun [14] in this laboratory observed only

~ 0.8% decrease of threshold for tap water with 1.53% air content. His source, however, was located farther from the nucleation vessel (~ 6.5 cm). The distance between the centerline of the horn tip and the neutron source was less than 2.5 cm, thus providing a neutron flux at the test section ~ 7x that for the results presented by Pyun [14].

CHAPTER VI

SUMMARY AND CONCLUSIONS

Summary

Two methods of nucleus spectrum measuring devices were evaluated. One is the Coulter counter technique, following in general methods developed here by Ahmed [13] and Pyun [14], whose principle of the nucleus size measurement is based on the electrical resistivity of nuclei and electrolyte. The second method was the light scattering method, following particularly the apparatus of Keller [17] whose principle of measurement of nucleus size depends on the light scattering properties of the nuclei. Neither of these methods is able to distinguish between solid particles and bubbles, but, using these methods, satisfactory information was obtained on the nucleus spectrum.

The light scattering method was found to be the more reliable nucleus spectrum measuring device for any kind of water. However, its range of applicability is limited by the concentration of the nuclei in the water sample, which cannot be too great. Coincidence and boundary errors must be minimized if water samples contain too many nuclei to minimize errors on the spectrum. Free gas bubbles can be measured very accurately, since direct calibration with free bubbles can be used relatively easily.

The Coulter counter technique was found to be limited by the conductivities of the nuclei. For proper operation of the system, resistivities of nuclei should be very large compared to that of the

"electrolyte," i.e. the test liquid. In agitated water, as in a typical water tunnel, most of the nuclei are bubbles, and this method gives relatively accurate results. In relatively quiescent water (as in the present tests), particles dominate the bubbles, and this method is useless unless the electrical conductivity of the liquid is increased. Addition of ~ 0.1% salt will accomplish this objective so that the Coulter results become relatively accurate.

Nucleus spectrum, both number and size, was found to:

1) increase when solid particles were added;

2) decrease when degassed;

3) decrease by settling time;

4) remain practically unchanged when under magnetic field or neutron irradiation or when wetting agent or polymer is added. And, finally,

5) an increase on the total nuclei count for $\geq$ 4 μm nucleus diameter is found when under neutron irradiation.

Inception pressures for cavitation (threshold) were measured in tap, filtered tap, and degassed tap water using the acoustic cavitation apparatus developed in this laboratory [81]. The variables for the water samples were temperature, nucleus spectrum, settling time, fast neutron irradiation, imposed magnetic field, and total gas content. Frequency of the sonic horn was kept constant at 14 KHz. The inception of cavitation was detected using an optical system consisting of a laser, and a photo cell from which laser light was cut off

when a bubble was present. Inception pressures were measured by a calibrated piezoelectric crystal which was attached to the top of the horn assembly. This system was calibrated by direct measurements as previously explained. Spectrum were measured for the most part using the light scattering method. Hydrostatic pressure was 1 atm. in all measurements.

The nuclei content of the water was varied by filtering and addition of particles, and also by degassing. Temperature of the water was varied from 70°F to 140°F in ~ 20°F intervals. Inception pressures as a function of temperature were measured for two samples of tap water with different air content, and when one of the samples was degassed at 140°F. Inception pressures for cavitation were also measured for a filtered (2 μm pore size) and fully degassed (0.51% air) sample of tap water. The effect of 1 curie Pu-Be fast neutron source was also investigated as a function of temperature.

The inception pressures (thresholds) for cavitation exhibit the following trends:

1) increased when sample nuclei content size and number decrease;
2) increased when water is degassed;
3) decreased when particles were added;
4) increased when a wetting agent or polymer was added;
5) decreased when the water sample was kept under fast neutron irradiation;

6) increased when waiting (settling) time was increased;

7) unchanged when water was under 5.9 K Gauss magnetic field.

A theoretical analysis was made to predict behavior of threshold pressure under some of the variables presented above, using measured nucleation pressure as reference to calculate some of the unknown factors in the crevice theory. This theory predicted the threshold pressures quite closely in most cases.

Conclusions

In general, we have found the light scattering method more advantageous than the Coulter technique. Nucleus spectra obtained using the Coulter counter with salt addition (0.1-0.2% by mass) approach the spectra obtained by the light scattering method. The total nuclei count (above 5 μm diameter) obtained by Coulter counter was ~ 60% of that obtained using the light scattering method for 0.1-0.2% salty water, but only ~ 20% for tap water without salt addition. Total nuclei count percentages for larger diameters were less.

Cavitation inception threshold was ~ 0.0 bar-abs. for water samples saturated and over-saturated with air. Thresholds were 2-6 bar (depending on the factors mentioned in the Summary) for gas-undersaturated water. Thus cavitation thresholds depend not only on the quality of the water in terms of nuclei content and its temperature, but also on the external effects, such as neutron (or cosmic ray) irradiation.

APPENDIX A

EFFECT OF ELECTROLYTE AND PARTICLE RESISTIVITIES ON COULTER COUNTER RESULTS

The exact resistance change due to a particle in the orifice is given in Chapter II:

$$\Delta R = 2\pi\left(1 - \frac{\rho_o}{\rho_p}\right)\frac{\rho_o}{A^2}\int_0^R dx\left[\frac{R^2 - x^2}{1 - 4\left(1 - \frac{\rho_o}{\rho_p}\right)\frac{R^2 x^2}{d^2}}\right] \tag{A-1}$$

Setting $Q \equiv 4(1 - \rho_o/\rho_p)$ and $S \equiv \frac{d^2}{Q} - R^2$ and integrating,

$$\Delta R_1 = \frac{2\rho_o}{A}\left[\tan^{-1}\frac{R}{S}\left(\frac{R^2}{S} + S\right) - R\right] \tag{A-2}$$

If $\rho_o \ll \rho_p$, $Q \cong 4$ and $S \cong b \equiv \frac{d}{2}$, since

$$\tan^{-1}\frac{R}{b} \cong \frac{R}{b} - \frac{R^3}{3b^2} \quad \text{for} \quad \frac{R}{b} \ll 1$$

$$\Delta R_2 \cong \frac{\rho_o}{A^2}\left(\frac{4}{3}\pi R^3\right) \tag{A-3}$$

For tap water, $\rho_o \cong 3800\ \Omega\text{-cm}$,

$$d = 70\ \mu m = 7 \times 10^{-3}\ cm \Longrightarrow A = 3.84 \times 10^{-5}\ cm^2$$

For the above values, Eqs. (A-2) and (A-3) become

$$\Delta R_1 = 1.98 \times 10^8\left[\tan^{-1}\frac{R}{S}\left(\frac{R^2}{S} + S\right) - R\right]\Omega \tag{A-4}$$

$$\Delta R_2 \cong 1.09 \times 10^{13} R^3 \Omega \qquad \text{(A-5)}$$

The relative error $\frac{\Delta R_2 - \Delta R_1}{\Delta R_2}$ is plotted in Figure A-1 as a function of ρ_o/ρ_p to see the effect of resistivity ratios.

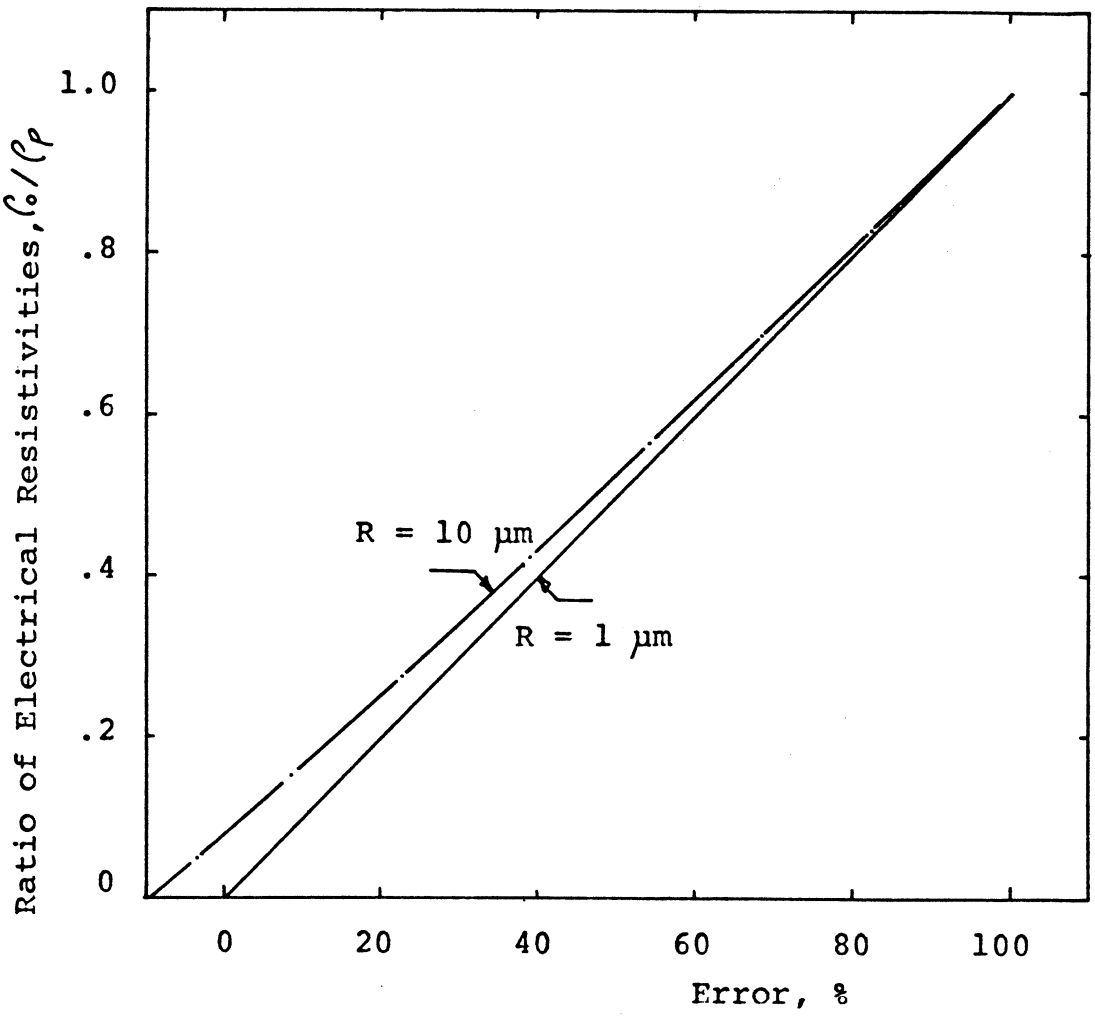

Figure A-1 Percent Error as a Function of ρ_o/ρ_ρ and Radius of Nuclei.

5077

APPENDIX B

ACOUSTIC WAVE ATTENUATION METHOD TO MEASURE NUCLEUS SPECTRUM [21, 22]

The resonance frequency of bubbles of uniform size can be calculated assuming a spring mass, and dissipation system [21]. The presence of free gas in the form of bubbles produces significant changes in propagation characteristics. By comparison, small solid particles in the water have a negligible effect on acoustic characteristics of the liquids. Not only do gas pockets produce a degree of "softness", but the bubble executes a resonant oscillation which greatly increases effects at certain frequencies.

A bubble, being a two-phase system of a gas pocket in direct contact with a liquid, forms an oscillator of the zero order. The displaced liquid forms the mass of the resonant system and the gas pocket, the spring. The equation of motion for such a spring-mass system is given by

$$\frac{\partial^2 v}{\partial t^2} + B\frac{\partial v}{\partial t} + Kv = -p \exp(i\omega t) \qquad \text{(B-1)}$$

where m, B and K are effective mass of the displaced water, dissipation, and stiffness of the gas pocket, respectively. v is the incremental change in the bubble volume, and p exp (i ωt) is the applied pressure.

The solution of the differential equation (B-1) is

$$v = \frac{-p \exp(i\omega t)}{\omega^2 m[(\frac{K}{\omega^2 m} - 1) + i\frac{B}{\omega m}]} \qquad (B-2)$$

The incremental compressibility due to N bubbles becomes,

$$\eta_b = \frac{-vN}{p \exp(i\omega t)} = \frac{N}{\omega^2 m[(\frac{\omega_0^2}{\omega^2} - 1) + i\frac{B}{\omega m}]} \qquad (B-3)$$

where ω_o is the resonant frequency of the bubble system.

The effective mass, stiffness and dissipation can be derived as,

$$m = \rho/4\pi R$$

$$K = 3\gamma P_i/4\pi a^3$$

$$B = \omega_o m\delta$$

where

ρ = density of water

R = bubble radius

γ = ratio of specific heats of gas

p_i = internal pressure of the bubble

δ = damping coefficient.

For adiabatic compression $\gamma \cong 1.4$, and for isothermal compression $\gamma = 1$.

The resonance frequency is

$$f_o = \frac{\omega_o}{2\pi} = \frac{1}{2\pi}\sqrt{\frac{K}{m}} = \frac{1}{2\pi R}\sqrt{\frac{3\gamma P_i}{\rho}} \qquad (B-4)$$

For bubbles larger than 10 μm diameter, compression is adiabatic, and for 10 μm and less, compression is isothermal [21].

P_i in this case should also include pressure due to surface tension.

$$P_i = P_H + \frac{2\sigma}{R}$$

where P_H is the hydrostatic pressure. Thus, in general,

$$f_o = \frac{1}{2\pi R} \sqrt{\frac{3\gamma}{\rho} (P_H + \frac{2\sigma}{R})} \qquad \text{(B-5)}$$

For bubble-free water, the complex compressibility constant is

$$\eta_o = \eta_{or} + i\,\eta_{oi} .$$

The velocity of propagation is the real part of the propagation constant,

$$c_o = \text{Re}\ \frac{1}{\sqrt{\rho \eta_o}} = \text{Re}\ \frac{1}{\sqrt{\rho \eta_{or}}} \left(1 - i \frac{\eta_{oi}}{2\eta_{or}} + \ldots\right)$$

$$\cong \frac{1}{\sqrt{\rho \eta_{or}}} \qquad \text{(B-6)}$$

The higher order terms in the binomial expansion being ignored, since the reactive term of compressibility is very small compared to the real terms.

Attenuation, similarly, is expressed in terms of the imaginary part of the inverse propagation constant,

$$\alpha = 8.68\ \omega\ \text{Im}\ \sqrt{\rho \eta_o} = 8.68\ \omega\ \text{Im}\ \sqrt{\rho \eta_{or}} \left(1 + i \frac{\eta_{oi}}{2\eta_{or}} + \ldots\right)$$

$$\cong 8.68 \frac{\omega}{C_o} \frac{\eta_{oi}}{2\eta_{or}} \qquad \text{(B-7)}$$

The relation between volume V and total number of bubbles is

$$\frac{4}{3}\pi R^3 N = V \tag{B-8}$$

Inserting Equation (B-8) into Equation (B-3), one gets

$$\eta_b = \frac{3V}{4\pi^2 \rho (f_o R)^2} \frac{(1-z^2) - i\,\delta z}{(1-z^2)^2 + (\delta z)^2} \tag{B-9}$$

where $z = \omega/\omega_o$.

Thus attenuation and sound speed in water with bubbles will be

$$c = c_o \left[1 - \frac{3\,c_o^2}{8\pi^2 (f_o R)^2} V \frac{(1 - z^2)}{(1-z^2)^2 + (\delta z)^2}\right] \tag{B-10}$$

and

$$\alpha = 8.68\pi \frac{f_o}{c_o} \frac{\eta_{oi}}{\eta_{or}} + \frac{3\times 8.68}{4\pi} \frac{c_o}{(f_o R)^2} V \frac{f_o \delta z^2}{(1-z^2)^2 + (\delta z)^2} \tag{B-11}$$

where the first term in each case is that of water itself, and the second term is the perturbation produced by bubbles.

The attenuation $f_o\,\delta \int \frac{z^2\,dz}{(1-z^2)^2 + \delta^2 z^2}$ for a uniformly distributed bubble population between $z = 1/2$ and $z = 3/2$ is approximately a linear function of frequency, and is equal to $1.4\,f_o$. For this circumstance, the attenuation perturbation equation (B-11) can be written as:

$$\alpha = 8.68\pi \frac{f_o}{c_o} \frac{\eta_{oi}}{\eta_{or}} + 4.03 \times 10^2 V f_o \tag{B-12}$$

The ratio between received amplitudes under test conditions with bubbles present, and under test conditions with bubbles absent is a measure of the attenuation which is, in fact, due mostly to the resonant and near resonant bubbles. The total volume concentration range within which the technique could be useful is that between 0.033 ppm and 1 ppm by mass, which correspond respectively, to 10^5 and 3×10^6 nuclei per second through the test control volume. Attempts to measure concentrations outside this concentration range results in attenuations either too small to be observed, or so large that the signal is nearly completely obliterated [22].

APPENDIX C

STABILIZATION OF NUCLEI BY CONICAL CREVICES

Consider a conical, imperfectly-wetted crevice with apex angle 2β (Figure 2-7) with an air cavity up to its apex. The air-water interface has a contact angle α with the conical surface. If contact angle exceeds a critical value α_A, the interface advances in the direction of the apex; whereas for contact angle $\leq \alpha_R$, the interface recedes from the apex. The stabilizing action of the crevice occurs [25] when

$$\alpha_A > \beta + \frac{\pi}{2} > \alpha_R$$

Let us consider a situation where the pressure inside the cavity is larger than the saturation pressure of gas, in water. Air inside the cavity will diffuse out until the surface becomes so concave that partial pressure inside the cavity and in the water are equal. Then

$$P_H = (P_g + P_v) + \frac{2\sigma}{R} \qquad (C-1)$$

will be satisfied.

When the liquid is degassed sufficiently, the contact angle will reach a limiting value α_A. When this condition is reached, additional diffusion of air causes the surface to creep toward the crevice apex. Radius of curvature of the interface continues decreasing until equation (C-1) is satisfied. For such a crevice geometry, the position of the interface is given by:

$$a = R|\cos(\alpha_A-\beta)| = 2\sigma|\cos(\alpha_A-\beta)|/[P_H-(P_g+P_v)] = a_c \qquad (C-2)$$

A crevice which has half the diameter at the mouth of that given by equation (C-2) is called a critical crevice [25]. For a crevice smaller than this critical size, the contact angle will always be smaller than α_A. Thus, for a smaller crevice

$$a_o = R|\cos(\alpha-\beta)| \qquad \alpha < \alpha_A \qquad (C-3)$$

The qualitative difference between large and smaller crevices is that the advancing interface remains at the mouth of the crevice for small crevices.

Any increase in water pressure pushes the interface towards the crevice apex maintaining the constant angle at α_A. Any decrease, however, does not cause the interface to move away from the apex; instead the radius of curvature of the surface is adjusted to the pressure. When the liquid pressure is reduced enough to cause the receding contact angle to be reached, or the interface become hemispherical (whichever happens first), the interface does recede from the apex of the crevice. A vapor cavity is said to be nucleated at this pressure.

For larger crevices, this condition is given by

$$P_L = \gamma_1 P_g + P_v - \frac{2\sigma}{R'} \qquad (C-4)$$

where

R' = radius of curvature of the interface for the larger crevice

as shown in Figure 2-8 just before nucleation,

γ_1 = a constant less than or equal to 1, reflecting the fact that the gas partial pressure in the crevice decreases from the equilibrium value if the diffusion process cannot keep pace with the rapid outward motion of an acoustically stressed interface.

P_L = pressure in the liquid

$$\begin{aligned} a &= R' \left| \cos(\alpha_R - \beta) \right|, && \alpha_R > \beta \\ &= R' && \alpha_R \leq \beta \end{aligned} \qquad \text{(C-5)}$$

Using equations (C-4), (C-5) and (C-2), one gets

$$P_H - P_A = P_L = \gamma_1 P_g + P_v - (P_H - P_g - P_v) \times \left| \frac{\cos(\alpha_R - \beta)}{\cos(\alpha_A - \beta)} \right|, \quad \alpha_R > \beta \qquad \text{(C-6)}$$

$$= \gamma_1 P_g + P_v - (P_H - P_g - P_v) / \left| \cos(\alpha_A - \beta) \right|, \quad \alpha_R < \beta$$

and for the smaller crevice

$$\begin{aligned} P_L &= \gamma_1 P_g + P_v - 2\sigma \left| \cos(\alpha_R - \beta) \right| / a_o && \alpha_R > \beta \\ &= \gamma_1 P_g + P_v - (2\sigma / a_o) && \alpha_R \leq \beta \end{aligned} \qquad \text{(C-7)}$$

where a_o is the radius of the mouth of the smaller crevice.

Consider a crevice with apex angle $2\beta = 100^o$ that is imperfectly wet by water. If we assume that water does not completely wet the mote, then a reasonable estimate of the advancing constant angle might be $\alpha_A = 150$. The equation (C-2) gives

$$a_c = \frac{2 \times 72}{(P_H - P_g - P_v) \times 10^6} \left| \cos (100^\circ) \right| ,$$

for P_H = 1 bar and

P_v = .4 psi $\cong$ 0.027 bar (at T $\cong$ 74°F)

$$a_c \cong \frac{1.44 \times 0.174 \times 10^{-4}}{(.97 - P_g)} \cong \frac{0.25 \times 10^{-4}}{.97 - P_g} \text{ cm}$$

TABLE C-1

CRITICAL CREVICE RADIUS AS A FUNCTION

OF EQUILIBRIUM GAS PRESSURE

P_g Fraction of Saturation	Crevice Radius, μm	Particle Diameter, μm
0.0	0.258	2.58
0.2	0.325	3.25
0.4	0.44	4.4
0.5	0.53	5.3
0.6	0.675	6.7
0.7	0.925	9.25
0.8	1.47	14.7
0.9	2.78	27.8
0.97	∞	∞

5078

Assuming that the crevice radius is 0.1x that of particle diameter, the critical particle diameter can be calculated. Results are summarized in Table C-1.

For crevices larger than critical the effect of gas content depends on the magnitude of $\left| \cos (\alpha_R - \beta) / \cos (\alpha_A - \beta) \right|$, which can be very large if α_A is near $(\beta + \pi/2)$, (i.e., if the liquid poorly wets the crevice.

Thus if particles are larger than the critical particle, equation (C-6) will be valid. For a system with particles smaller than critical, equation (C-7) will be valid.

APPENDIX D

NUMERICAL SOLUTION OF BUBBLE DYNAMICS AND GAS DIFFUSION EQUATIONS

The equation

$$\rho R\ddot{R} + \frac{3}{2}\rho \dot{R}^2 = P_A \sin \omega t - P_H + P_v + P_g(t)\left(\frac{R_o}{R}\right)^3 - \frac{2\sigma}{R} - 4\eta \dot{R}/R \tag{D-1}$$

and

$$\frac{\partial C}{\partial t} + V \frac{\partial C}{\partial r} = D\left(\frac{\partial^2 C}{\partial r^2} + \frac{2}{r}\frac{\partial C}{\partial r}\right) \tag{D-2}$$

where

$$V = \dot{R}R^2/r^2$$

will be solved numerically using the fourth-order Runga-Kutta method for equation (D-1) and the DuFort-Frankel method for equation (D-2), where $\dot{R}$ and $\ddot{R}$ are first and second derivatives of radius with respect to time.

At a given time, the diffusion equation will be solved numerically. The values of R(t) will be obtained, solving equation (D-1), using the fourth order Runga-Kutta method. After R(t) is obtained, the distribution of concentration of air will be calculated using equation (D-2).

The concentration of air inside the bubble will be calculated using Henry's Law, which states that the concentration of gas is proportional to gas partial pressure in the liquid. Concentration distribution inside the bubble will be assumed to be uniform. Boundary and initial conditions thus are:

$$C(r, 0) = C_i \qquad r \geq R$$

$$\lim_{r \to \infty} C(r, t) = C_i$$

$$C(R, t) = C_s \qquad t > 0$$

where C_i is the initial uniform concentration of gas in the liquid at infinity, C_s is the concentration of the gas in the liquid at the bubble wall.

The diffusion equation can be written in numerical form as

$$C_{i+1, n+2}\left(1 + \frac{2D\Delta t}{\Delta r^2}\right) = C_{i+1, n}\left(1 - \frac{2D\Delta t}{\Delta r^2}\right)$$

$$- C_{i+2, n+1}\left[\frac{\Delta t}{\Delta r}\left(V - \frac{2D}{i\Delta r} - \frac{2D}{\Delta r}\right)\right]$$

$$+ C_{i, n+1}\left[\frac{\Delta t}{\Delta r}\left(V - \frac{2D}{i\Delta r} + \frac{2D}{\Delta r}\right)\right] \qquad \text{(D-3)}$$

where

$$t = (n-1)\Delta t \qquad n \geq 1$$

and

$$r = (i-1)\Delta r \qquad i \geq 1$$

The boundary and initial conditions are:

$$C(R, n\Delta t) = C_s = \frac{C_i}{P_{g_o}} P_g(t)\left(\frac{R_o}{R(t)}\right)^3 \cdot \gamma_v^2 \qquad t > 0$$

$$C(\infty, n\Delta t) = C_i$$

$$C(i\Delta r, 0) = C_i \qquad i\Delta r \geq R$$

where

P_{g_o} = partial pressure of the gas at equilibrium;

$P_g(t)$ = partial pressure of the gas at time t if R(t) is reduced to R, the original radius of bubble before it starts expanding.

γ_v = ratio of bubble volume under equilibrium in the crevice to the volume of bubble when $R(t) = R_o$;

= 1 for bubbles which are stabilized by other means.

The Fortran IV computer program listing is given in Appendix F.

APPENDIX E

CIRCUIT DIAGRAMS

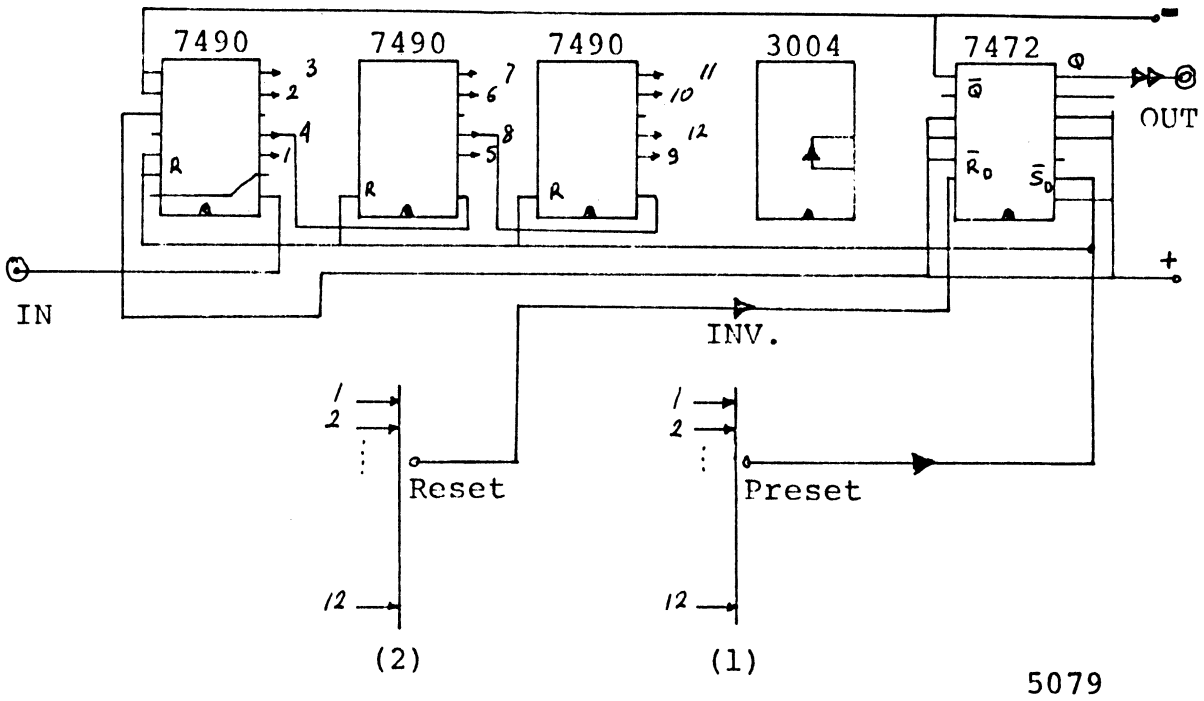

Figure E-1 Circuit Diagram of the Frequency Divider-Pulse Generator.

SN7490 is a decade counter, C3004 is a hex inverter, and SN7472 is a JK-M/S flip-flop. The position of rotary switch (1) determines how many times the input frequency will be devided. Rotary switch (2) will adjust the duration of the pulse.

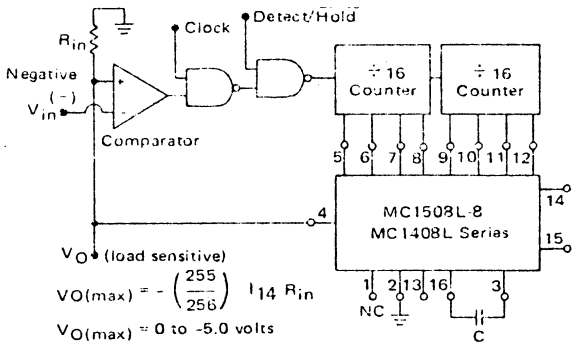

Figure E-2 Negative Peak Detecting Sample and Hold.

5080

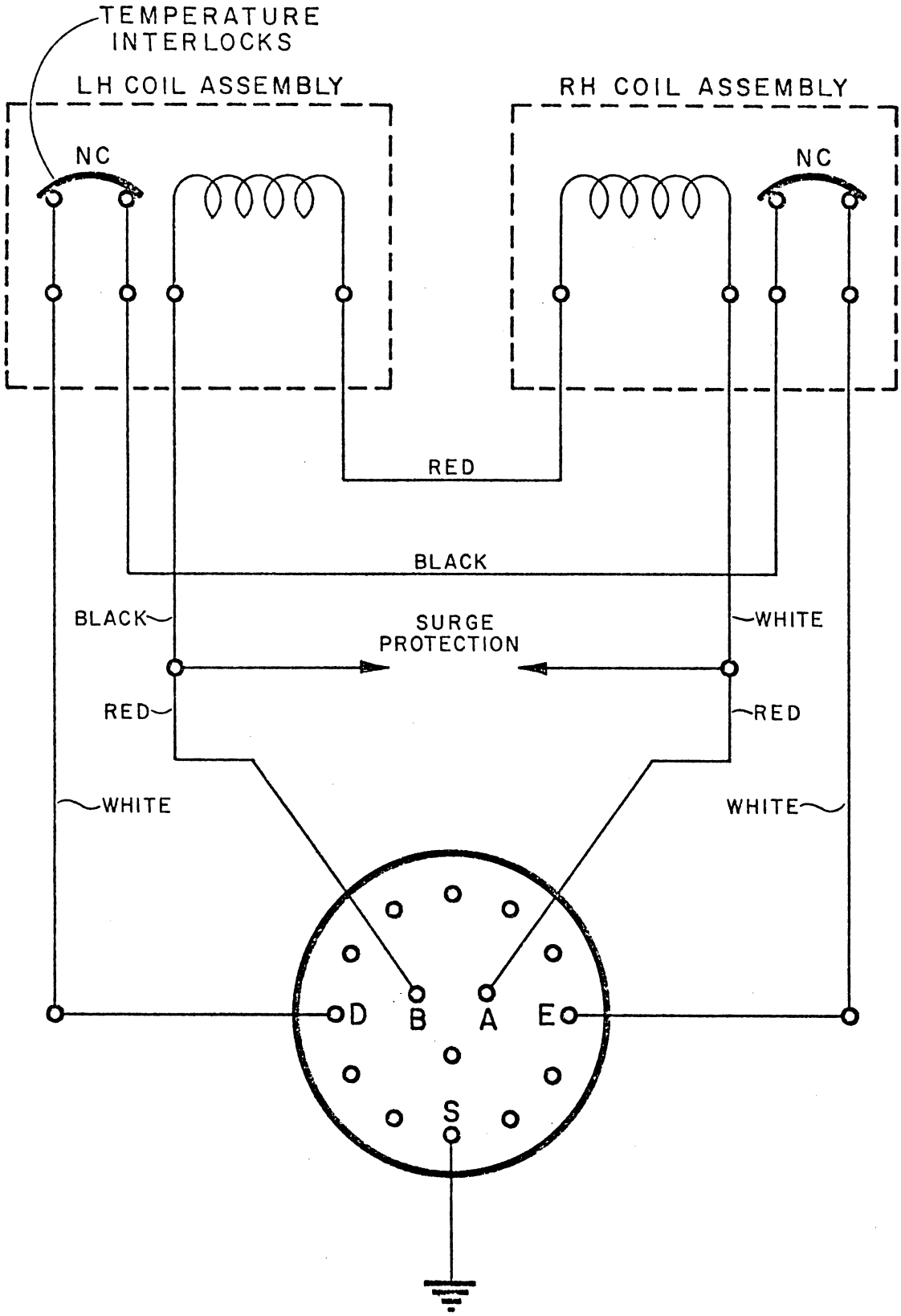

Figure E-3 Schematic for V-4007 Rotating Magnet.

5081

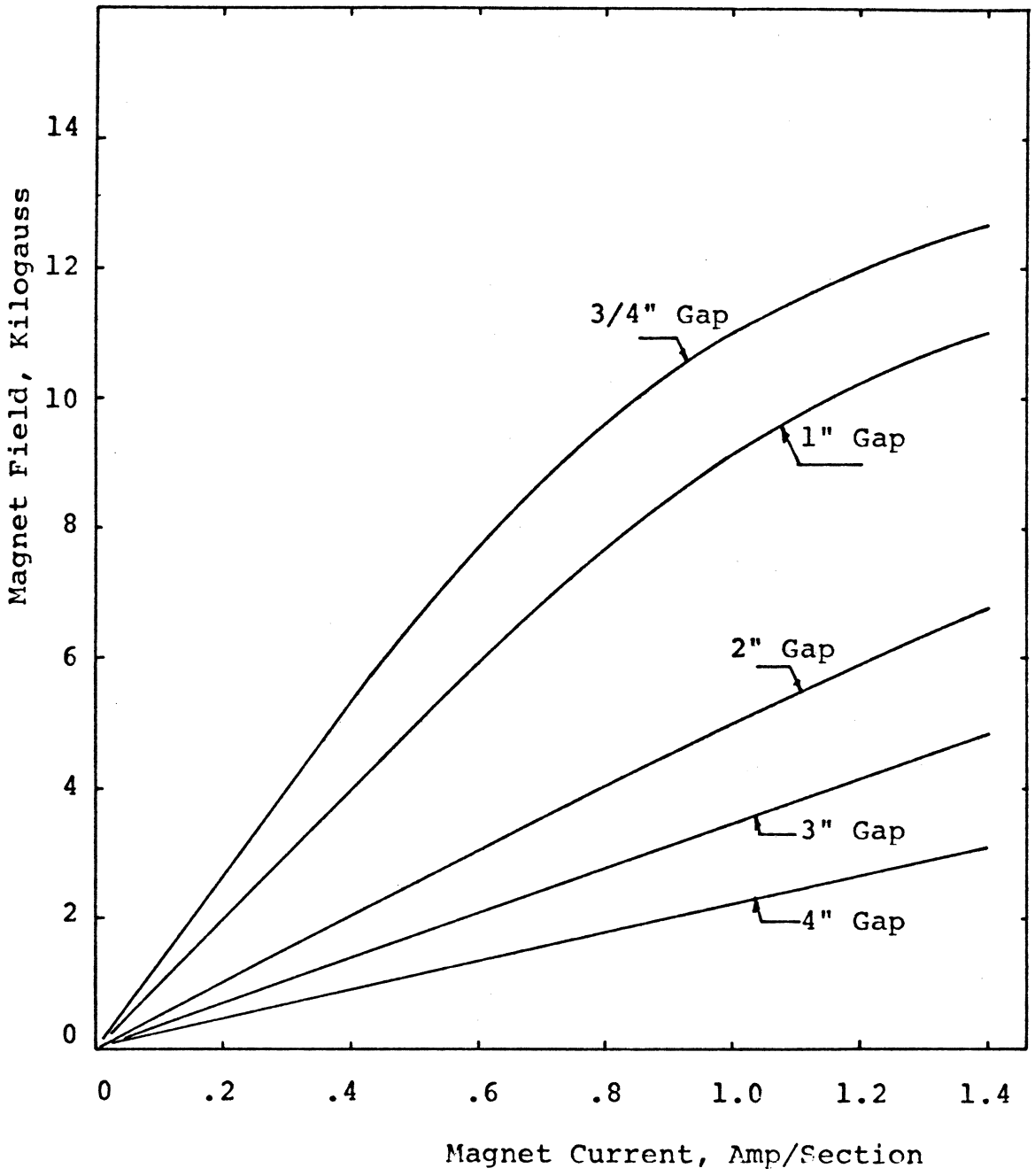

Figure E-4 Approximate Gap Field as a Function of Magnet Current and Gap Width.

5082

APPENDIX F

COMPUTER PROGRAM LISTINGS

```
C  TRANSFERS MCA COUNTS TO DIAMETER INTERVAL COUNTS

C  AMPL=APLIFICATION BETWEEN PM TUBE AND MCA
C  COR=ZERO LEVEL CORRECTION, IF REQUIRED, # CHANNELS
C  DIV= DIVIDER FOR MCA COUNTS
C  LZ=ZERO LEVEL, CHANNEL # AT WHICH PULSE HEIGHT IS ZERO
C  BCHNL= BOUNDARY CHANNEL AT DIAMETER INCREMENTS
C  V.LEVEL= VOLTAGE LEVEL AT BOUNDARY CHANNELS, VOLTS
      DIMENSION DIA(40),VOLTAG(40),VLEVL(128),BCHNL(40)
      DIMENSION DIAMCA(39),TITLE(40),MCA(128),AX(39)
 28   READ(5,27,END=31)TITLE
 27   FORMAT(40A2)
      READ(5,1,END=31)AMPL,COR,DIV,LZ
 1    FORMAT(3(F10.2),2X,I3)
      IF(DIV.EQ.0.)DIV=1.
      IF(LZ.EQ.0)LZ=6
 2    NC=128
      DELV=2./122.
      DLEV=-DELV*6.
      ZLLL=2.
 32   DO 22 I=1,NC
 22   MCA(I)=0.
      WRITE(12,20)
 20   FORMAT(1H1,' LSCAN')
      WRITE(6,27)TITLE
      WRITE(12,3)LZ,AMPL,NC
 3    FORMAT(' ZERO LEVEL:',I3/' AMPLIFICATION:',F6.2/'
     1' CHANNELS:',I3)
      WRITE(6,35)DIV,COR
 35   FORMAT(' DEVIDER:',F6.2/' Z.L. CORRECTOR:',F6.2)
      DIA(1)=1
      DIA(2)=2
      DO 4 I=5,25
 4    DIA(I-2)=.5*I+.5
      READ(5,26)VOLTAG
 26   FORMAT(8E10.4)
      READ(7,19,END=24)(MCA(I),I=1,NC)
 19   FORMAT(16I5)
 24   WRITE(12,23)(MCA(I),I=1,NC)
 23   FORMAT(/' MCA:'/(10I7))
      DO 5 I=14,30
 5    DIA(I+10)=I
      DO 6 I=1,40
 6    VOLTAG(I)=AMPL*VOLTAG(I)
      DLZ=LZ-COR
      LZ=LZ-COR+.999
      VLEVL(LZ)=(LZ-DLZ)*DELV
      LZ1=LZ+1
      NC1=NC-1
      DO 7 I=LZ1,NC
 7    VLEVL(I)=VLEVL(I-1)+DELV
      DO 8 I=1,40
      BCHNL(I)=-1
      IF(VOLTAG(I).LE.0.)GO TO 8
      DO 9 J=LZ,NC1
```

```
      IF(VOLTAG(I).GT.VLEVL(J+1))GO TO 9
      IF(VOLTAG(I).LT.VLEVL(J))GO TO 8
      BCHNL(I)=J+(VOLTAG(I)-VLEVL(J))/DELV
      GO TO 8
9     CONTINUE
8     CONTINUE
      DO 10 I=1,39
      AX(I)=0
      IB=BCHNL(I)
      IF(IB.LE.1)GO TO 10
      X=B CHNL(I)-IB
      A=(MCA(IB-1)+MCA(IB))*.5
      IF(X-.5)11,12,12
11    C=MCA(IB-1)-(MCA(IB-1)-MCA(IB))*X
      AX(I)=(A+C)*X*.5
      GO TO 10
12    C=MCA(IB)-(MCA(IB)-MCA(IB+1))*(X-.5)
      AX(I)=(MCA(IB)+C)*.5*(X-.5)
      AX(I)=AX(I)+(A+MCA(IB))*.5*.5
10    CONTINUE
      DO 13 I=1,39
      SUM=0.
      IB=BCHNL(I)
      IB1M1=BCHNL(I+1)-1
      DIAMCA(I)=-1
      IF(I.LE.2)GO TO 13
      IF(IB.LE.1)GO TO 13
      IF(IB1M1.LE.0)GO TO 13
      IF(I.GE.39)GO TO 13
      IF(IB.GT.IB1M1)GO TO 25
      DO 14 J=IB,IB1M1
14    SUM=SUM+MCA(J)
25    DIAMCA(I)=SUM-AX(I)+AX(I+1)
13    CONTINUE
      ZLL=ZLLL-(LZ-1)*DELV+DLEV
      DO 17 I=1,39
      IF(VOLTAG(I).LT.ZLL)GO TO 17
      M=I
      GO TO 34
17    CONTINUE
34    IF(DIV.EQ.1.)GO TO 18
      DO 33 I=1,M
      IF(DIAMCA(I).EQ.-1)GO TO 33
      DIAMCA(I)=DIAMCA(I)/DIV
33    CONTINUE
18    WRITE(12,21)
21    FORMAT(/4X,' DIAMETER      COUNTS      V. LEVEL'
     1'     BCHNL')
      DO 15 I=1,M
15    WRITE(12,16)DIA(I),DIAMCA(I),VOLTAG(I),BCHNL(I)
16    FORMAT(6F12.4)
      IB=BCHNL(M-1)
      X=B CHNL(M-1)-IB
      AR=MCA(IB)*(1-X)
      SUM=AR
```

```
      IB=IB+1
      DO 30 I=IB,NC
30    SUM=SUM+MCA(I)
      SUM=SUM/DIV
      WRITE(12,29)DIA(M),SUM
29    FORMAT(' ABOVE ',F4.1,' MICRON DIA.:',F7.2,' COUNTS
     1///)
      GO TO 28
31    STOP
      END
```

```
C  PROGRAM TO SOLVE DYNAMICS AND DIFFUSION EQUATIONS

C  PINT=PRINTING INTERVAL,SEC.
C  OPT=OPTIONS, IF EQ. 1.D0 NO DIFFUSION
C  OPT=3.D0 LETS IT OSCILLATE
C  R,CM; P, BAR/CM-CM; UM=CP, S=DYNES/CM, T=SECS, W=CYC/SEC
C  T=DEG-K,D=SQ-CM/SEC, RB=BAR-CM/MOL-DEG-K, RMAX=CM
C  RHO=GR/CC, C=GMOL/CC
C  CONC=FRACTION OF SATURATION FOR GAS
C  NR=# OF DIVISIONS ON R
C  R=MAX RADIUS OF EFFECT OF DIFFUSION INVESTIGATED
C  GG=RATIO OF VOLUME OF BUBBLE WHEN UNDER EQUI. TO THE VOL
C  WHEN R(T)=RO
      IMPLICIT REAL*8 (A-Z)
      INTEGER NDIM,IHLF,J,N,I,NR,N1,NT
      COMMON C,C1,C2,S,UM,PA,W,RHO,RO,DR,CIN,PGO,PGT,D,ROY1
      COMMON TT,DT,BETA,GAMMA,ALAM,PP,P,ERC,GG,OPT,PINT,PV
      COMMON VOL,FPD,RB,PL,J,N,NR
      EXTERNAL FCT,OUTP
      DIMENSION Y(2),DERY(2),AUX(8,2),PRMT(5),C(100,300)
      NAMELIST /DATA/ PRMT,Y,DERY,S,PL,PV,RO,UM,RHO,PA,NDIM,
     XF,PI,C1,TT,ERC,D,MOLW,CONC,RMAX,NR,RB,MULT,GG,OPT,PINT
      C1=0.D0
 4    DERY(1)=.5D0
      DERY(2)=.5D0
      PRMT(5)=0.D0
      Y(2)=0.D0
      IF(C1.NE.0.D0)GO TO 9
      READ(5,DATA,END=1)
      W=2.D0*PI*F
      CIN=CONC/MOLW*1.D-2*1.8
      DR=RMAX/NR
      VOL=4.D0/3.D0*PI*RO**3
      FPD=4.D0*PI*D
      DO 8 I=1,NR
 8     C(I,1)=CIN
      DO 7 I=1,NR
 7     C(I,2)=C(I,1)
      PGO=(PL-PV+2.D-6*S/RO)
      PGO=CONC*GG
      PAA=PL-PV-PGO+2.D-6*S/RO
 11   IF(PA.LE.PAA)PA=PA+.5
      IF(PA.LE.PAA)GO TO  11
      PRMT(1)=DARSIN(PAA/PA)/W
 9    J=PRMT(1)/PINT-1
      IF(J.LT.0)J=0
      C1=0.D0
      N=0
      IF(OPT.EQ.1.D0)GO TO 6
      NT=PRMT(2)/PRMT(3)
      IF(NT.GT.300)NT=300
      DT=PRMT(3)
      GAMMA=DT/DR
      ALAM=GAMMA/DR
```

```
      BETA=2.D0*D*ALAM
      PP=1.D0+BETA
      P=(1.D0-BETA)/PP
6     WRITE(6,5)
5     FORMAT(1H1//)
      WRITE(6,DATA)
      PGT=PGO*MULT
      WRITE(6,3)PA,PAA
      WRITE(6,10)RO,PA,CONC,TT
10    FORMAT(// RO=',1PD12.4// PA=',1PD12.4// CONC=',1PD12.4
     1 // TT',1PD12.4/)
3     FORMAT(' PA,PAA',2(1PE12.4),' BAR/SQ-CM')
      WRITE(6,2)
2     FORMAT(' T,Y,DERY,PRMT(4),PGT,PGTR,M,N,IHLF')
      Y(1)=RO
      CALL DRKGS(PRMT,Y,DERY,NDIM,IHLF,FCT,OUTP,AUX)
      GO TO 4
1     STOP
      END
      SUBROUTINE FCT(T,Y,DERY)
      IMPLICIT REAL*8 (A-Z)
      COMMON C,C1,C2,S,UM,PA,W,RHO,RO,DR,CIN,PGO,PGT,D,ROY1
      COMMON TT,DT,BETA,GAMMA,ALAM,PP,P,ERC,GG,OPT,PINT,PV
      COMMON VOL,FPD,RB,PL,J,N,NR
      DIMENSION Y(2),DERY(2),AUX(8,2),PRMT(5),C(100,300)
      DERY(1)=Y(2)
      DERY(2)=-1.5D0*Y(2)/Y(1)*Y(2)+(PGT*(RO/Y(1))**3-PL-
     1 2.D-6*S/Y(1)+PV-4.03D-8*UM*Y(2)/Y(1)+PA*DSIN(W*T))/
     2 (RHO*Y(1))*9.81D+5
      RETURN
      END
      SUBROUTINE OUTP(T,Y,DERY,IHLF,NDIM,PRMT)
      IMPLICIT REAL*8 (A-Z)
      INTEGER NDIM,IHLF,J,N,I,NR,N1,NT,NN,M,NRR,I1,I2,N2
      COMMON C,C1,C2,S,UM,PA,W,RHO,RO,DR,CIN,PGO,PGT,D,ROY1
      COMMON TT,DT,BETA,GAMMA,ALAM,PP,P,ERC,GG,OPT,PINT,PV
      COMMON VOL,FPD,RB,PL,J,N,NR
      DIMENSION Y(2),DERY(2),AUX(8,2),PRMT(5),C(100,300)
      M=0
      PGTR=0.D0
      IF(OPT.EQ.1.D0)GO TO 17
      IF(IHLF.GT.0)GO TO 12
      N=N+1
      N1=N+1
      N2=N+2
      C(NR,N)=CIN
      M=Y(1)/DR+.5D0
      NRR=M+9
      IF(M.EQ.0.D0)GO TO 5
      ROY1=(RO/Y(1))**3
      C(M,N2)=CIN/PGO*PGT*ROY1*GG*GG
      DO 9 I=M,NR
      I1=I+1
      I2=I+2
      V=Y(2)*(Y(1)**2/(I*DR)**2)
```

```
      VBIG=V*GAMMA-BETA/I
      Q=(VBIG-BETA)/PP
      R=(VBIG+BETA)/PP
      IF(C(I1,N).LT.1.D-6)C(I1,N)=CIN
      IF(C(I2,N1).LT.1.D-6)C(I2,N)=CIN
      IF(C(I ,N1).LT.1.D-6)C(I,N1)=CIN
      C(I1,N2)=P*C(I1,N)-Q*C(I2,N1)+R*C(I,N1)
      IF(DABS(C(I1,N2)-CIN)/CIN.LT.ERC)GO TO 19
9     CONTINUE
19    I=I+1
      DO 7 NN=I,NR
7     C(NN+1,N2)=CIN
      DN=FPI*(C(M+1,N)-C(M,N))*GAMMA*Y(1)**2
      DPG=RB*TT*DN/VOL
      PGT=PGT+DPG
      PGTR=PGT*ROY1
      IF(Y(2).GT.0.D0)GO TO 4
      GO TO 3
4     IF(N.EQ.298)GO TO 15
      GO TO 17
15    N=0
      DO 16 I=M,NR
      C(I,1)=C(I,299)
16    C(I,2)=C(I,300)
17    IF(OPT.EQ.3.D0)GO TO 14
      IF(Y(2).GE.0.D0)GO TO 14
      PRMT(5)=1.D0
      GO TO 3
14    IF(T.LT.J*PINT)GO TO 2
3     WRITE(6,1)T,Y(1),Y(2),DERY,PRMT(4),PGT,PGTR,
     1M,N,IHLF
1     FORMAT(' *',8(1PD12.4),5I4)
      J=J+1
      IF(OPT.EQ.1.D0)GO TO 2
      WRITE(6,10)(C(I,N2),I=M,NRR)
10    FORMAT(10(1PD12.4))
      GO TO 2
12    WRITE(6,13)IHLF,PRMT(3)
13    FORMAT(' IHLF=',I2,' DT=',1PD12.4)
      PRMT(3)=PRMT(3)/(2**(IHLF+2))
      C1=1.D0
      PRMT(5)=1.D0
2     RETURN
5     WRITE(6,6)
6     FORMAT(' M IS ZERO')
11    FORMAT(I4,6(1PD12.4))
      END
```

APPENDIX G

EXPERIMENTAL APPARATUS

1. Frequency counter, Model DY-2500, Dymec Inc.
2. Scaler, Model 430, Ortec Inc.
3. Timer, Model SC-42, Tracelab Inc.
4. Pulse generator, Type 114, Tektronix Inc.
5. Delayed pulse generator, Model 222A , Hewlett Packard Inc.
6. Storage oscilloscope, type 564, Tektronix Inc.
7. Dual beam oscilloscope, type 551, Tektronix Inc.
8. Multichannel analyser, ND-110, Nuclear Data Inc.
9. Display Monitor, ND-410, Nuclear Data Inc.
10. IBM typewriter, IBM Co.
11. X-Y recorder, Model 2D, Hewlett Packard Inc.
12. Autofinger ND-316, Nuclear Data Inc.
13. He-Ne Laser, Model 120, Spectra Physics Inc.
14. High voltage power supply, Model N-4035, Hamner Electronics Inc.
15. He-Ne Laser, Model 132, Spectra Physics Inc.
16. Variable auto transformer, Type 2PF751, Staco Inc.
17. Chemical pump, Model 3-MD, Little Giant Pump Co.
18. Vacuum pump, Model 560YZ-1838, Central Scientific Co.
19. Variac, 20 ampere, General Radio Co.

20. Temperature recorder/controller, Model Y153x62P-(W72)-(13D), Honeywell Co.

21. Electro Magnet, Model V-4007-1, Varian Associates.

22. Regulated magnet power supply, Model V2200, Varian Associates.

23. Power amplifier, Model 2250 MB, MB Electronics Inc.

24. Audio oscillator, Model 201C, Hewlett Packard Inc.

25. Vacuum tube voltmeter, Model 400H, Hewlett Packard Inc.

26. Dual beam oscilloscope, Type 502, Tektronix Inc.

27. Dual trigger, Model TR104S/N EG and G Inc.

28. DC power supplies, Model 902, Analog Devices Inc.

29. Audio oscillator,' Model 200 AB, Hewlett Packard Inc.

30. Photomultiplier tube, Type 9558B, Emitronics Inc.

31. Tester, Model 630, Triplett Co.

32. DC Power Supply, Harrison 6209B, Hewlett Packard Inc.

33. Manometer, King Engineering Co.

34. Operational amplifiers, 741 HC, Fairchild Semiconductor Inc.

35. Lenses

36. Telescope

37. Pulse divider - square wave generator

38. Peak detector

39. Zero level shifter

40. Pu-Be sources

41. Ultrasonic horn

42. Impedance matching power transformer

43. Heater, MT02, Edwin L. Wiegand Co.

44. Ampere meter, Model MD, Simpson

45. Rotating flow meter, Model AN-10, Cox Instrument Division

46. Coulter tube, 70 μm orifice, Coulter Electronics Inc.

APPENDIX H

IMPEDANCE MATCHING

Impedance matching between amplifier and transformer and transformer and exponential horn assembly, is very important for the purposes of adequate power transfer. Approximate voltage and current measurements showed that input-B of transformer was about 3Ω, and input-A was about 16Ω. Input impedance of the horn, by the same method, was found to be about 825Ω. However, output impedance of the transformer would not match 825Ω horn impedance, since Output-A of transformer was 500Ω and Output-B only 21.5Ω. Thus, the best impedance match was obtained using input-B and output-A of the transformer. During impedance measurements, voltage was measured by a Simpson AC voltmeter and current was calculated by measuring voltage drop across a known resistor. Use of HP400D or equivalent RMS voltmeter is recommended for the voltage measurements for more accurate results. Efficiency of the system was calculated using power input to the acoustic horn assembly and power output of the amplifier and found to be about twenty per cent.

BIBLIOGRAPHY

1. Leonard Euler, "Theorie plus complete des machines, qui sont mises en mouvement par La reaction de L'eau," Historie de L'Academie Royale des Sciences et Belles Lettres, Classe de Philosophie Experimentale, pp. 227-295, Mem 10, 1754, Berlin, 1756.

2. Sir John Thornycroft and S. W. Barnaby, "Torpedo-boat Destroyers," Proc. Inst. Civ. Eng., 122 (1895), 51-103.

3. S. W. Barnaby, "On the Formulation of Cavities in Water by Screw Propellers at High Speeds," Trans. Inst. Nav. Arch., 39 (1898), 319-144.

4. Sir Charles Parsons, "The Application of the Compound Steam Turbine to the Purpose of Marine Propulsion," Trans. Inst. Nav. Arch., 38 (1897), 232-242.

5. L. C. Burrill, "Sir Charles Parsons and Cavitation," Trans. Inst. Marine Engrs., 43, #8 (1951), 149-167.

6. Sir Charles A. Parsons and S. S. Cook, "Investigations into the Causes of Corrosion or Erosion of Propellers," Trans. Inst. Nav. Arch., 61 (1919), 222-247.

7. O. Reynolds, "On the Internal Cohesion of Liquids and the Suspension of a Column of Mercury to a Height more than Double that of Barometer," Scientific Papers, I, Cambridge University Press (1900), 231-243.

8. J. C. Fisher, "The Fracture of Liquids," J. Appl. Phys., 19 (1948), 1062-1067.

9. R. D. Ivany, "Collapse of a Cavitation Bubble in Viscous, Compressible Liquid Numerical and Experimental Analysis," Ph. D. Thesis, Nuclear Engineering Department, University of Michigan, 1965.

10. R. T. Knapp, J. W. Daily and F. G. Hammitt, Cavitation, McGraw-Hill (1970).

11. M. S. Plesset, "Tensile Strength of Liquids," C. I. T. Report #85-47, Pasadena, California, 1969.

12. L. J. Briggs, "Maximum Superheating of Water as a Measure of Negative Pressure," J. Appl. Phys., 26, 8, 1955.

13. O. Ahmed, "A New Technique for the Measurement of Cavitation Nuclei Spectra," Ph. D. Thesis, The University of Michigan, 1973.

14. J. Pyun, "On the Use of Coulter Counter to Measure the Microbubble Spectrum in Water," Ph. D. Thesis, The University of Michigan, 1973.

15. R. G. Perel'man and E. V. Govorskii, "Effect of a Constant Magnetic Field on Cavitation Erosion in an Electrically Conducting Liquid," Soviet Physics-Doklady, 16, 2 (1971).

16. I. Landa , E. S. Tebay, Johnson ,V., and J. Lawrence, "The Measurement of Bubble Size Distribution using Scattered Light," Hydronautics Incorporated Technical Report 707-4, 1970.

17. A. Keller, "The Influence of the Cavitation Nucleus Spectrum on Cavitation Inception, Investigated with a Scattered Light Counting Method," J. of Basic Engr., December 1972.

18. A. Keller, E. Yilmaz and F. G. Hammitt, "Comparative Investigations of the Scattered Light Counting Method for the Registration of Cavitation Nuclei and the Coulter Counter," Report # UMICH 01357-36-T, The University of Michigan, Ann Arbor, Michigan, 1973.

19. S. Kinsman and J. R. Coulter, Jr., "Particle Size Measurements using the Resistance Change Principle," American Ceramic Society, 63rd Annual Meeting, Toronto, Canada, 1961.

20. Coulter Counter Model-A Manual, Coulter Electronics, Hialeah, Florida.

21. W. R. Turner, "Physics of Microbubbles," Vitro Laboratories, Technical Note 01654-2, Silver Spring, Maryland 1963.

22. F. R. Schiebe and J. M. Killen, "An Evaluation of Acoustic Techniques for Measuring Gas Bubble Size Distributions in Cavitation Research," University of Minnesota, Project Report #120, 1971.

23. L. R. Gavrilov, "On the Size Distribution of Gas Bubbles in Water," Soviet Physics-Acoustics, 15, 1, 1964.

24. W. J. Galloway, "An Experimental Study of Acoustically Induced Cavitation in Liquids," J. of Acous. Soc. of Am., 26, 5, 1954.

25. M. Strasberg, "Onset of Ultrasonic Cavitation in Tap Water," J. of Acous. Soc. of Am., 31, 2, 1959.

26. G. W. Willard, "Ultrasonically Induced Cavitation in Water: A Step-by-Step Process," J. of Acous. Soc. of Am., 4,1953.

27. R. E. Nystrom, "Ultrasonically Induced Sodium Superheat," Ph.D. Thesis, The University of Michigan, 1969.

28. C. D. Messino, D. Sette and E. Wanderlingh, "Effects of Solid Impurities on Cavitation Nuclei in Water," J. of Acous. Soc. of Am., 41, 3, 1967.

29. E. N. Harvey, W. D. McElroy, and A. H. Whiteley, "On Cavity Formation in Water," J. Appl. Phys., 18, 1947.

30. F. E. Fox and K. F. Herzfeld, "Gas Bubbles with Organic Skin as Cavitation Nuclei," J. of Acous. Soc. of Am., 26, 6, 1954.

31. N. Harvey, et al., "Bubble Formation in Animals," Cellular and Comparative Physiology, 24, 1944.

32. M. Strasberg, "Undissolved Air Cavities as Cavitation Nuclei," Cavitation in Hydrodynamics, HMSO, 1956.

33. J. W. Holl, "Nuclei and Cavitation," Trans. ASME, J. of Basic Engr., December 1970.

34. R. E. Apfel, "The Role of Impurities in Cavitation-Threshold Determination," J. of Acous. Soc. of Am., 48, 5,1970.

35. R. T. Knapp, "Cavitation and Nuclei," Trans. ASME, 80, August 1958.

36. M. S. Plesset and S. A. Zwick, "Non-Steady Heat Diffusion Problem with Spherical Symmetry," J. Appl. Phys., 23, 1, 1952.

37. H. K. Forster and N. Zuber, "Growth of a Vapor Bubble in a Superheated Liquid," J. Appl. Phys., 25, 4, 1954.

38. Lord Rayleigh, Phil. Mag., 34, 1917.

39. H. K. Forster, "On the Conduction of Heat into a Growing Vapor Bubble," J. Appl. Phys., 25, 1954.

40. H. K. Forster and N. Zuber, "Dynamics of Vapor Bubbles and Boiling Heat Transfer," A. I. Ch. E. Journal, 1, 4, 1955.

41. M. S. Plesset and N. Zwick, "The Growth of Vapor Bubbles in Superheated Liquids," J. Appl. Phys., 25, 4, 1954.

42. H. K. Forster, "Diffusion in a Moving Medium with Time Dependent Boundaries," A. I. Ch. E. Journal, 3, 1957.

43. G. Birkhoff, R. S. Margulies and W. A. Horning, "Spherical Bubble Growth," Phys. of Fluids, 1, 3, 1958.

44. L. E. Scriven, "On the Dynamics of Phase Growth," Ch. Engr. Sci., Genie Chimique, 10, 1/2, 1959.

45. L. A. Skinner and S. G. Bankoff, "Dynamics of Vapor Bubbles in Spherically Symmetric Temperature Fields of General Variation," Phys. of Fluids, 7, 1, 1964.

46. M. S. Plesset, and Din-Yu Hsieh, "Theory of Gas Bubble Dynamics in Oscillating Pressure Fields," Phys. of Fluids, 3, 6, 1960.

47. W. J. Bernhorst and G. N. Hatsopoulos, "Bubble Growth Calculation without Neglect of Interfacial Discontinuities," Trans. ASME, J. Appl. Mech., Paper #67-WA/APM-36.

48. F. G. Blake, Jr., "Cavitation Threshold Sound Pressures in Water as a Function of Temperature and Hydrostatic Pressure," Technical Memorandum #12, Harvard University, Massachusetts, 1949.

49. M. S. Plesset, "Effect of Dissolved Gases on Cavitation in Liquids," C.I.T. Report #85-55, 1970.

50. Din-Yu Hsieh and M. S. Plesset, "Theory of Rectified Diffusion of Mass into Gas Bubbles," J. Acous. Soc. of Am., 33, 2, 1961.

51. M. S. Plesset and Din-Yu Hsieh, "Comments on the Theory of Rectified Diffusion," Letters to Editor, J. Acous. Soc. of Am., 1961.

52. A. Eller, and H. G. Flynn, "Rectified Diffusion during Nonlinear Pulsations of Cavitation Bubbles," J. Acous. Soc. of Am., 37, 3, 1965.

53. Din-Yu Hsieh, "Rectified Internal Convection and Ultrasonic Cavitation in Helium II," C. I. T. Report #85-33, 1966.

54. L. V. Wijngaarden, "On the Growth of Small Cavitation Bubbles by Convective Diffusion," J. Heat and Mass Transfer, 10, 1967.

55. Yu. Ya. Boguslavskii, "Diffusion of a Gas into a Cavitation Void," Soviet-Physics-Acous., 13, 1, 1967.

56. Yu. L. Levkovskii, "Effect of Diffusion on the Sound Radiation from a Cavitation Void," Soviet Physics-Acous., 14, 4, 1969.

57. L. A. Skinner, "Acoustically Induced Gas Bubble Growth," J. Acous. Soc. of Am., 51, 1, 1972.

58. O. A. Kapustina and Yu. G. Statnikov, "Influence of Acoustic Microstreaming on the Mass Transfer in a Gas Bubble-Liquid System," Soviet Physics-Acous., 13, 3, 1968.

59. Yu. G. Statnikov, "Microstreaming about a Gas Bubble in a Liquid," Soviet Physics-Acous., 13, 3, 1968 .

60. E. A. Neppiras and B. E. Noltingk, "Cavitation Produced by Ultrasonics," Proc. Physical Soc. London, B64, 1951.

61. B. E. Noltingk, and E. A. Neppiras, "Cavitation Produced by Ultrasonics," Proc. Phys. Soc. London, 633, 1950.

62. M. S. Plesset, "Bubble Dynamics," C. I. T. Report #85-23, 1963.

63. N. K. Adam, The Physics and Chemistry of Surfaces, Oxford University Press, 1946.

64. D. A. Glasser, Physics Rev., 87, 665, 1952.

65. W. B. Fretter, Ann. Rev. Nuclear Sci., 5, 145, 1955.

66. H. T. Whitehouse, Jr., " A Study of Alpha- Lithium-7-, and Fission-fragment-induced Bubble Nucleation in Superheated Liquids, " Tech. Report #SU-326-P13-8, Stanford University, 1972.

67. D. A. Pilati, "Bubble Nucleation by Fast Neutron Recoil Atoms in Superheated Ethyl-alcohol and Water, " Tech. Rep. # SU-326-P13-7, 1972.

68. F. Seitz, "On the Theory of the Bubble Chamber, " Phys. of Fluids, 1, 1, 1958.

69. J. W. Holl, "An Effect of Air Content on the Occurrence of Cavitation, " Trans. ASME, Journal Basic Engr., 60-Hyd-8, 1960.

70. H. P. Flatt, "Transient Bubble Growth in a Homogeneous Reactor, " Atomics International Report # NAA-SR-3923, Canoga Park, California, 1960.

71. A. Eller and H. G. Flynn, "The Equilibrium and Stability of a Translating Cavity in a Liquid, " J. Fluid Mech., 30, 4, (G. B.), 1967.

72. C. R. Bell, "Radiation Induced Nucleation of the Vapor Phase, " Ph. D. Thesis, M. I. T., 1970.

73. L. W. Deitrich, "A Study of Fission-Fragment-Induced Nucleation in Superheated Water, " Ph. D. Thesis, Stanford University, Report # SU-326-P-13-4, 1969.

74. Lord Rayleigh, Philosophical Mag. S. 5, 34, 207, 1892.

75. D. Sette and F. Wanderlingh, "Nucleation by Cosmic Rays in Ultrasonic Cavitation, " Phys. Rev., 125, 2, 1962,

76. D. Sette and F. Wanderlingh, "Thermodynamic Theory of Bubble Nucleation Induced in Liquids by High-energy Particles, " J. Acous. Soc. Am., 41, 4, 1967.

77. D. Lieberman, "Radiation Induced Cavitation, " Phys. Fluids, 2, 4, 1959.

78. R. D. Finch, "Influence of Radiation on the Cavitation Threshold of Degassed Water, " J. Acous. Soc. Am., 36, 12, 1964.

79. M. Greenspan and C. E. Tschiegg, "Radiation-induced Acoustic Cavitation; Apparatus and Some Results," N.B.S., J. Research, 716, 4, 1967.

80. A. I. Eller, "Bubble Growth by Diffusion in an 11-KHz Sound Field, J. Acous. Soc. Am., 52, 5,

81. R. Garcia, "Comprehensive Cavitation Damage Data for Water and Various Liquid Metals Including Correlations with Material and Fluid Properties," Ph. D. Thesis, The University of Michigan, 1966.

82. A. Keller, Private communications.

83. A. Keller, "Experimentelle und theoretische undersuchungen zum problem der modellmässigen behandlung von strömungskavitation," Ph. D. Thesis, Technischen Universitat Munchen, 1973.

84. Model ND-110, 128 Channel Analyzer Instruction Manual, 1965.

85. M. S. Plesset, "Tensile Strength of Liquids," Cavitation State of Knowledge, 1969.

86. A. J. Acosta and B. R. Parkin, "Cavitation Inception," Presentation to the Seventh Meeting of the American Towing Tank Conference, C.I.T., 1974.

87. J. W. Holl and A. L. Treaster, "Cavitation Hysteresis," Trans. ASME, J. Basic Engr., March 1966.

88. W. C. Connolly, "The Threshold of Cavitation as a Function of Temperature and Frequency for Benzene and Ethyl Alcohol," Dissertation, Catholic University of America, 1954.

89. B. Hahn and R. N. Peacock, Nuclear Instrumentation and Methods, 20, 1963.

90. N.B.S. Handbook 72.

91. N.B.S. Handbook 69.

92. R. Brossman, "Die Lichtstreuung an Kleinen Teilchen als Grundlage einer Teilchengrossenbestinmunz," Dissertation, Tech. Hoch., Karlsruhe, 1966.

93. D. Messino, D. Sette and F. Wanderlingh, "Statistical Approach to Ultrasonic Cavitation," J. Acous. Soc. Am., 35, 10, 1963.

94. J. W. Hoyt, "The Effect of Additives on Fluid Friction," Trans. ASME, J. Basic Engr., 94, 2, 1972.

95. J.H.J. Van der Meulen, "Cavitation Suppression by Polymer Injection," A.S.M.E. Polyphase Flow Forum, 1972-74.

96. P. D. Fitzgerald, "Laser Doppler Velocimeter Evaluation and Measurements in a Flow with Drag Reduction," Ph.D. Thesis, The University of Michigan, 1974.

97. M. G. Sirotyuk, "Stabilization of Gas Bubbles in Water," Soviet Physics-Acoustics, 16, 2, 1970.

98. R. Hickling and M. S. Plesset, "The Collapse of a Spherical Cavity in a Compressible Liquid," C.I.T. Report #85-24, 1963.

99. T. Mitchell and F. G. Hammitt, "On the Effects of Heat Transfer upon Collapsing Bubbles," Nucl. Sci. Eng., 53, 1974.

100. I. A. Shalobasov and K. K. Shal'nev, "Effect of an External Magnetic Field on Cavitation and Erosion Damage," Heat Transfer-Soviet Research, 3, 6, 1971.

101. R. B. Stephenson, "Sonoluminescence from Acoustically Cavitated Water," Report # UMICH 01357-20-T, The University of Michigan, 1971.

102. K. K. Shalnev, et al., "Experimental Investigation of Effect of External Magnetic and Electric Fields on Cavitation and Erosion," Proc. Conference on Cavitation, Heriot-Watt Uni. Edinburg, Scotland, September 1974.